Non-Langevin Recombination in Fullerene and Non-Fullerene Acceptor Solar Cells

Dipl. Phys. Seyed Mehrdad Hosseini

Kumulative Dissertation

zur Erlangung des akademischen Grades
"doctor rerum naturalium"
(Dr. rer. nat.)
in der Wissenschaftsdisziplin Experimentalphysik

Eingereicht an der
Mathematisch-Naturwissenschaftlichen Fakultät
Institut für Physik und Astronomie
der Universität Potsdam

Ort und Tag der Disputation: Potsdam, 18.02.2022

Supervisor: Prof. Dr. Safa Shoaee
Second supervisor: Prof. Dr. Dieter Neher

Reviewers: Prof. Dr. Safa Shoaee
Prof. Dr. Dieter Neher
Prof. Dr. James Robert Durrant

Published online on the
Publication Server of the University of Potsdam:
https://doi.org/10.25932/publishup-54783
https://nbn-resolving.org/urn:nbn:de:kobv:517-opus4-547831

Abstract

Organic solar cells (OSCs), in recent years, have shown high efficiencies through the development of novel non-fullerene acceptors (NFAs). Fullerene derivatives have been the centerpiece of the accepting materials used throughout organic photovoltaic (OPV) research. However, since 2015 novel NFAs have been a game-changer and have overtaken fullerenes. However, the current understanding of the properties of NFAs for OPV is still relatively limited and critical mechanisms defining the performance of OPVs are still topics of debate.

In this thesis, attention is paid to understanding reduced-Langevin recombination with respect to the device physics properties of fullerene and non-fullerene systems. The work is comprised of four closely linked studies. The first is a detailed exploration of the fill factor (FF) expressed in terms of transport and recombination properties in a comparison of fullerene and non-fullerene acceptors. We investigated the key reason behind the reduced FF in the NFA (ITIC-based) devices which is faster non-geminate recombination relative to the fullerene (PCBM[70]-based) devices. This is then followed by a consideration of a newly synthesized NFA Y-series derivative which exhibits the highest power conversion efficiency for OSC at the time. Such that in the second study, we illustrated the role of disorder on the non-geminate recombination and charge extraction of thick NFA (Y6-based) devices. As a result, we enhanced the FF of thick PM6:Y6 by reducing the disorder which leads to suppressing the non-geminate recombination toward non-Langevin system. In the third work, we revealed the reason behind thickness independence of the short circuit current of PM6:Y6 devices, caused by the extraordinarily long diffusion length of Y6. The fourth study entails a broad comparison of a selection of fullerene and non-fullerene blends with respect to charge generation efficiency and recombination to unveil the importance of efficient charge generation for achieving reduced recombination.

I employed transient measurements such as Time Delayed Collection Field (TDCF), Resistance dependent Photovoltage (RPV), and steady-state techniques such as Bias Assisted Charge Extraction (BACE), Temperature-Dependent Space Charge Limited Current (T-SCLC), Capacitance-Voltage (CV), and Photo-Induce Absorption (PIA), to analyze the OSCs.

The outcomes in this thesis together draw a complex picture of multiple factors that affect reduced-Langevin recombination and thereby the FF and overall performance. This provides a suitable platform for identifying important parameters when designing new blend systems. As

a result, we succeeded to improve the overall performance through enhancing the FF of thick NFA device by adjustment of the amount of the solvent additive in the active blend solution. It also highlights potentially critical gaps in the current experimental understanding of fundamental charge interaction and recombination dynamics.

Zusammenfassung

Organische Solarzellen (OSZ) haben in den letzten Jahren durch die Entwicklung neuartiger Nicht-Fulleren-Akzeptoren (NFA) hohe Wirkungsgrade erzielt. Fulleren-Derivate waren das Herzstück der Akzeptor-Materialien, die in der Forschung zur organischen Photovoltaik (OPV) verwendet wurden. Doch seit 2015 haben neuartige NFAs den Fullerenen den Rang abgelaufen. Allerdings ist das derzeitige Verständnis der Eigenschaften von NFA für OPV noch relativ begrenzt und kritische Mechanismen, die die Leistung von OPV bestimmen, sind immer noch Gegenstand von Diskussionen.

In dieser Arbeit geht es um das Verständnis der Reduced-Langevin-Rekombination in Hinblick auf die bauteilphysikalischen Eigenschaften von Fulleren- und Nicht-Fulleren-Systemen. Die Arbeit besteht aus vier eng miteinander verbundenen Studien. Die erste ist eine detaillierte Untersuchung des Füllfaktors (FF), ausgedrückt als Transport- und Rekombinationseigenschaften in einem Vergleich von Fulleren und Nicht-Fulleren-Akzeptoren.

Wir untersuchten den Hauptgrund für die geringere FF im NFA-Bauelement (auf ITIC-Basis), nämlich die schnellere nicht-geminate Rekombination im Vergleich zum Fulleren-Bauelement (auf PCBM[70]-Basis). Anschließend wird ein neu synthetisiertes NFA-Derivat der Y-Serie betrachtet, das derzeit die höchste Leistungsumwandlungseffizienz für OSZ aufweist. In der zweiten Studie veranschaulichten wir die Rolle der Unordnung bei der nicht-geminaten Rekombination und der Ladungsextraktion von dicken NFA-Bauelementen (auf Y6-Basis). Infolgedessen haben wir die FF von dickem PM6:Y6 verbessert, indem wir die Unordnung reduziert haben, was zur Unterdrückung der nicht-geminaten Rekombination in Richtung Nicht-Langevin-System führt. In der dritten Arbeit haben wir den Grund für die Dickenunabhängigkeit des Kurzschlussstroms von NFA-Bauelementen aufgedeckt, die durch die außerordentlich lange Diffusionslänge von Y6 verursacht wird. Die vierte Studie umfasst einen umfassenden Vergleich einer Auswahl von Fulleren- und Nicht-Fulleren-Mischungen in Hinblick auf die Effizienz der Ladungserzeugung und Rekombination, um die Bedeutung einer effizienten Ladungserzeugung zum Erzielen einer geringeren Rekombination aufzuzeigen.

Zur Analyse der OSCs habe ich transiente Messungen wie das Time Delayed Collection Field (TDCF), Resistance dependent Photovoltage (RPV) sowie stationäre Techniken wie die Bias

Assisted Charge Extraction (BACE), Temperature-Dependent Space Charge Limited Current (T-SCLC), Capacitance-Voltage (CV) und Photo-Induce Absorption (PIA) eingesetzt.

Die Ergebnisse dieser Arbeit zeichnen ein komplexes Bild zahlreicher Faktoren, die die Rekombination nach dem Prinzip des reduzierten Langèvins und damit die FF und die Gesamtleistung beeinflussen. Dies bietet eine geeignete Plattform zum Identifizieren wichtiger Parameter bei der Entwicklung neuer Mischsysteme. So ist es uns gelungen, die Gesamtleistung zu verbessern, indem wir die FF der dicken NFA-Vorrichtung durch Anpassung der Menge des Lösungsmittelzusatzes in der aktiven Mischungslösung erhöht haben. Außerdem werden potenziell kritische Lücken im derzeitigen experimentellen Verständnis der grundlegenden Ladungswechselwirkung und Rekombinationsdynamik aufgezeigt.

List of Publication

(1) Hosseini, S. M.; Roland, S.; Kurpiers, J.; Chen, Z.; Zhang, K.; Huang, F.; Armin, A.; Neher, D.; Shoaee, S. Impact of Bimolecular Recombination on the Fill Factor of Fullerene and Nonfullerene-Based Solar Cells: A Comparative Study of Charge Generation and Extraction. *J. Phys. Chem. C* **2019**, *123* (11), 6823–6830. https://doi.org/10.1021/acs.jpcc.8b11669.

(2) Zhang, S.; Hosseini, S. M.; Gunder, R.; Petsiuk, A.; Caprioglio, P.; Wolff, C. M.; Shoaee, S.; Meredith, P.; Schorr, S.; Unold, T.; Burn, P. L.; Neher, D.; Stolterfoht, M. The Role of Bulk and Interface Recombination in High-Efficiency Low-Dimensional Perovskite Solar Cells. *Adv. Mater.* **2019**, *31* (30). https://doi.org/10.1002/adma.201901090.

(3) Phuong, L. Q.; Hosseini, S. M.; Koh, C. W.; Woo, H. Y.; Shoaee, S. Measuring Competing Recombination Losses in a Significantly Reduced Langevin System by Steady-State Photoinduced Absorption and Photocurrent Spectroscopy. *J. Phys. Chem. C* **2019**, *123* (45), 27417–27422. https://doi.org/10.1021/acs.jpcc.9b08901.

(4) Shoaee, S.; Armin, A.; Stolterfoht, M.; Hosseini, S. M.; Kurpiers, J.; Neher, D. Decoding Charge Recombination through Charge Generation in Organic Solar Cells. *Sol. RRL* **2019**, *3* (11), 1900184. https://doi.org/10.1002/solr.201900184.

(5) Tokmoldin, N.; Hosseini, S. M.; Raoufi, M.; Phuong, L. Q.; Sandberg, O. J.; Guan, H.; Zou, Y.; Neher, D.; Shoaee, S. Extraordinarily Long Diffusion Length in PM6:Y6 Organic Solar Cells. *J. Mater. Chem. A* **2020**, *8* (16), 7854–7860. https://doi.org/10.1039/d0ta03016c.

(6) Perdigón-Toro, L.; Zhang, H.; Markina, A.; Yuan, J.; Hosseini, S. M.; Wolff, C. M.; Zuo, G.; Stolterfoht, M.; Zou, Y.; Gao, F.; Andrienko, D.; Shoaee, S.; Neher, D. Barrierless Free Charge Generation in the High-Performance PM6:Y6 Bulk Heterojunction Non-Fullerene Solar Cell. *Adv. Mater.* **2020**, *32* (9), 1906763. https://doi.org/10.1002/adma.201906763.

(7) Hosseini, S. M.; Tokmoldin, N.; Lee, Y. W.; Zou, Y.; Woo, H. Y.; Neher, D.; Shoaee, S. Putting Order into PM6:Y6 Solar Cells to Reduce the Langevin Recombination in 400 Nm Thick Junction. *Sol. RRL* **2020**. https://doi.org/10.1002/solr.202000498.

(8) Phuong, L. Q.; Hosseini, S. M.; Sandberg, O. J.; Zou, Y.; Woo, H. Y.; Neher, D.; Shoaee, S. Quantifying Quasi-Fermi Level Splitting and Open-Circuit Voltage Losses in Highly Efficient Nonfullerene Organic Solar Cells. *Sol. RRL* **2020**, 2000649.

(9) Pranav, M.; Benduhn, J.; Nyman, M.; Hosseini, S. M.; Kublitski, J.; Shoaee, S.; Neher, D.; Leo, K.; Spoltore, D. Enhanced Charge Selectivity via Anodic-C60 Layer Reduces Nonradiative Losses in Organic Solar Cells. *ACS Appl. Mater. Interfaces* **2021**, *13* (10), 12603–12609.

(10) Tokmoldin, N.; Vollbrecht, J.; Hosseini, S. M.; Sun, B.; Perdigón-Toro, L.; Woo, H. Y.; Zou, Y.; Neher, D.; Shoaee, S. Explaining the Fill-Factor and Photocurrent Losses of Nonfullerene Acceptor-Based Solar Cells by Probing the Long-Range Charge Carrier Diffusion and Drift Lengths. Adv. Energy Mater. 2021, 2100804.

(11) Marin-Beloqui, J.; Zhang, G.; Guo, J.; Shaikh, J.; Wohrer, T.; Hosseini, S. M.; Sun, B.; Shipp, J.; Auty, A. J.; Chekulaev, D. Insight into the Origin of Trapping in Polymer/Fullerene Blends with a Systematic Alteration of the Fullerene to Higher Adducts. J. Phys. Chem. C 2021.

(12) Alqahtani, O.; Hosseini, S. M.; Ferron, T.; Murcia, V.; McAfee, T.; Vixie, K.; Huang, F.; Armin, A.; Shoaee, S.; Collins, B. A. Evidence That Sharp Interfaces Suppress Recombination in Thick Organic Solar Cells. ACS Appl. Mater. Interfaces 2021, 13 (47), 56394–56403.

Publications included in this thesis

(1) **Hosseini, S. M.**; Roland, S.; Kurpiers, J.; Chen, Z.; Zhang, K.; Huang, F.; Armin, A.; Neher, D.; Shoaee, S. Impact of Bimolecular Recombination on the Fill Factor of Fullerene and Nonfullerene-Based Solar Cells: A Comparative Study of Charge Generation and Extraction. *J. Phys. Chem. C* **2019**, *123* (11), 6823–6830. https://doi.org/10.1021/acs.jpcc.8b11669.

The publication is incorporated in **Chapter 4.**

Personal Contribution:

Main idea (80%)

Performed experiments (100%)

Fabricated devices (100%)

Result Interpretation (50%)

Drafted the paper (40%)

Manuscript editing/optimization (80%)

(2) **Hosseini, S. M.**; Tokmoldin, N.; Lee, Y. W.; Zou, Y.; Woo, H. Y.; Neher, D.; Shoaee, S. Putting Order into PM6:Y6 Solar Cells to Reduce the Langevin Recombination in 400 Nm Thick Junction. *Sol. RRL* **2020**. https://doi.org/10.1002/solr.202000498.

The publication is incorporated in **Chapter 5.**

Personal Contribution:

Main idea (80%)

Performed experiments (100%)

Fabricated devices (100%)

Result Interpretation (80%)

Drafted the paper (80%)

Manuscript editing/optimization (80%)

(3) Tokmoldin, N.; **Hosseini, S. M.**; Raoufi, M.; Phuong, L. Q.; Sandberg, O. J.; Guan, H.; Zou, Y.; Neher, D.; Shoaee, S. Extraordinarily Long Diffusion Length in PM6:Y6 Organic Solar Cells. *J. Mater. Chem. A* **2020**, *8* (16), 7854–7860. https://doi.org/10.1039/d0ta03016c.

The publication is incorporated in **Chapter 6.**

Personal Contribution:

Main idea (40%)

Performed experiments (50%)

Fabricated devices (100%)

Result Interpretation (30%)

Drafted the paper (30%)

Manuscript editing/optimization (20%)

(4) Shoaee, S.; Armin, A.; Stolterfoht, M.; **Hosseini, S. M.**; Kurpiers, J.; Neher, D. Decoding Charge Recombination through Charge Generation in Organic Solar Cells. *Sol. RRL* **2019**, *3* (11), 1900184. https://doi.org/10.1002/solr.201900184.

The publication is incorporated in **Chapter 7.**

Personal Contribution:

Main idea (20%)

Performed experiments (100%)

Fabricated devices (80%)

Result Interpretation (30%)

Drafted the paper (20%)

Manuscript editing/optimization (20%)

Contents

Chapter 1. Introduction

1.1 Renewable Energy

Increasing the energy demand and, simultaneously, raising concerns for the environment have been caused mankind's attention to be focused on renewable energy. Such that, in 2019, more than 200 gigawatts of installed power from renewable energy sat the biggest record.[1] Among the renewable energy sources, solar energy in particular photovoltaic is the most promising technology due to its large theoretical potential (supplying 6000 times larger than the global annual energy consumption[2]). Therefore, the research institutes, as well as companies, have been looking for understanding the physics behind photovoltaics.

1.2 Organic Photovoltaic

Organic photovoltaics (OPV) have attracted widespread attention over the last two decades as a unique renewable energy generation technology. One of the main reasons is that their performance continues to improve with a large diversity of materials. Using OPVs can potentially reduce the cost of fabrication and enable producing non-toxicity products with light-weight and flexible.

1.3 Motivation: History of Organic Solar Cells

The starting point of photovoltaics dates back to 1839 when the French physicist Alexandre Edmond Becquerel observed the effect of light on a cell made up of two metal electrodes in an acidic solution.[3] In 1906, Pochettino studied the solid anthracene which was the first organic component with photoconductivity property.[4] Then, the milestone of systematic research on the fundamental processes such as photo excitation and charge transport properties was in the 1960s when Pope et al. investigated the electroluminescence of anthracene crystal.[5,6] Later, the first organic solar cell consisted of a single, pure organic layer sandwiched between two electrodes with different work functions was fabricated by Tang and Albrecht; however, its power conversion efficiency (PCE) did not exceed 0.001%.[7]

In order to overcome the impediment of the strong exciton binding energy, in 1986, a bilayer solar cell consists of a donor (copper phthalocyanine) and an acceptor (perylene tetra carboxylic) organic compounds with PCE of 1% was introduced by Tang.[8] However, in this planar heterojunction (PHJ), a few photo-generated excitons have a chance to reach the donor-acceptor interface due to the short exciton diffusion length, and the exciton dissociation yield reduces. To prevail over this major disadvantage of PHJ, in 1995, the concept of bulk heterojunction (BHJ) was introduced.[9,10] In the BHJ, a Donor is well intermixed with an

acceptor on nano-meter scale to form an interpenetrating network morphology which facilitates the exciton dissociation, approaching 100%; however, the complete charge carrier separation and transportation in the more disordered bulk system are still the main challenges to achieve high PCEs. During the two last decades, various strategies such as attempting to control the morphology of the active layer, engineering of the interfacial layers, synthesizing of new materials with unique properties[11,12], etc. have been utilized. Such that in the following decade the PCE constantly increased and exceeded over 18%.[13–17] However, the active layer thickness of these optimum devices is limited to around 100 nm and by increasing the active layer thickness, which is more favorable for commercialization of OPVs, the PCE drops. Mainly this drop is due to the reduction in the fill factor (FF) which is a measure of quality of the solar cell. This essential parameter is calculated by comparing the ratio of maximum obtainable power to the product of the open circuit voltage and short circuit current (see section 2.4 for more details). In fact, the competition between charge extraction and recombination peaks at the maximum power point, which determines the FF (which will be further discussed in section 2.5).

This motivated the main goal of this thesis, namely to improve the fundamental understanding of the FF (which will be addressed in chapters 4 and 7) and answer these two questions: why does the FF drop through increasing the active layer thickness? and how to prevent this reduction? (which will be addressed in chapters 5 and 6)

Chapter 2. Physics of organic semiconductors

2.1 Conjugated Molecules

Organic materials are based on carbon compounds, hydrocarbons, or their derivatives and they could include any number of other elements, e.g. sulfur, oxygen, or nitrogen. The main component, the element carbon (C), has six electrons with its ground state electron configuration $1s^2\ 2s^2 2p^2$. The s-orbitals of the first and second shells are fully occupied by two electrons. The two remaining electrons are found in two of the three degenerate p-orbitals ($2p_x$, $2p_y$, and $2p_z$), each by one electron according to Hund's rule, which leads to $1s^2\ 2s^2 2p_x^1 2p_y^1$. These four electrons in the outer shell, named valance electrons, play the role in the electric properties of organic materials. To make a stable bond with another atom, the atom tries to achieve a noble gas configuration; therefore, these four electrons fill the $2p_z$ and three $2sp^2$ (which are formed by the linear combination[18] of 2s, $2p_x$, and $2p_y$) orbitals, each by one electron (see Figure 1.1). Now if two carbon atoms are adjacent to each other, the sp^2 orbitals overlap and form sigma (σ) bonds which are either bonding (σ) or anti-bonding (σ^*), depending on the sign of the combination. These σ-bonds are covalent and strongly localized electron densities such that they do not contribute to charge transport. On the other hand, the perpendicular p_z orbital of each carbon atoms remain unchanged. These p_z orbitals overlap in a region out of the plane and form pi (π) bonds, which are again bonding (π) or anti-bonding (π^*), depending on the phase overlap. More neighbor carbon atoms, more bonding, and anti-bonding π-orbitals (slightly shifted in the energy, see Figure 1.1.b) become involved until a conjugated C=C–C=C–C chain is built up. According to the 1 dimension (1D) quantum well model, this conjugated chain, comprising equally spaced C-H fragments, should be 1D metal with no energy gap. However, Peierls distortion[19,20] suggests that 1D metal cannot exist which leads to an alternation of the double-bond across the polymer chain and create a band gap between the highest occupied molecular orbital (HOMO) the lowest unoccupied molecular orbital (LUMO) as illustrated in Figure 2.1b.

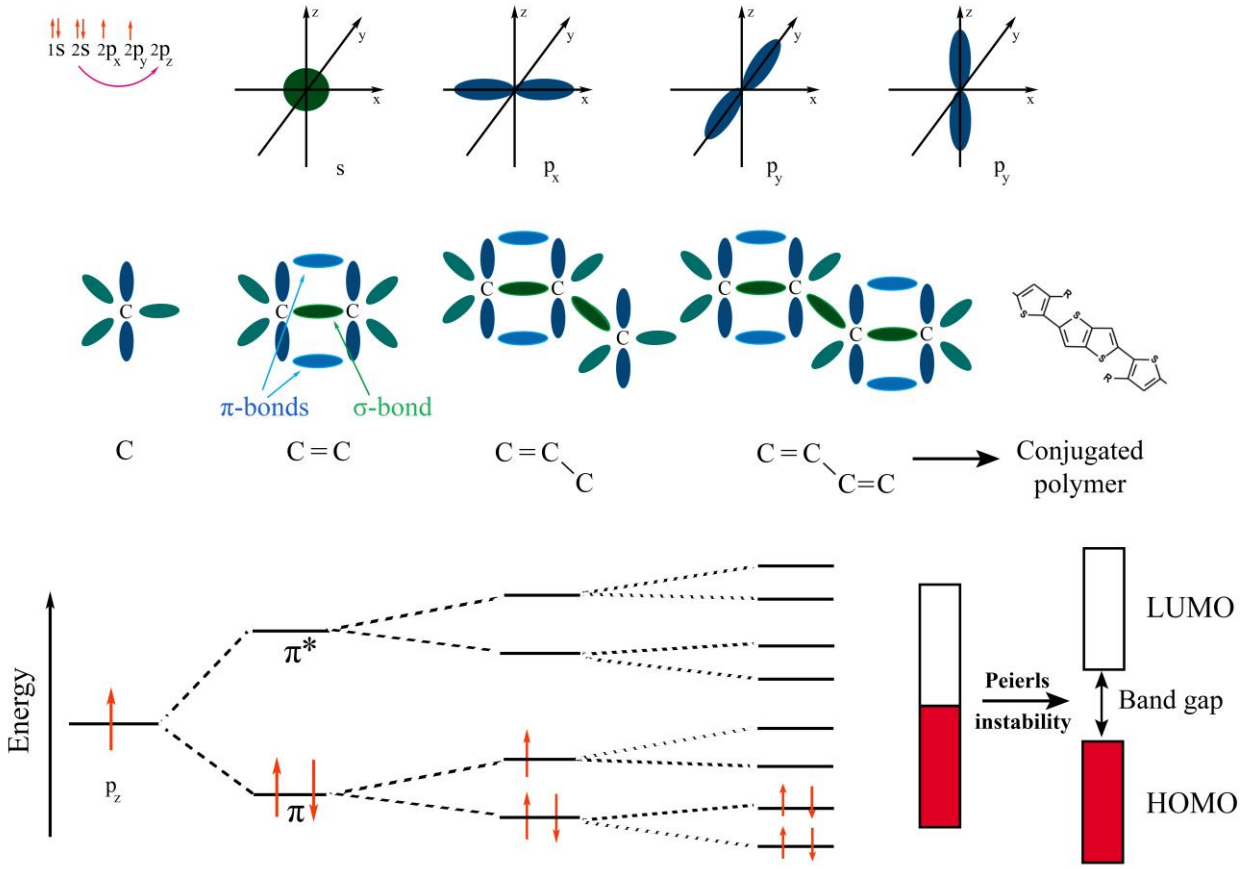

Figure 2.1. a) electronic configuration of a carbon atom and its orbitals, b) formation of $2sp^2$ orbitals and its energy diagram from a single carbon atom to a conjugated polymer with alternating single and double bonds between carbon atoms, called dimerization[19], which creates an energy gap at the Fermi level and splits the expected metal band into an occupied (HOMO) and an unoccupied (LUMO) band.

2.2 Disorder Charge carrier mobility

Intrinsically disordered systems with low mobility as well as low dielectric constant are known to be characteristic of organic semiconductors. These properties, in organic BHJ solar cells, limit the charge transport between localized states such that each molecule (or π-system) constitutes a hopping site with a transition probability to a neighboring π-system. In 1960 Miller and Abrahams[21] introduced a model, named variable range hopping (VRH), to describe the hopping transport of electrons, in inorganic semiconductors, from occupied to unoccupied localized donor states. In this model, the jump rate from site i to j with E_i and E_j site energies, respectively, (by assuming $E_j - E_i > k_B T$) is describe by:

$$\nu_{ij} = \nu_0 \exp(-2\xi\Delta R_{ij}) . \begin{cases} \exp\left(-\frac{E_j - E_i}{k_B T}\right); & E_i > E_j \\ 1; & E_i < E_j \end{cases} \quad (2.1)$$

where k_B is Boltzmann's constant, T is temperature, the prefactor ν_0 is the attempt frequency which the electron tries a jump with, ΔR_{ij} is the site distance and ξ is the wave function decay parameter. However, this model neglects the polaronic effect; hence, the Marcus model would be an appropriate theory to explain the electron transfer in a hopping regime given by:

$$\nu_{ij} = \frac{2\pi I_{ij}^2}{h}\sqrt{\frac{\pi}{\lambda k_B T}}\exp\left(-\frac{(E_j - E_i + \lambda)^2}{4\lambda k_B T}\right) \quad (2.2)$$

where I_{ij}^2 is the electronic coupling and λ is the reorganization energy, covering polarization effects upon charging or discharging a molecule.

In 1993, Bässler [22] Introduced a model for disordered single or multiple components organic solid, denoted as Gaussian disorder model, so that charge transport is described with the hopping sites energy distribution g(E) given by:

$$g(E) = \frac{1}{\sqrt{2\pi\sigma^2}}\exp(-\frac{E^2}{2\sigma^2}) \quad (2.3)$$

where E is the energy related to the center of the density of state with the width of σ, denoted as the energetic disorder that originates from the fluctuation of the lattice polarization energies and/or the distribution of segment length in π- or σ-bonded main chain polymer. In this picture, the mobility of charge carriers depends on temperature, energetic disorder, and electric field *F* as expressed by:

$$\mu(T, \sigma, F) \propto \exp[-\left(\frac{2\sigma}{3k_B T}\right)^2]\sqrt{F} \quad (2.4)$$

For a more extensive review on charge transport please see the references [23,24]. In this work, we have shown how the energetic disorder affects not only the mobilities in non-fullerene based OSCs but also the bimolecular recombination such that reducing both the energetic and structural disorder enhance the charge carrier mobilities and also suppress the bimolecular recombination, toward having a non-Langevin system, see chapter 5 for more details.

2.3 Working Mechanism: from light absorption to charge extraction

The device architecture of an organic solar cell (OSC) has been shown in Figure 2.2. The active layer, based on a combination of electron donor (D) blended with an acceptor (A) in the form of BHJ, has been sandwiched between a hole transport layer (HTL) and an electron transport layer (ETL). The energy levels position at the interface of HTL/ETL and the active layer should be favorable for fast exciton dissociation followed by charge separation. All layers (one by one) are spin coated on a transparent conductive oxide, deposited on a glass substrate, and then the sample is finalized by evaporating a top metal contact. These two electrodes (ideally ohmic contacts with the HTL and ETL) are responsible for charge collection.

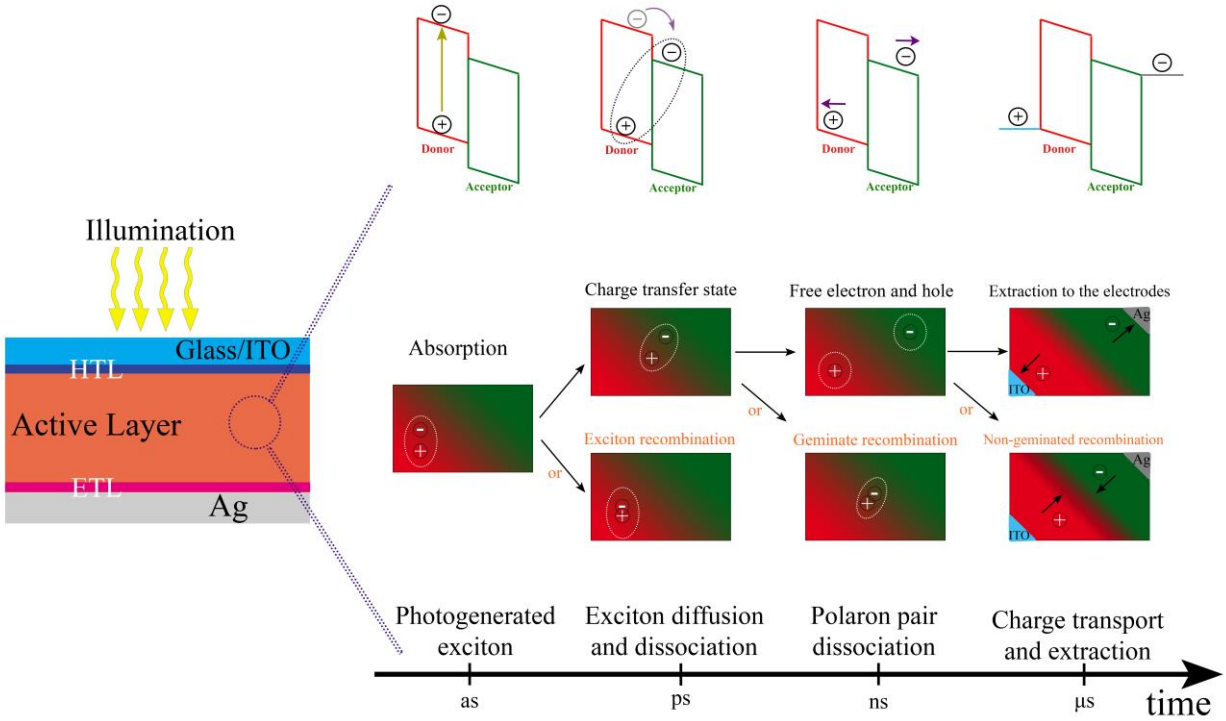

Figure 2.2. Left side, the device structure of an OSC. The middle and the right sides, the scheme of the four crucial physical processes of photocurrent generation at different time scales with the energy diagram of the donor-acceptor interface.

Figure 2.2 sketches all the key steps of photocurrent generation involved Ⅰ) photon absorption and exciton generation, Ⅱ) exciton diffusion and dissociation, Ⅲ) polaron pair dissociation, and Ⅳ) charge transport and extraction.

Ⅰ - Photon Absorption and Exciton Generation

The first step of photocurrent generation is to absorb photons in the active layer. Usually, organic materials show Ⅰ) a very broad absorption due to the significant geometry relaxations that take place in the excited states (the width of the absorption bands can reach over 1 eV)[25], and Ⅱ) a high absorption coefficient (e.g. in contrast with inorganic materials)[26] such that 100-200 nm active layer thicknesses are sufficient for the absorption in the wide range of sun spectrum from visible to near-infrared. Photon absorption can occur in the D or both D and A materials with excitation of electrons from the HOMO to the LUMO level, which leads to exciton generation, at attosecond (as) time scale.

Ⅱ - Exciton Diffusion and Dissociation

After exciton generation, the excitons need to be dissociated in order to have separated charge carriers for producing a photocurrent; however, they are Coulombically bound. The Coulomb attraction between two charges is given by:

$$E_C = \frac{e^2}{4\pi\varepsilon_0\varepsilon_r r} \quad (2.5)$$

where e, ε_0, ε_r and r are elementary charge, the permittivity of vacuum, the dielectric constant of the surrounding medium, and the distance between the electron-hole pair; respectively. The Coulomb interaction causes a binding energy for the exciton and in OSCs due to low dielectric constant ($\varepsilon \approx 3$ - 4), this binding energy is usually large (0.3 to 1 eV) in comparison with thermal energy $k_B T$ (0.025 eV). Therefore, at room temperature, a small exciton diffusion length (5-10 nm)[27], which is the distance where the exciton travels during its lifetime, leads to exciton relaxation. However, if the domain size of the donor and the acceptor in the BHJ device are small enough the electrons can reach the donor-acceptor interfaces before relaxation. Once the electron is at the interface, it can be transferred into the LUMO level of the acceptor. This is known as exciton dissociation or charge transfer (CT) formation which occurs around picosecond (ps) time scale as shown in Figure 2.2.

Ⅲ- Polaron Pair Dissociation

The electron or hole in combination with the polarization due to changes in the surroundings is commonly called a negative or positive polaron, respectively. When CTS formation takes place, the electron and hole reside on adjacent molecules and are denoted as polaron pairs in the CTS which is still Coulombically bound. Now, the polaron pair has two competing pathways: Ⅰ) the electron and hole recombine, called geminate recombination (will be discussed in section 2.6.1), due to Coulomb interaction or Ⅱ) they overcome the Coulomb binding energy and polaron pair dissociation occurs. In-state of the art, in most OSCs in form of BHJ, efficient polaron pair dissociation has been observed which might be correlated with some specific aspects of organic semiconductors, e.g. energetic disorder[28], high local charge carrier mobilities[29,30] because of delocalized charge carriers within conjugated segments of the polymer chain or electrostatic interfacial field[31].

Ⅳ- Charge Transport and Extraction

The last step is the transport of electron and hole (polarons) towards their respective electrodes. However, in a BHJ, electrons and holes can encounter each other during their transport and recombine non-geminately (it will be discussed in section 2.6.2 in more details); therefore, an efficient charge transport will be achieved if the charge carrier transit (extraction) time is shorter

than the charge carrier lifetime. This restricts the active layer thickness to typically on the order of 100 nm with a high efficiency[11,12]. On the other hand, if the lifetime is longer than the extraction time, increasing the active layer thickness doesn't affect the efficiency of charge transport, leading to a Non-Langevin system (see section 2.6.2.1). In addition, the existence of interlayers (HTL and ETL) before and after the active layer, enhances charge transport toward the electrodes through creating selective contacts. These selectively contacts hinder the transport of the opposite charges toward the wrong electrodes[32,33]; as a result, this reduces another type of recombination, named surface recombination[34–36].

2.4 Photovoltaic Conversion Efficiency

The overall efficiency (so-called external quantum efficiency (EQE)) is obtained from the efficiency (η) of the four aforementioned steps.

$$EQE = \eta_{Abs}.\eta_{Exc}.\eta_{CT}.\eta_{Ext} = \eta_{Abs}IQE \quad (2.6)$$

where η_{Abs}, η_{Exc}, η_{CT} and η_{Ext} are the efficiency of absorption, exciton dissociation, CT dissociation, and charge extraction. The EQE gives the number of collected charges per incident photon (can be measured experimentally, see section 3.5), while the internal quantum efficiency (IQE) gives the number of collected charges per absorbed photon (can be obtained upon knowing the active layer absorption spectrum, see section 3.3).

The quantity that describes the operation of solar cell devices is denoted by power conversion efficiency (PCE) which is the ratio of maximum provided electrical power density (P_{max}) to the incident light power density (P_{in}).

$$PCE = \frac{P_{max}}{P_{in}} \quad (2.7)$$

In order to obtain the PCE, the current density-voltage (*J*-V) characteristics of the solar cell device are recorded under simulated one sun illumination, air mass (AM)1.5 condition by a solar simulator. AM is the path length of sunlight through the atmosphere relative to the shortest way from the zenith to the ground. AM1.5, corresponding to an angle of incidence of 48°, is chosen as the standard spectrum for solar cell characterization[37] and the integral over AM 1.5 is 1 kW m^{-2} = 100 mW cm^{-2}. This value is approximately reached, e.g., in Münsingen in southern Germany at noon at an equinox, i.e. on the 21st of March and the 23rd of September. As illustrated in Figure 2.3, in a typical *J*-V curve of a solar cell device, there are three important points.

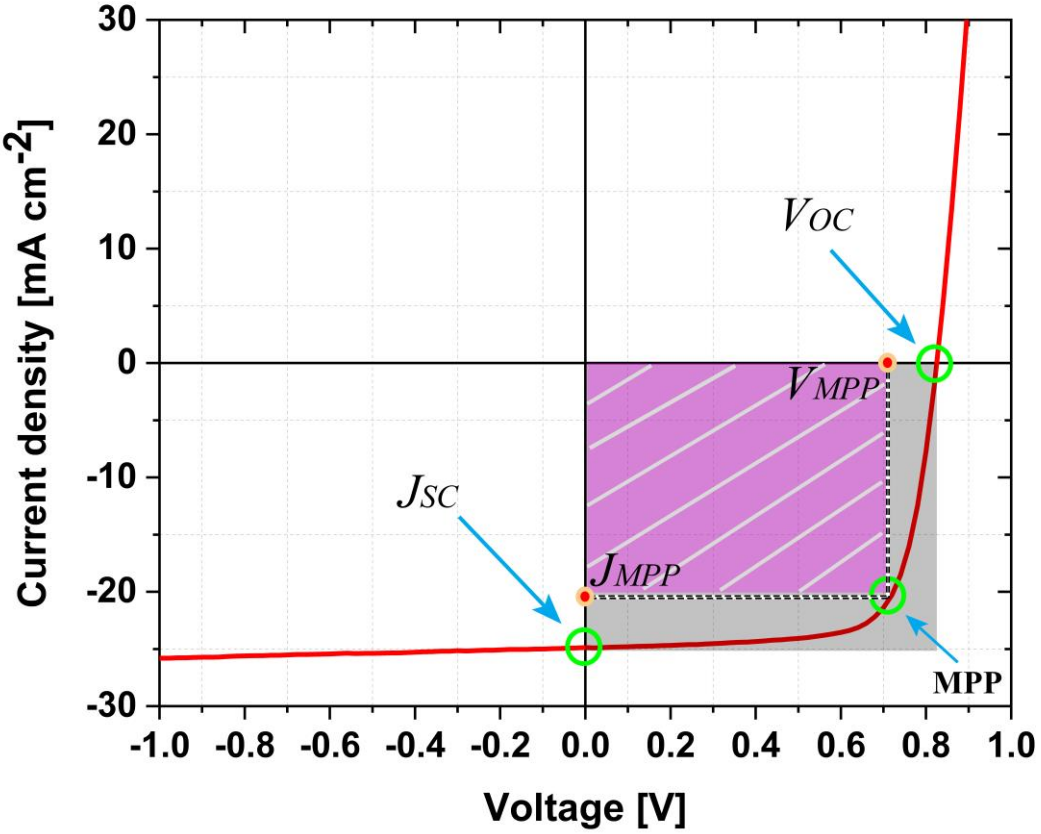

Figure 2.3. current density-voltage characteristics of a typical solar cell device under one sun illumination.

- J_{SC}: short circuit current density which is the current density at zero volt.
- V_{OC}: open circuit voltage which is the maximum voltage a solar cell can produce and it is limited by the energy levels of the HOMO level of the donor and the LUMO level of the acceptor.
- MPP: maximum power point is optimum operation point where the product of current density and voltage is maximized (J_{MPP} and V_{MPP}, respectively).

The MPP can be expressed as a function of J_{SC} and V_{OC} with the FF as a proportionality constant such that:

$$P_{max} = J_{MPP}.V_{MPP} = J_{SC}.V_{OC}.FF \quad (2.8)$$

where FF is a quality factor and expresses the squareness of the *J*-*V* curve; therefore, the PCE can be rewritten as:

$$PCE = \frac{P_{max}}{P_{in}} = \frac{J_{SC}.V_{OC}.FF}{P_{in}} \quad (2.9)$$

In order to achieve high PCE, an understanding of the physics behind these parameters is required.

2.5 Shockley-Queisser limit / Model for Fill Factor

Over recent years, a lot of research has been done on a good understanding of the physical phenomena determining J_{SC} [38,39], V_{OC}[40–42], and FF[43,44]. On the other hand, most OSCs suffer from a modest FF and high voltage losses in the V_{OC} which reduce the overall PCE.[45] Herein, we address the FF and V_{OC} (in section 2.6.3) in more details. In 1960, Shockley and Queisser (SQ) proposed a model to calculate the upper limit for the efficiency of a p-n junction solar cell, based on the principle of detailed balance[46] (see section 2.6.3 for more details). Such that according to this model, the FF is approximately expressed by[47]:

$$FF_{ideal} \approx \frac{\frac{eV_{OC}}{n_{id}k_BT} - ln\left(1+\frac{eV_{OC}}{n_{id}k_BT}\right)}{1+\frac{eV_{OC}}{n_{id}k_BT}} \tag{2.10}$$

where n_{id} is the ideality factor. In 2016, Neher et al.[44] proposed an analytical model based on modified SQ theory to determine the FF in OSCs as:

$$FF = \frac{\frac{eV_{OC}}{(1+\alpha)k_BT} - \ln\left(0.79+0.66\left[\frac{eV_{OC}}{(1+\alpha)k_BT}\right]^{0.5}\right)}{1+\frac{eV_{OC}}{(1+\alpha)k_BT}} \tag{2.11}$$

where α is a dimensionless parameter defined by:

$$\alpha^2 = \frac{e^2 k_{eff} G d^4}{4\mu_e \mu_h (k_B T)^2} \tag{2.12}$$

where k_{eff}, G, d, μ_e and μ_h are bulk (or effective) recombination, generation rate, thickness, electron mobility, and hole mobility, respectively. According to this model, the competition between charge extraction and bimolecular recombination (will be discussed in the following section) determines the FF. Such that under ideal conditions ($\alpha \ll 1$), the charge extraction is dominant and the solar cell acts as a Shockley-type diode; however, for $\alpha > 1$, bimolecular recombination dominates. In this case, the photocurrent becomes transport-limited, as shown in Figure 2.4.

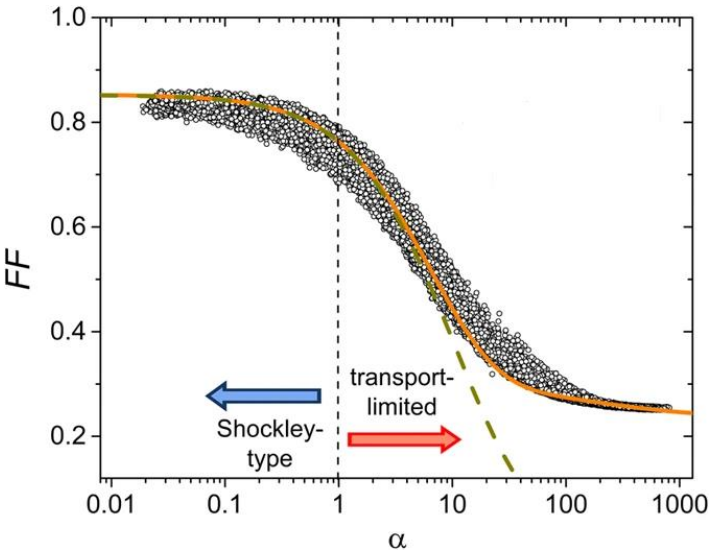

Figure 2.4. FF as a function of α. The gray points are from simulated *JV*-curves with balanced mobilities and V_{OC} between 0.7 and 0.9 V.[44]

2.6 Recombination

The recombination of photogenerated species may occur Ⅰ) after exciton formation and diffusion to the D-A interface, Ⅱ) after CTS formation, or Ⅲ) after CTS dissociation. Type Ⅰ is the recombination of an electron with a hole resulting from one photo-excitation, so-called geminate recombination. Type Ⅱ which happens at the D/A interface, again called as geminate recombination, can be either radiative or non-radiative (it will be discussed further in the next section). On the other hand, type Ⅲ which is the recombination of dissociated charge carriers generated by different absorption photons. These dissociated charge carriers can encounter one another to reform CTS and decay back to the ground state. This is referred to as non-geminate (or bimolecular) recombination. In addition, when charge carriers recombine at the wrong electrode, that is referred to as surface or interfacial recombination. In the following sections both geminate and non-geminate recombination will be addressed in details.

2.6.1 Geminate Recombination

In 1938, Onsager proposed a model to describe the probability of the separation of photogenerated Coulomb bound pair of ions in a weak electrolyte, calculated from the laws of Brownian motion.[48] In this model, a hot electron and a localized hole are generated by photon absorption with an energy of $h\nu$. Subsequntly the hot electron is thermalized at distance a (thermalization length) from the localized hole, forming first excited state. Onsager defined the Coulomb capture radius (also called the Onsager radius) as the distance at which the Coulomb attractive potential energy equals the kinetic thermal energy (k_BT) such that:

$$r_C = \frac{e^2}{4\pi\varepsilon_0\varepsilon_r k_B T} \tag{2.13}$$

As illustrated in figure 2.4, If the thermalization length is greater than Onsager radius ($a > r_C$), first excited state can be thermally dissociated; otherwise, it geminately recombines, which is common in OSCs because of the low dielectric constant ($\varepsilon_r \approx 3-4$). Then the probability of the geminate recombination is expressed with $1 - P(E)$, where $P(E)$ is field-dependent escape probability[49]:

$$P(E) = \exp\left(\frac{-r_c}{a}\right)\left(1 + \frac{e r_c}{2k_B T}E\right) \tag{2.14}$$

where E is the strength of applied electric field.

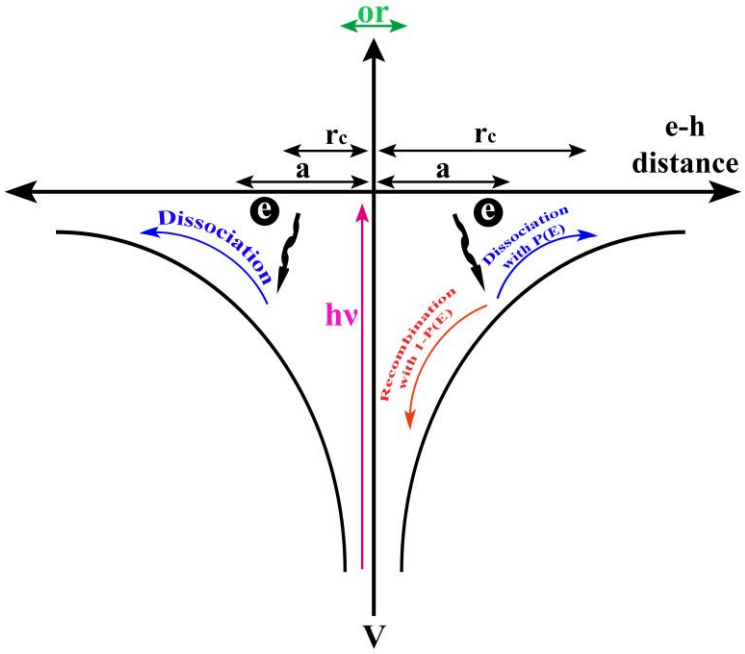

Figure 2.4. Potential energy diagram summarizing Onsager theory. Photoexcitation (with $h\nu$ energy) generates a hot mobile electron, which thermalizes at distance a from the localized hole. Then, if the Onsager radius is smaller than a, dissociation into free charge carriers will take place; on the other hand, if Onsager radius is greater than a, electron and hole can either undergo geminate recombination or dissociate into free charge carriers.

Onsager theory contains a boundary condition such that the recombination of polaron pairs occurs when the distance between two ions becomes zero, and this process is irreversible. However, in 1983, Braun claimed that this condition is not appropriate due to the finite lifetime of the CT state.[50] Therefore, he proposed an extended version of Onsager model with two decay processes for CT sate: Ⅰ) $k_d(E)$, the electric field dependent dissociation rate into free carriers and Ⅱ) k_f, geminate recombination rate back to the ground state. According to his work, the escape probability is given by:

$$P(E) = \frac{k_d(E)}{k_d(E)+k_f} = k_d(E)\tau(E) \quad (2.15)$$

where $\tau(E)$ is the lifetime of CT state which is a reversible process.

While this model is successfully used in some OSCs[51,52], the model describes a simplified situation and it doesn't include some features of OSCs such as energetic disorder, high local charge carrier mobilities, or electrostatic interfacial field as discussed in section 2.3, part Ⅲ. For a more extensive review on polaron pair dissociation please see references[29,36,53].

2.6.2 Non-Geminate Recombination

The non-geminate recombination is based on meeting oppositely charge carriers, originate from different photons, after CT dissociation so that free charge carriers return back to the CT interface, forming the CTS, and then *"geminately"* recombine back to the ground state. This type of recombination has a huge impact on the device performances of OSCs.

2.6.2.1 Langevin and Non-Langevin Systems

In 1903, Paul Langevin introduced a model to describe recombination dynamics of two opposite ions in a large reservoir.[54] According to his model, the recombination occurs if two opposite charges approach each other to a distance less than the Coulomb capture radius. In this picture, the recombination rate is given by:

$$R = k_L\,(np - n_{int}p_{int}) \quad (2.16)$$

where $n(p)$ is the free electron (hole) density, $n_{int}(p_{int})$ is the intrinsic electron (hole) density and k_L is the Langevin recombination constant:

$$k_L = (\mu_h + \mu_e)\frac{e}{\varepsilon_r\varepsilon_0} \quad (2.17).$$

This model can be applied for organic BHJ solar cells by assuming the donor and acceptor phases as two reservoirs; however, the charge recombination exclusively occurs at the donor-acceptor interface and as a result, the morphology of the active layer can play a significant role. In addition, in this model, it is assumed that charge carrier transport is homogeneous through the bulk and electron and hole densities are nonfluctuating and uncorrelated. This assumption might be valid in crystalline semiconductors; however, in low mobility disordered materials such as organic BHJ solar cells where charge transport occurs through percolated pathways, charge transport is inhomogeneous, violating the assumption. Also, Langevin assumed that all charges entering the Coulomb-radius recombine, which is not true. Therefore, k_{eff} departs from the recombination predicted by Langevin theory into $\frac{k_L}{\gamma}$, where γ is the reduction factor. Numerous experimental and theoretical work has been done in order to calculate and explain this reduction factor; herein, I will discuss some of them.

Spatial Fluctuation in The Potential Landscape

In 1997, Arkhipov and Adriaenssens[55] formulated a model to explain the reduction factor in disorder materials. They considered random spatial fluctuations of the potential landscape, leading to spatially separated percolation pathways for transport of electrons and holes, by this assumption: the characteristic length of the spatial fluctuations should be larger than the carrier localization radius. According to this model, recombination can occur only because of the weak overlap of the electron and hole densities, given by:

$$k_{eff} = k_L \frac{2\pi\Delta_E}{k_B T} \exp(-\frac{2\Delta_E}{k_B T}) \quad (2.18)$$

where Δ_E is the characteristic amplitude of the potential fluctuations. This model explained the suppressed non-geminate recombination in hydrogenated amorphous silicon (a-Si:H) as a disorder material.

Slowest Carriers Dominate Recombination

In 2006, Koster and his coworkers[56] claimed that Langevin theory doesn't hold for polymer-fullerene BHJ solar cells. As the charge carrier recombination takes place at the interface of D-A, therefore if the slower charge carrier does not reach the interface, the recombination process does not occur. Hence, they introduced a modification to the Langevin model by replacing the $(\mu_h + \mu_e)$ with the minimum mobility,

$$k_{eff} = \min(\mu_h, \mu_e) \frac{e}{\varepsilon_r \varepsilon_0} \quad (2.19)$$

Their extension justified the suppressed recombination in poly(3-hexylthiophene) (P3HT) blended with 6,6-phenyl C61-butyric acid methyl ester (PCBM[60])[56] and also in poly(2-methoxy-5-(2'-ethylhexyloxy)-1,4-phenylene vinylene) (MDMO-PPV) blended with PCBM[60][57].

However, the Koster and Arkhipov models cannot predict correctly the temperature dependence of the reduction factor of the recombination rate:

$$\zeta = \frac{R}{R_{exp}} \quad (2.20)$$

where R_{exp} is the experimentally determined recombination rate. In those models, a positive temperature dependent of ζ was predicted; however, Deibel and Wagenpfahl[58] in 2009, showed a negative temperature coefficient in the annealed P3HT:PCBM device.

Non-zero Separation with a Finite Intrinsic Recombination Rate

According to the Langevin model, recombination of an electron and hole occurs when the distance between charges, R, is zero. In 2010, Hilczer and Tachiya[59] claimed that charge carriers can recombine even at non-zero distance with a finite intrinsic recombination rate. They

proposed a formula to show how various physical parameters, such as the intrinsic recombination rate, the diffusion coefficients (D) of electrons and holes and the Onsager radius the suppressed Langevin recombination:

$$\gamma = \frac{k_L}{k_{eff}} = 1 - e^{\frac{-r_c}{R}} + \frac{Dr_c}{pR^2} e^{\frac{-r_c}{R}} \quad (2.21)$$

where p is the intrinsic reactivity parameter, which is given by $p = k_{BCT}R$ where k_{BCT} is back charges transfer rate to the original distance (R) after separation to certain distances. Such that the higher reduction of back charges transfer rate leads to increase the suppression of Langevin recombination, as experimentally reported by Schwarz et al.[60] This theory can be helpful in order to reduce bimolecular recombination in OSCs by optimizing the physical parameters.

Encounter-Limited Regime

In 2015, Heiber et al.[61] simulated the Langevin recombination for OSCs with different domain sizes (from 5 to 55 nm), 100 morphologies for each domain sizes, and charge carrier mobilities. In their study, for the small domain sizes (5 nm), the recombination coefficient follows the Langevin model; however, by increasing the domain sizes deviation from the Langevin model was observed. This deviation was noted to depend on the charge carrier mobilities such that, in the extreme cases, for a system with imbalanced mobilities, slow carriers are not accessible for the opposite charges and they have to travel through the domains in order to reach the interface for recombination. Therefore, the recombination coefficient will be dominated by slower (faster) carriers if charge carriers are far from (close to) the interface. In other words, by changing the domain size, the critical parameter is in the average distance between the charge carriers and the interface; as a result, it changes the mobility dependence. Hence, they proposed a recombination coefficient, depending on domain size and power mean of mobilities, as indicated in Figure 2.5, given by:

$$k_{enc} = \frac{e}{\varepsilon_r \varepsilon_0} f(d) 2 \left(\frac{\mu_e^g + \mu_h^g}{2}\right)^{\frac{1}{g}} \quad (2.22)$$

where *f(d)* and *g* are a domain-size-dependent prefactor and power mean exponent, respectively. For a very small domain size, $\lim_{d \to 0} f(d) = 1$ and $\lim_{d \to 0} g(d) = 1$, leading to Langevin expression.

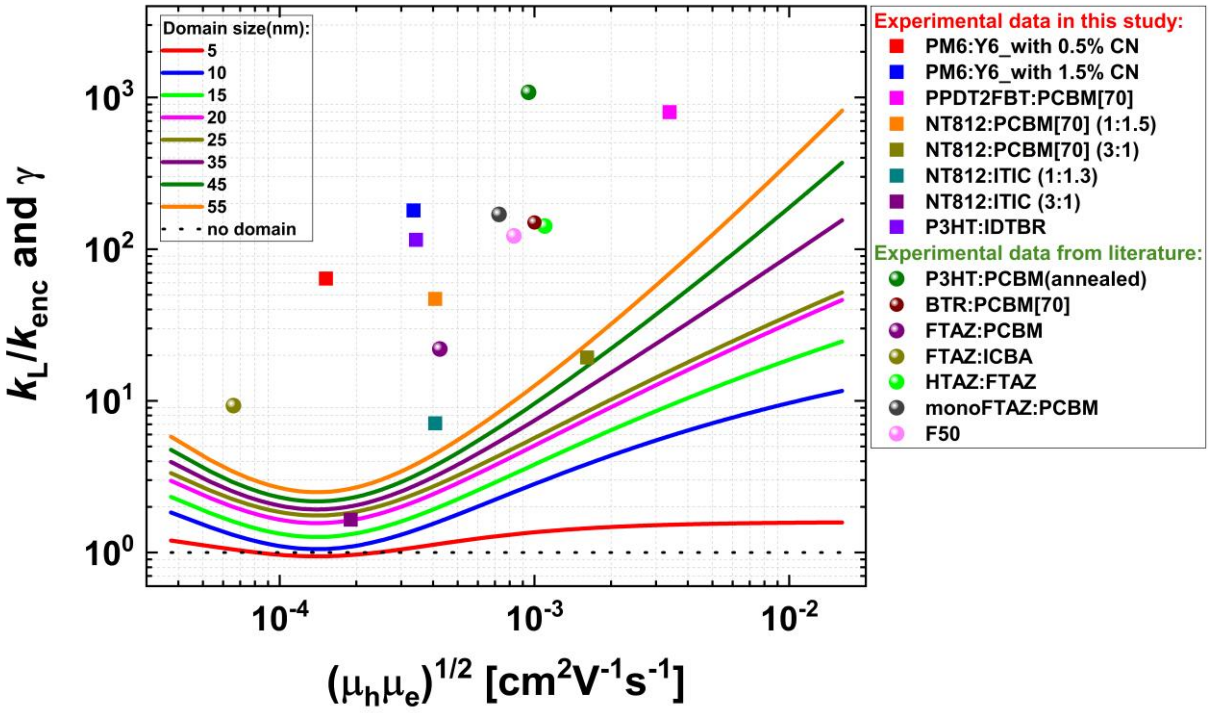

Figure 2.5. Simulated reduction factor of Langevin recombination, given by $\frac{k_L}{k_{enc}}$, at different domain sizes (colored lines, calculated based on Heiber et al.[61]) as a function of the square root of the mobilities. The measured Langevin reduction factor in this study (colored squares) and experimental data from literature[62–65] (colored circles).

Nevertheless, this simulation model cannot predict the reduction factor of many non-Langevin systems, as illustrated in Figure 2.5.

Kinetics of Charge Transfer State

In 2016, Armin et al.[63] claimed that the Langevin reduction factor includes two independent stages, I) the reduction due to the probability of the encounter between the free electron and hole (γ_{enc}) to form CTS as predicted by Heiber et al.[61] and II) the reduction due to probability of redissociation of CTS ($\gamma_{CT} = \frac{k_d(E)}{k_f} + 1$) as expressed by Braun[50]; Hence,

$$\gamma = \frac{k_L}{k_{eff}} = \gamma_{enc}\gamma_{CT} \tag{2.23}$$

He observed 150 times suppression of Langevin recombination coefficient in BTR:PCBM[70], such that by considering a domain size of 10 nm, he claimed that $\gamma_{enc} = 2$ and as a result γ_{CT} will be 75 times.

In chapter 7, we will discuss this further and show that the main reduction of Langevin recombination is due to the redissociation of CTS.

2.6.3 Radiative and Non-Radiative Recombination

Recombination of charge carriers through CTS can be either by the limitation of charge transport, which reveals in the field-dependent behavior of *J-V* curve, leading a reduction in FF (see chapter 4), or by the energy dissipation of CTS, mostly leading to reduce V_{OC}, will be discussed in this following section.

Open Circuit Voltage Losses

When the solar cell is kept under open circuit condition, all photogenerated free carriers under steady state illumination recombine, and there is no net current at any point inside the device, leading to having a quasi-equilibrium state. Under this condition, V_{OC} is the maximum output voltage that the solar cell can produce. In 2003, Mihailetchi et al.[66] have shown that in non-ohmic contacts, the V_{OC} is correlated with the work function difference of two electrodes according to metal-insulator-metal (MIM) model, and in ohmic contacts, it depends on the HOMO level of the donor and LUMO level of the acceptor. In 2006, Scharber et al.[67] studied a series of OSC devices (26 polymer donor materials with different HOMO levels blended with a common acceptor, PCBM) and claimed that even an extended MIM model is not sufficient to describe the V_{OC}. They proposed an empirical equation which shows that V_{OC} is limited by the energy of HOMO level of the donor and LUMO level of the acceptor:

$$eV_{OC} = |E^{D}_{HOMO} - E^{A}_{LUMO}| - 0.3 \quad (2.24)$$

where the value of 0.3 V in the Equation is an empirical factor, expressing the voltage losses. Despite the fact that the optical band gap of OSCs (either donor or acceptor) is high enough, compared with the rival solar cells[68,69]; however, the voltage losses dominate reaching the high V_{OC}.[70] Now there are two questions: "What is the maximum value of V_{OC} predicted by theory? and how can this value be achieved experimentally?" To answer the first question, SQ model[46] is utilized in order to calculate the thermodynamic limit for the efficiency of organic BHJ solar cells[71,72], based on the principle of detailed balance between absorption and emission of light, indicating every microscopic process must have the same rate as its inverse process in thermal equilibrium. In this model, the solar cell assumes as a absorber with a step-function behavior:

$$\text{Absorptance: } \begin{cases} 1 \; above\; band\; gap \\ 0 \; below\; band\; gap \end{cases} \quad (2.25)$$

And also every photon creates one electron-hole pair which is able to reach the respective electrodes. Therefore, the short circuit current can be expressed as:

$$J_{sc,SQ} = e \int_{Eg}^{\infty} \varphi_{sun}(E).dE \quad (2.26)$$

where Eg and $\varphi_{sun}(E)$ are the band gap and the solar spectrum. On the other hand, in dark condition, the SQ model treats the solar cell as a black body and in the thermal equilibrium. In this situation, non-radiative recombination is assumed to be suppressed, and according to the detailed balance principle, the incident radiation from ambient must be in equilibrium with the emitted radiation from the device; therefore, the saturated current density is defined as:

$$J_{0,SQ} = e\int_{Eg}^{\infty}\varphi_{BB}(E).dE \tag{2.27}$$

where $\varphi_{BB}(E)$ is the black body spectrum, as formulated by Plank in 1901:

$$\varphi_{BB}(E)dE = \frac{2\pi}{h^3c^2}\frac{E^2}{\exp\left(\frac{E}{k_BT}\right)-1}dE \tag{2.38}$$

where h is the Planck constant, c is the vacuum velocity of light. Then the V_{OC} in the SQ limit is given by:

$$V_{OC,SQ} = \frac{k_BT}{e}\ln(\frac{J_{sc,SQ}}{J_{0,SQ}}+1) \tag{2.29}$$

However, in a real case the step-function is replaced by the photovoltaic external quantum efficiency spectrum (EQE_{PV}), leading to short circuit current density and radiative saturated current density:

$$J_{sc} = e\int_{Eg}^{\infty}EQE_{PV}(E).\varphi_{sun}(E).dE \tag{2.30}$$

and $J_{0,rad} = e\int_{Eg}^{\infty}EQE_{PV}(E).\varphi_{BB}(E).dE$ (2.31)

respectively. Then, the V_{OC} limited by the radiative recombination is given by:

$$V_{OC,rad} = \frac{k_BT}{e}\ln(\frac{J_{sc}}{J_{0,rad}}+1) \tag{2.32}$$

which is the maximum value of the V_{OC} predicted by theory. Now it turns to answer the second question: "Is this value achievable in a real solar cell?". To answer this question, the theory of detailed balance and reciprocity will be addressed here.

In 2007, Rau[73] has claimed that the photovoltaic diode not only converts photon energy into electricity, but also converts electric energy into photons. The reciprocity between these two opposite opto-electronic processes represents that a perfect solar cell would also be a perfect light emitted diode (LED) with electroluminescence external quantum efficiency close to unity:

$$EQE_{EL} = \frac{J_{em}}{J_{inj}} \tag{2.33}$$

where J_{em} and J_{inj} are radiative emission current and injection current, respectively, meaning that the injected charge carriers are all recombined and emitting photons in 100%. However, in reality, the $EQE_{EL} < 1$ and according to this theory, the difference between measured V_{OC} and V_{OC} limited by the radiative recombination ($V_{OC,rad}$) expresses the non-radiative voltage loss in a solar cell (see appendix A):

$$\Delta V_{OC,non-rad} = V_{OC,rad} - V_{OC} = -\frac{k_B T}{e} \ln(EQE_{EL}) \quad (2.34)$$

In 2017, Vandewal and his coworkers[74] have shown that non-radiative voltage loss in fullerene-based OSCs is intrinsic and correlated with the electron vibration coupling including two modes: Ⅰ) high frequency modes, related to hydrogen-carbon or carbon-carbon bonds and Ⅱ) low frequency mode, resulted from the deformation of molecules. They also derived through theory and shown experimentally that increasing the CT energy reduces the non-radiative voltage loss, as indicated for a large set of donor-fullerene material systems, experimentally in that work.

Chapter 3. Experimental Techniques

3.1 Organic Materials

In the last decade, a various range of organic materials has been utilized in the field of solar cells due to their attractive optical and electrical properties. Typically, these materials can be classified into three main types: a) electron donors b) electron acceptors, and c) interfacial layers.

Donor

In this work, three donor materials in combination with respective acceptors have been studied, their chemical structures are indicated in Figure 3.1. Poly[[4,8-bis[5-(2-ethylhexyl)-4-fluoro-2-thienyl]benzo[1,2-b:4,5-b']dithiophene-2,6-diyl]-2,5-thiophenediyl[5,7-bis(2-ethylhexyl)-4,8-dioxo-4H,8H-benzo[1,2-c:4,5-c']dithiophene-1,3-diyl]-2,5-thiophenediyl] (PM6) was purchased from 1-Material, poly[(2,5-bis(2-hexyldecyloxy)phenylene)-alt-(5,6-difluoro-4,7-di(thiophen-2-yl)benzo[c]- [1,2,5]thiadiazole)] (PPDT2FBT) was supplied by Han Young Woo in Department of Chemistry, College of Science, Korea University, and naphtho[1,2-c:5,6-c′]bis([1,2,5]-thiadiazole)-based polymer (NT812) was supplied by Fei Huang in Institute of Polymer Optoelectronic Materials and Devices, South China University of Technology.

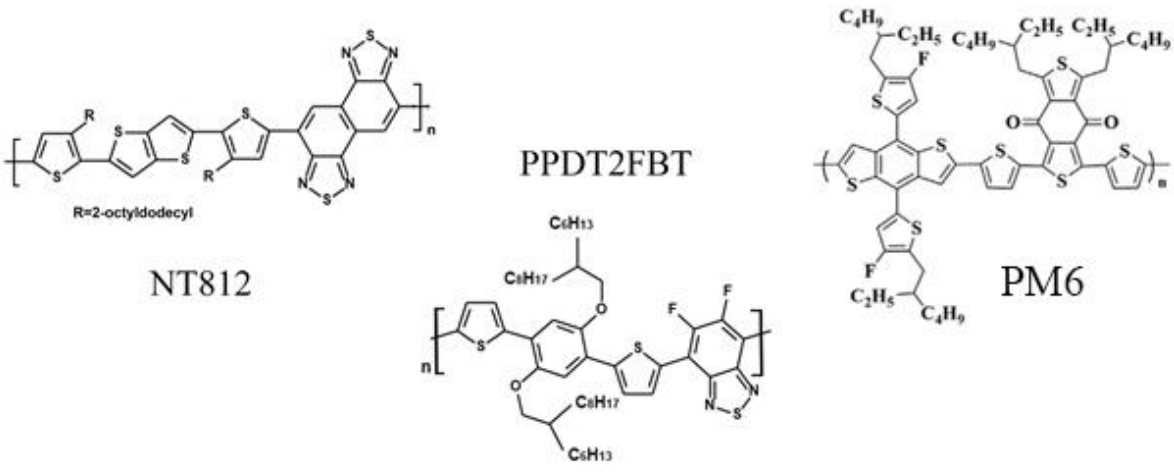

Figure 3.1. Chemical structure of donor materials used in this work.

Acceptor

Acceptor materials are strongly electronegative, compared to the respective donor, which facilities electron transfer from donor to acceptor. [6,6]-phenyl-C71butyric acid methyl ester (PCBM[71]) is one of the most famous fullerene acceptors which is widely using in the field of

organic solar cells (OSCs); however, its absorption spectrum shows a weak absorption in the visible region and no absorption in the near-infrared region (as shown in Figure 3.2d). To compensate for this disadvantage, non-fullerene acceptors have been introduced with many advantages such as facile synthesis, simplified purification, tunable optical and electronic properties, and improved solubility. Within this thesis, I focus on two types of non-fullerene acceptors named 3,9-bis(2-methylene-(3-(1,1-dicyanomethylene)-indanone))-5,5,11,11-tetrakis(4-hexylphenyl)-dithieno[2,3-d:2′,3′-d′]-sindaceno[1,2-b:5,6-b′]dithiophene (ITIC) was supplied by Fei Huang and (2,20-((2Z,20Z)-((12,13-bis(2-ethylhexyl)-3,9-diundecyl-12,13-dihydro-[1,2,5]thiadiazolo[3,4-e]thieno[2,"30':4',50]thieno[20,30:4,5]pyrrolo[3,2-g]thieno[20,30:4,5]thieno[3,2-b]indole-2,10-diyl)bis(methanylylidene))bis(5,6-difluoro-3-oxo-2,3-dihydro-1H-indene-2,1-diylidene))dimalononitrile) (Y6) was supplied by Yingping Zou in College of Chemistry and Chemical Engineering, Central South University of China. In chapter 4, the comparison of ITIC and PCBM[71] (purchased from Solenne) when they are blended with NT812, has been studied and in chapters 5 and 6, the combination of Y6 with PM6 has been analyzed.

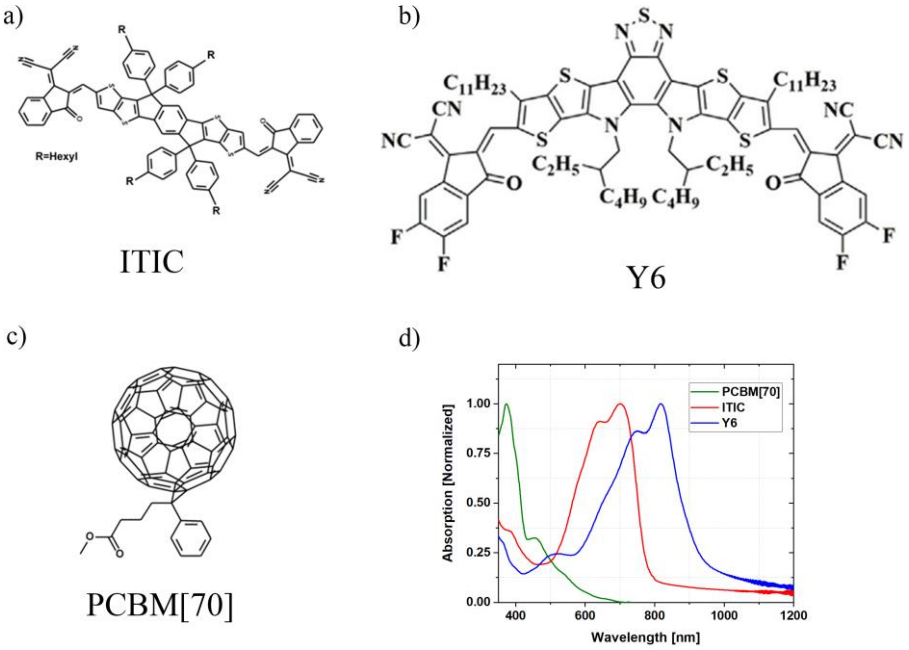

Figure 3.2. a,b, and c) Chemical structure of ITIC, Y6, and PCBM[70], respectively, and d) absorption spectrum of them.

Interfacial layer

Interfacial layers can act as electron/hole blocking or transport layers leading to either improving the efficiency by reducing the recombination and increasing the charge extraction or blocking electrons/holes in order to have a single diode behavior for space charge limited current (SCLC) purposes. Herein, I used different interfacial layers such as Poly(3,4-

ethylenedioxythiophene) polystyrene sulfonate (PEDOT:PSS) purchased from Heraeus Deutschland (Clevios P AI4083), 2,9-Bis[3-(dimethyloxidoamino)propyl]anthra[2,1,9-def:6,5,10-d'e'f']diisoquinoline-1,3,8,10(2H,9H)-tetrone (PDINO) and Poly(9,9-bis(3'-(N,N-dimethyl)-N-ethylammoinium-propyl-2,7-fluorene)-alt-2,7-(9,9-dioctylfluorene))dibromide (PFN-Br) purchased from 1-Material, ZnO nanoparticles purchased from Avantama (N-10) and MoO_3 purchased from Sigma-Aldrich.

The solvents: chloroform, chlorobenzene, 1,2-Dichlorobenzene, methanol, the solvent additives: 1-Chloronaphthalene (CN) and diphenyl ether (DPE), and the electrodes: silver (Ag), gold (Au), and aluminum (Al) were all purchased from Sigma-Aldrich.

3.2 Device Preparation

In the framework of this thesis, all devices are designed as shown in Figure 3.3a, with an active layer in the form of bulk heterojunction (BHJ). Indium tin oxide (ITO) glass substrates with sheet resistance 15 Ω/sq were purchased from PsiOTec, Lumtec, and Automatic research. Figure 3.3b illustrates two types of device structures with different pixel sizes so that $6mm^2$ (device Ⅰ) is used for steady state characterization and $1.1mm^2$ (device Ⅱ) is used for the transient electronic experiment, where a low RC-time is required; therefore, the sheet resistance and the pixel size have to be as small as possible.

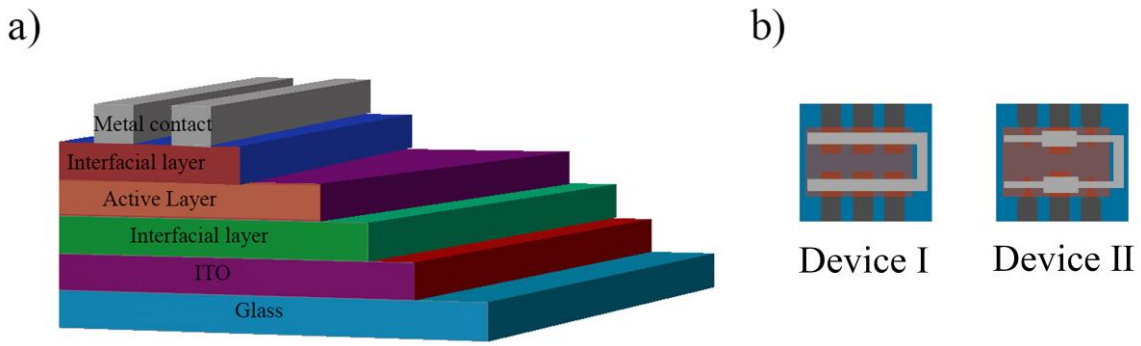

Figure 3.3. a) The device architecture of an OSC. b) Two types of a device structure for steady state characterization (device Ⅰ) and transient measurements (device Ⅱ). The active layer (light red) is sandwiched between the ITO substrate (purple) and the metal contact (light gray) evaporated by different shadow masks. The cross section of the ITO and top metal contact makes a pixel which is variable by changing the ITO pattern and top metal contact area, device Ⅰ includes $6mm^2$ pixel sizes and device Ⅱ includes $1.1mm^2$ and $16mm^2$ pixel sizes.

For device fabrication, at first, all substrates are mechanically cleaned in soap water and then they are cleaned in the ultrasonic bath with Hellmanex, deionized water, acetone, and

isopropanol for 20 min, followed by drying under nitrogen gas immediately after bringing out from the ultrasonic bath. The cleaned substrates were treated by oxygen plasma in 4 minutes at 200 W. Depending on the device architecture, either PEDOT:PSS (for solar cells and single diodes) or ZnO nanoparticles (just for single diodes) was spin coated on top of ITO substrates and then they are annealed on the hotplate at 150°C for 20 min in order to remove any remaining water present in PEDOT:PSS, or form the ZnO crystals. Afterward, substrates are transferred by a perfectly sealed transfer box into the glovebox (which is under nitrogen condition, O_2 << 1 ppm and H_2O << 1 ppm) in order to spin coat the active layer from its solution. The specific details of preparing the active layer solutions are given in chapters 4-7. Then the next layer which is the interfacial layer respect to the device architecture was spin coated from its solution. Finally, the substrates were transferred into the evaporator glovebox. The metal contact (which is Ag, Au, or Al depending on the device structure) was thermally evaporated on the top of the interfacial layer with a shadow mask (to make a specific pixel size) under high vacuum condition (1×10^{-7} mbar).

3.3 Absorption Measurement

In order to study the absorption of the blend of Donor:Acceptor or pristine Donor/Acceptor, a glass substrate (purchased from Thermo scientific) was cleaned as mentioned above, and then the active layer solution was spin coated on top of it, in the glovebox under nitrogen condition. After that, these films were encapsulated by a blue fix glue (purchased from BLUFIXX GmbH). Finally, the absorption spectrum of the films was measured by a Varian Cary 500 UVVIS-NIR spectrometer.

3.4 Current Density-Voltage Characterization

One of the most widely used techniques for analyzing solar cells is steady state current density-voltage (*J-V*) measurement. In this technique, the device is kept under standardized illumination conditions, air mass 1.5 irradiation with an intensity of 100 mW cm^{-2} (in this work, a Xenon lamp (Oriel 91160, 300 W) calibrated by KG5 filtered silicon solar cell (certified by Fraunhofer ISE) was used) and then the current density through the device is measured as a function of applied voltage (which was by a Keithley 2400 digital source meter). My devices were connected to the Keithley from ITO sides and top contact with a home-built sample holder which has a temperature controller in order to have the room temperature condition for the devices.

3.4.1 Temperature-Dependent Space Charge Limited Current

For temperature-dependent space charge limited current (SCLC) measurements, the fabricated single diodes are mounted into a portable nitrogen cryostat (Purchased from Janis research company INC, Model VPF-100) in the glovebox under nitrogen condition. Then the cryostat was sealed and took out from the glovebox and connected to a portable Turbo pump (EWARDS, T-Station 85) which was pumped down to 1×10^{-8} mbar. This portable nitrogen cryostat with high vacuum condition allows us to cool the temperature down to 70K. At the end, the *J-V* was measured by Keithley 2400 in a 2-wire source configuration under dark condition at different temperatures which was controlled by a temperature controller (Lake Shore, Model 335), connected to the cryostat.

3.5 Photoluminescence and Electroluminescence Measurements

In steady state photoluminescence (PL) measurement, the films were illuminated by a continuous-wave (CW) laser diode (purchased from https://www.insaneware.de/epages/61714203.sf/de_DE/?ObjectPath=Categories) excited state. However, in electroluminescence (EL) measurement, the charges were injected into the devices by a voltage-current source (Keithley 2400). Then, the emission spectrum was detected in a steady state condition by an Andor SR393i-B spectrometer equipped with a silicon (Si) (DU420ABR-DD) and an indium-gallium arsenide (InGaAs) (DU491A-1.7) detectors. In PL measurement, the PL emission of pristine and blend films were compared in order to find photoluminescence quenching (PLQ) which shows in the blend, how much exciton diffusion takes place from donor (acceptor) to acceptor (donor) interface, if the donor (acceptor) is excited.

$$PLQ = 1 - \left(\frac{PL_{blend}}{PL_{pristine}} \times \frac{1-10^{-Absorbance\ of\ pristine}}{1-10^{-Absorbance\ of\ blend}}\right) \tag{3.35}$$

3.5.1 External Quantum Efficiency of the Electroluminescence

The ratio of the number of emitted photons over the number of injected charges into the device is called electroluminescence external quantum efficiency (EQE_{EL}) which shows how many injected electrons recombine radiatively. The number of injected charges can be calculated from the applied current by Keithley 2400; however, to obtain the absolute number of emitted photons, the emission spectra needs to be integrated in all directions. First, the EL spectrum was measured by Andor SR393i-B spectrometer and it is normalized. Then, the OSC is assumed as a Lambert's emitter (see Appendix B for more details) and the absolute photon flux from the cells was measured by a calibrated silicon photodiode for the same injection conditions. In order

to make this assumption close to reality, in this measurement, the small pixel size has been chosen (6mm^2 is the best choice).

3.6 Photovoltaic External Quantum Efficiency Measurement

The incident photons to converted electron efficiency (IPCE) or photovoltaic external quantum efficiency (EQE_{PV}) is an important analysis in order to find how many electrons reach the outer circuit per incident photon as a function of the wavelength. In this work, the devices were monochromatically illuminated by a monochromator (LOT-Oriel) with a 200 W halogen lamp. Then, the output current of the devices was measured by a lock in amplifier (EG&G Princton Applied Research Model 5302). In front of the light source, an optical chopper was mounted as a reference frequency for the lock in amplifier. The light source was calibrated via a silicon photodiode (calibrated by Newport UV-818) and a germanium photodiode (calibrated by Newport 818-IR) for the visible and near infrared part of the light spectrum, respectively.

3.7 Resistance Dependent Photovoltage Experiment

Resistance dependent photovoltage (RPV) is a transient photovoltage technique that can measure both electron and hole mobilities simultaneously in operational devices. In this measurement, the device was illuminated by a short laser pulse (Q-switched Nd:YAG laser (NT242, EKSPLA) with 6 ns pulse duration and a typical repetition rate of 500 Hz which is changeable). A low light intensity is applied so that the electric field inside the device is undisturbed. The device was connected to a resistor box such that the photosignal is measured by an oscilloscope (Agilent DSO9104H) parallel, as shown in Figure 3.4. The measurement was repeated at many different load resistances, from differential mode (small resistor) to integral mode (large resistor); in order, firstly, to visualize the transit times, and secondly, to reveal the slower carrier mobility by amplifying the slower carrier's conduction current. Finally, the transit times for the faster and the slower carriers (if they are imbalanced) were determined as shown in Figure 2.4 and the mobility is given by:

$$\mu = \frac{d^2}{t_{tr}.V_{Bi}} \tag{3.36}$$

where d, t_{tr} and V_{Bi} are the device thickness (which was measured by Dektak, Bruker model), transit time and built-in field, respectively.

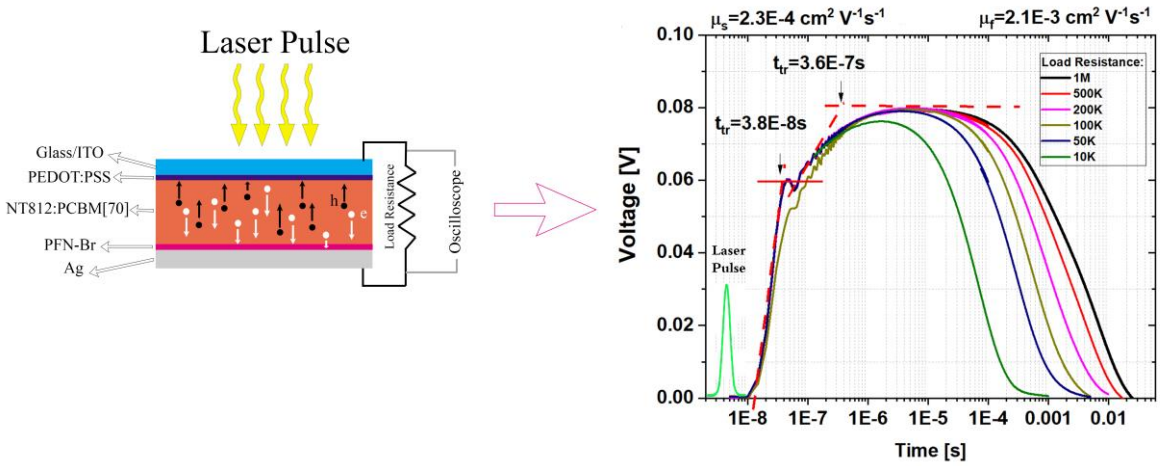

Figure 3.4. Sketch of an OSC (e.g. NT812:PCBM[70]), illuminated by a short laser pulse with 6 ns pulse width, which is connected to a load resistance, and the photovoltage is measured by the oscilloscope. The photogenerated charges start to move toward the electrodes; therefore, the photovoltage increases until the transit time when the charges reach the electrodes. In the case of distinct slow and fast carriers, two separate peaks and transit times will be observed corresponding to the faster and slower carriers. The first increase in the voltage corresponds to the faster carriers reaching the electrode, whilst the photovoltage increase due to the movement of the slower carriers saturates at longer transit time when the last slower charge carriers reach the respective electrode.

3.8 Bias Assisted Charge Extraction Experiment

Bias assisted charge extraction (BACE) measurement is the developed version of the charge extraction method, introduced by Duffy and coworkers[75], with high time resolution and strong extraction capability. In this measurement, the device was mounted in a home-built sample holder (designed by Andreas Pucher, Jona Kurpiers and Seyed Mehrdad Hosseini, includes five amplifiers and a high resolution relay, see section 3.8.1 for more details) and steady state illumination is applied by a CW-laser diode (purchased from insaneware). In order to find saturated photocurrent (J_{sat}) and open circuit voltage (V_{OC}) under each illumination condition, a variable reverse bias voltage was applied (by Keithley 2400) into the device until the photocurrent (the current under dark condition is subtracted from the current under light condition) is saturated (recorded by the LabView code), and then the voltage from the Keithley 2400 is opened under zero current condition to find the V_{OC}. After that, the high frequency relay (Panasonic ARA200A05, 1GHz) is switched off and the device is connected to the amplifiers. Now the DC mode of the laser changes to the pulse mode with pulse duration of 2 ms. The input voltage of the laser is amplified by another home-built amplifier in order to get a very fast falling/raising time (~15 ns) for switching off/on. During the illumination a pre-bias voltage,

which is V_{OC} at the same illumination condition, was applied through the device; consequently, the output current would be zero because the charge generation and charge recombination rate are equal at this condition. Then the illumination was turned off and also the pre-bias voltage was changed into a reverse (collection) bias voltage in order to extract all charges from the device before recombining (see Figure 3.5). Then the bimolecular recombination coefficient k_2 (if we assume that it's the dominant recombination process) would be calculated by this equation:

$$R = G = \frac{J_G}{e.d} = k_2.n^2 \qquad (3.37)$$

where R, G, J_G, e, d, and n are recombination rate, generation rate the generation current (which equals to the J_{sat} at the reverse bias voltage), the elementary charge, the thickness of the device, and the charge carrier density, respectively.

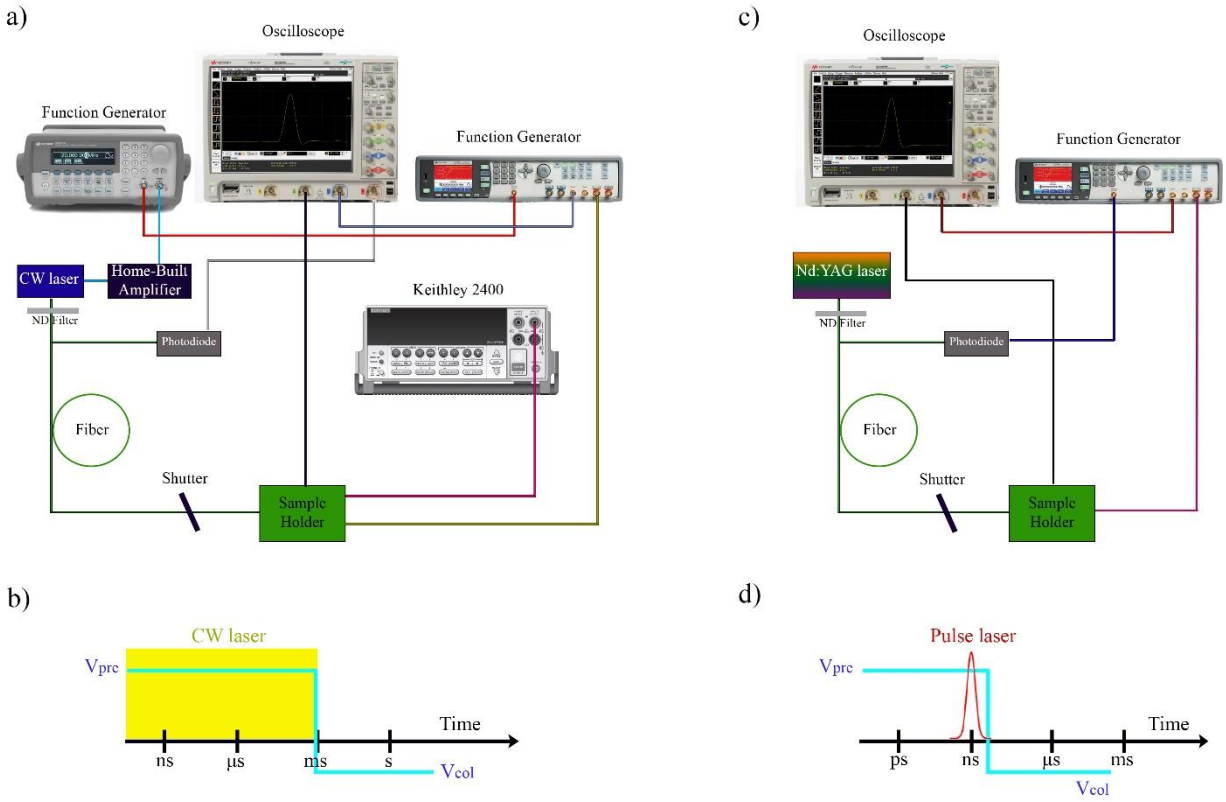

Figure 3.5. Instrument network and experimental time ranges for bias assisted charge extraction (a and b) and time delayed collection field (c and d).

3.8.1 Home-Built Amplifier

Extraction of all charges from the device needs a very fast voltage switching from pre-bias voltage to reverse (collection) bias voltage in order to distinguish between free charges being generated and their recombination; therefore, a home-built amplifier[76] was used. This home-built amplifier includes four fast current feedback operational amplifiers (purchased from Texas

instruments, THS3091) are connected in parallel to amplify the input voltage of the function generator by a factor of four which allows us to generate the signal with a fast rise time and low overshoot. After applying the voltage, the output current of the device should be measured, however, the current is very low and the signal needs to be amplified to get high resolution. Therefore, a differential amplifier (purchased from Texas instruments, THS3091) is used, connected in parallel to the grounded 10Ω (also 5Ω or 1Ω are possible) resistor, and then the photocurrent was measured by the oscilloscope (Agilent DSO9104H). By integrating the photocurrent transients, charge carrier density either at pre-bias or collection bias was obtained.

3.9 Time Delayed Collection Field Experiment

In this work, time delay collection field (TDCF) measurement was used in order to study the charge generation dynamic in OSCs. This technique is over 30 years old and at first, was applied to inorganic solar cells[77]; however, later also used to study OSCs.[78–80] In this measurement, the device was illuminated by a short laser pulse (as the same as RPV measurement) while it's held at pre-bias voltage, applied by a fast and low jitter function generator (Agilent 81150A) which is directly triggered by a fast trigger diode (EOT-ET2030TTL). An optical delay line (85m long quartz fiber, LEONI) delays the light pulse, which was detected by the diode before the fiber, in order to make a perfect timing and a low jitter between the optical excitation and the applied voltages (see Figure 3.5). This delay time can be tuned by the function generator before applying the collection bias for two purposes: Ⅰ) charge generation and Ⅱ) charge recombination analysis's. If the delay time between the laser pulse (excitation) and collection bias (extraction) is the shortest (6 ns, limited by the pulse width), the generation of free carriers could be measured. In this case, the pre-bias voltage varies in order to study the dependence of charge carrier generation on the electric field. On the other hand, by increasing the delay time, the photogenerated charge carriers will be allowed to recombine before extraction; consequently, the recombination dynamic would be tracked.

3.10 Capacitance-Voltage Experiment

Electrochemical impedance spectroscopy (EIS) is a technique that utilizes an alternating current (AC) signal of small amplitude to perturb a system under investigation and measure its electrical response (current or voltage). Impedance is analogous to electrical resistance and is popularly described as the "total opposition of a device or a circuit to the flow of alternating current". In this technique a sinusoidal voltage signal $V(t) = V_0 \sin \omega t$ is applied to the device under test and the electric response is measured as

$$I(t) = I_0 \sin(\omega t + \varphi) \tag{3.38}$$

where V_0 and I_0 are voltage and current amplitudes, $\omega = 2\pi f$ is the angular frequency of the sinusoidal wave and φ is the phase shift, i.e. a delay between the input and output wave signals. In this case, impedance is determined as

$$Z = \frac{V(t)}{I(t)} = Z_0 \frac{\sin \omega t}{\sin(\omega t + \varphi)} \tag{3.39}$$

where $Z_0 = V_0/I_0$.

Since the capacitance of simple circuits can be readily obtained from the impedance data, most impedance tools can be used to perform capacitance measurements. One of such measurements which finds an application in the study of a wide range of semiconductor devices and structures is capacitance-voltage (C-V) profiling.

In this study, the dark CV measurements were performed using the Keysight E5061B Vector Network Analyzer with a frequency measurement range of 5 Hz to 500 MHz. Prior to the measurements, the tool was calibrated using the 85032E Type N calibration kit. This was followed by the tool compensation procedure using the "Open", "Short" and "50 Ohm" measurements at the device connection fixture.

3.11 Photo-Induced Absorption Experiment

In quasi-steady-state photo-induced absorption (PIA) measurements, the excitation light emitting from a continuous-wave laser diode (Spectral Products) was modulated by an optical chopper (Thorlabs MC2000B) at a frequency tunable in a range from 200 Hz to 10 kHz, and then focused on the devices. The excitation wavelength was set to 405 nm (3.06 eV), and the excitation fluence is monitored by a programmable attenuator. A tungsten halogen lamp was utilized as a source for the probe light. The lamp's white light was sent to a monochromator (Spectral Products DK240), and the monochromatic probe light then was directed to overlap spatially with the modulated excitation light on the sample's surface. The change in the transmitted probe light ΔT induced by the modulated photoexcitation was detected by using a Si or InGaAs photodiode (Thorlabs) and a lock-in amplifier (SR830) referenced at the modulation frequency of the excitation light. The ΔT signal was corrected by subtracting the background. The transmitted probe light T was measured by using another optical chopper to modulate the probe light, the same photodiodes, and the lock-in amplifier.

Chapter 4. Impact of Bimolecular Recombination on the Fill Factor of Fullerene and Nonfullerene-Based Solar Cells

In this chapter, we present a comparative study of bulk heterojunction solar cells composed of a recently introduced nappthothiadiazole-based polymer (NT812) as the electron donor and two different acceptor molecules, namely PCBM[70] and ITIC. A comparison between the photovoltaic performance of these two types of solar cells reveals that the open circuit voltage (V_{OC}) of NT812:ITIC based solar cell is larger but the fill factor (FF) is lower than that of NT812:PCBM[70] device. We find the key reason behind this reduced FF in the ITIC-based device to be faster non-geminate recombination relative to the NT812:PCBM[70] system.

The supplementary information of this paper can be accessed online at (https://pubs.acs.org/doi/abs/10.1021/acs.jpcc.8b11669).[81]

4.1 Introduction

Conventional organic solar cells (OSCs) consist of blends of electron donating materials and classical electron accepting fullerene-based molecules in the form bulk heterojunctions (BHJs). However, in the past few years, the focus in the development of OSCs has shifted to non-fullerene acceptors (NFAs); synthesizing and engineering systems with power conversion efficiencies (PCEs) of 13%.[82] While these materials achieve impressive short circuit current (J_{sc}) and/or large V_{OC}, the devices exhibit relatively modest FF. Indeed, even good organic solar cells exhibit considerably lower FFs ~0.7 than the best perovskite 0.8-0.85 and inorganic devices, ~0.87.[83] In particular, most of these high efficiency organic devices have active layers around 100 nm only. Increasing the thickness is beneficial for enhancing the light absorption and, favourable for high-throughput solution processing techniques at lower cost and less defect density.[84] However, when the active layer thickness is increased, the FF and, with that, the overall PCE are reduced significantly for the majority of polymer/fullerene or non-fullerene combinations. Reduced FF can be imagined as the manifestation of voltage dependent charge photogeneration and inefficient free charge extraction in competition with non-geminate recombination.[85,86] Several reports have indicated that the geminate recombination of initially generated charge pairs at the donor/acceptor interface can be a significant loss pathway limiting the photocurrent generation, in particular, for those with highly intermixed donor−acceptor blends.[80,87,88] In other disordered systems, various reports showed that photocurrent at short circuit current is limited by non-geminate recombination.[89–91] However, there are significant

variations in the literature over the factors limiting the FF of organic photovoltaics (OPV) devices including selectivity of the contacts.[92,93]

Recently a novel Naphtho[1,2-c:5,6-c′]Bis([1,2,5]Thiadiazole)-based polymer (NT812) has been introduced with power conversion efficiencies as high as 10% in junctions with thickness of several hundreds of nm – very exceptional results for OSCs.[94] In previous work we presented charge transport and recombination properties of NT812:PCBM[70] and found significantly suppressed bimolecular recombination in this system.[95] In this study, we employ both steady state and transient electro-optical measurements to disentangle geminate and non-geminate loss processes in NT812 when blended with PCBM[70] and ITIC devices (see scheme 4.1 and Figure S1 for chemical structure and energy levels). We investigate possible reasons for the lower FF in ITIC blends.

Indeed, a detailed study of charge carrier generation, recombination, and extraction reveals different properties for these two acceptor systems. Our results indicate that despite a 0.2 eV smaller LUMO-LUMO offset in the NT812:ITIC blend and the lower electron mobility, this system still generates as efficient photocurrent as NT812:PCBM[70] device, at short circuit current. However the photocurrent in ITIC blend degrades more with approaching V_{OC} in NT812:ITIC resulting in a lower FF compared to NT812:PCBM[70]. Whilst both systems exhibits field independent charge generation, the NT812:ITIC device unveils more non-geminate recombination.

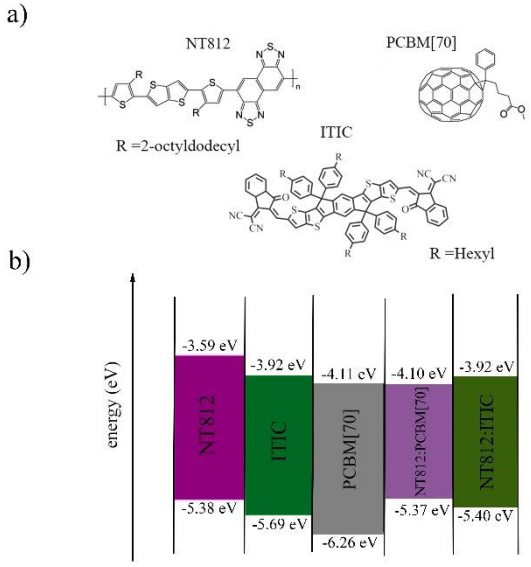

Scheme 4.1. a) Chemical structure of NT812, ITIC and PCBM[70], b) Photochemical energy level diagram for neat and blend films, obtained from CV measurements, see Figure S1.

4.2 Results and Discussion

Figure 4.1 shows current–voltage (*JV*) curves for 100 nm thick BHJ solar cells under simulated 1 sun illumination. The NT812:PCBM[70] device exhibits 8.0% PCE with an V_{OC} of 0.76 V, a J_{SC} of 14.3 mAcm^{-2} and a FF of 73%. The NT812:ITIC device exhibits a slightly higher J_{SC} and V_{OC} of 16.2 mAcm^{-2} and 0.81 V respectively, however a lower FF of 55%, which reduces the efficiency to 7.3%. Whilst the PCEs in 100 nm thick junction devices are not too different, the ITIC device exhibits a non-negligible gradient at short circuit, indicating that the observed J_{SC} and FF are reduced by loss mechanisms already effective at short circuit. As photon absorption is voltage-independent, this slope must be related to field dependent charge generation, or recombination/extraction.[52,96,97] We note that due to the small equilibrium charge carrier density in NT812:ITIC system any role of screening of built-in field due to the doping is negligible.[95] The smaller energy offsets in ITIC blend may be the cause of the slightly reduced exciton dissociation in this system (see Figure S2 for photoluminescence quenching data (PLQ)), however based on literature on other systems[98] the data still suggests efficient dissociation of the exciton at the NT812:ITIC interface within the amorphous regions whilst pure polymer and or ITIC domains also co-exists (hence the lower PLQ). In the following, the differences in geminate and non-geminate recombination dynamics are presented in order to investigate the origin of the dramatic change in the FF.

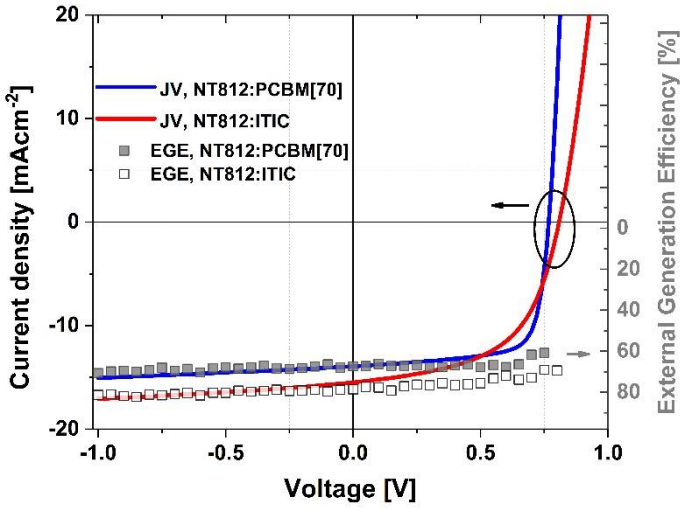

Figure 4.1. The external generation efficiency (EGE) which is mainly representative of geminate recombination for NT812:PCBM[70] and NT812:ITIC, measured with TDCF, as a function of pre-bias for 4ns delay time and fluences of ~0.02 μJ cm^{-2} at excitation wavelength of 532 nm with a laser pulse length of 6 ns. For comparison, the current density versus voltage

(JV) characteristics of the same device under simulated AM 1.5 G light calibrated to 100 mW cm^{-2} is shown by a solid line.

Charge transport properties

To investigate charge transport properties of BHJ solar cells, electron and hole mobilities (μ_e and μ_h) and equilibrium charge carrier concentration need to be quantified. We performed resistance dependent photovoltage (RPV) and space charge limited current (SCLC) measurements (see Figure S3) to determine the carrier mobilities.[99]

RPV setup is similar to time-of-flight, where charge carriers are photogenerated by a short low intensity laser pulse (such that the electric field inside the device is undisturbed. Unique to the RPV, the entire measurement is repeated at many different load resistances. The transient photosignal is determined by the competition between the transport of charge carriers inside the film, and the response of the external RC circuit. Typical data is shown in Figure S3; results are tabulated in Table 4.1.

In the ITIC system, using RPV we determine balanced carrier mobilities of ~1.4×10^{-4} cm^2 V^{-1} s^{-1}. This balanced mobility is confirmed through the SCLC measurements where the electron and hole mobilities are extracted to be 4.5×10^{-4} and 3.7×10^{-4} cm^2 V^{-1} s^{-1}, respectively. The electron mobility in the blend with ITIC is about an order of magnitude lower than typical PCBM[70] electron mobility in efficient blends with sufficient fullerene loading.[100,101] We had previously measured hole and electron mobilities of 4×10^{-4} and 2×10^{-3} cm^2 V^{-1} s^{-1} respectively, in NT812:PCBM[70] devices.[95]

There are differing views on the importance of mobility balance from the theoretical perspective; most simulations have predicted photogeneration to suffer strongly from imbalanced mobilities.[102] In addition, the preferential extraction of only one carrier type is well-known to cause space charge of the slower species to build up.[101,103] The creation of space charge suppresses the overall charge carrier collection efficiency due to the screening of the built-in electric field – this is especially the case in the thick junction but has been argued to play a detrimental role in thin solar cells (~100 nm).[101] In this regard, it is anticipated that the ITIC blend takes advantage of its balanced mobilities. However, it is a general consensus that low mobilities are detrimental to charge generation and extraction,[100] which in part may be the cause of the lower FF in ITIC devices.

Table 4.1. electron and hole mobilities of NT812:ITIC device based on two type of measurements, SCLC and RPV.

Measurement	Electron mobility ($cm^2\ V^{-1}\ s^{-1}$)	Hole mobility ($cm^2\ V^{-1}\ s^{-1}$)
SCLC	4.5×10^{-4}	3.7×10^{-4}
RPV	1.4×10^{-4}	1.4×10^{-4}

Charge generation

To understand the poorer FF in NT812:ITIC blends, charge generation and recombination were studied in detail with a combination of different steady-state and transient methods. A poor FF may originate from a field dependent dissociation of CT states into free carriers, and /or significant bimolecular recombination of the free carriers. The former is mostly dependent on the driving force to dissociate CT states to free charges and the latter is a typical characteristic of low mobility disordered systems.

We employed time-delayed collection field (TDCF) measurements to elucidate on the nature of charge generation and recombination as described in previous work.[79] In TDCF measurements, the device is held at a particular pre-bias while excitons are photogenerated with a laser pulse. At that certain bias, any geminate and non-geminate recombination may occur, and after a specified delay time, a reverse bias is applied to collect all extractable charges that have survived geminate and non-geminate recombination. When these experiments are conducted under very low fluences and at short delay times, non-geminate recombination is minimized during charge carrier extraction and thus the total extracted charge per photons absorbed is representative of the external generation efficiency (EGE). The EGE can be obtained as a function of voltage. At longer delay times and higher fluences, TDCF can yield information about non-geminate recombination of free carriers.

Figure 4.1 shows the JV curves of NT812:ITIC and NT812:PCBM[70] devices along with the EGE as a function of voltage (total charge plotted versus the pre-bias voltage at a delay time, t_d=4 ns at very low fluence (~0.02 μJcm^{-2})). The *JV* curves are well described by our EGE at V < 0.25 V for NT812:PCBM[70] and V < 0 V for NT812:ITIC. This means that the device photocurrent is generated exactly with the charges measured by TDCF at short delay times. It is also evident that in PCBM[70] devices there is no effect of pre-bias on generation, while the

ITIC exhibits about 3% loss from -1 V to J_{SC}, which is insignificant; previous reports have demonstrated systems with much higher field dependent charge generation.[104]

This finding suggests that free charge photogeneration in both ITIC and PCBM[70] systems proceeds in a fashion where there is a low barrier for charge transfer state dissociation into free carriers. This may be either due to entropy,[28] and / or high local mobility.[30]

In ITIC and PCBM[70] blends, based on high photoluminescence quenching yields and high photocurrent densities, we anticipate the co-existence of both mixed and pure domains, whereby an energetic sink is established that drives and stabilizes the photogenerated charges out of the intermixed regions.[98] The rather weak or even absent field dependence of generation seen in ITIC and PCBM[70] is consistent with this structural picture.

Non-geminate recombination

Non-geminate recombination occurs as free charges travel through the film and encounter the opposite charge at the interface between donor and acceptor bulk heterojunction to form a CT state. This CT state may decay to the ground state and effectively an electron and a hole are recombined non-geminately to the ground state. The simplest description of charge carrier recombination is Langevin's model in which encounter rate is consider as $k_L = q(\mu_h + \mu_e)/\varepsilon_r\varepsilon_0$ where q is elementary charge; ε_r and ε_0 are relative and vacuum permittivity, respectively; μ_e and μ_h are electron and hole mobilities. In this model, the encounter rate of electrons and holes is determined with the sum of electron and hole mobilities. A more realistic modification of the encounter rate, k_{en} which is relevant to BHJ systems with nano-domains has been presented by Heiber et al.[61] given by Equation 4.40.

$$k_{\mathrm{en}} = \left(\mu_h^g + \mu_e^g\right)^{\frac{1}{g}} f(d)\ \frac{q}{\varepsilon_r\varepsilon_0} \equiv \gamma_{\mathrm{geo}} k_L \tag{4.40}$$

where g is a domain size dependent power mean exponent and $f(d)$ a morphological reduction prefactor due to the confinement of the carrier in their respective domains. γ_{geo} is the overall geometrical reduction factor of bimolecular recombination relative to the Langevin rate (sum of mobilities) explained in previous works.[63] However, often many systems typically show a significant departure from this type of recombination. As such the recombination of free carriers can be expressed by the rate equation

$$R = k_{\mathrm{rec}} n^2 = \gamma k_L n^2 \tag{4.41}$$

$$\gamma = \gamma_{\mathrm{CT}} \times \gamma_{\mathrm{geo}} \quad (4.42)$$

where k_{rec} is the recombination coefficient for bimolecular recombination, γ the overall bimolecular recombination reduction factor relative to Langevin rate (k_L) and γ_{CT} the reduction factor due to the efficient recycling the CT states in some systems (see below). Therefore, γ has to have two major components. γ_{geo} is the reduction factor due to the reduced encounter rate of charges at the interface, with respect to the Langevin rate. Heiber et al. have found that this reduction factor is not significant for domain sizes relevant to efficient solar cells.[61] The other component that reduces the recombination, γ_{CT}, is related to the kinetics of the charge transfer states. When the dissociation rate of the free carriers is much faster than the decay rate of the singlet CT states to the ground and back electron transfer rate of the triplet CT states to triplet excitons, this effectively results in suppressed recombination rate of free charges to the ground state.[105]

We employed steady state bias assisted charge extraction (BACE) to probe the nature of recombination.[62] In BACE measurements, the device under steady state illumination is held at the pre-bias voltage which is exactly the VOC at the given illumination intensity. Under this condition, the recombination of free carriers is equal to the charge generation (G) so that

$$R = G = \frac{J_{sat}}{q.d} \quad (4.43)$$

where J_{sat} and d are the saturated current at reverse bias voltage and the thickness of the device, respectively. When the LED is turned off, the external bias is rapidly changed to the reverse bias in order to extract all carriers; hence, the recombination coefficient for bimolecular recombination (k_{rec}) is determined.

Our measurements indicate that k_{rec} measured for ITIC blend is 8×10^{-17} $\mathrm{m^3\ s^{-1}}$ at 1 sun, with dependence on charge-carrier density, as shown in Figure 4.2.

This recombination coefficient is rather high and it is only 5 times less than its Langevin recombination coefficient (k_{L}) for this system as shown by the dash line. NT812:PCBM[70] however exhibit much smaller k_{rec}, yielding 43 times reduced recombination than its Langevin recombination limit. In the SI we present a comparison between the measured data with that of the literature, on the competition factor between charge extraction and second-order bimolecular recombination as defined by Bartesaghi et al.[85] (see Figure S4). Previous report has suggested 800 times reduced recombination for NT812:PCBM[70],[95] however we note that

NT812 has a different molecular weight in this study and also yields lower efficiency compared to the previous work.

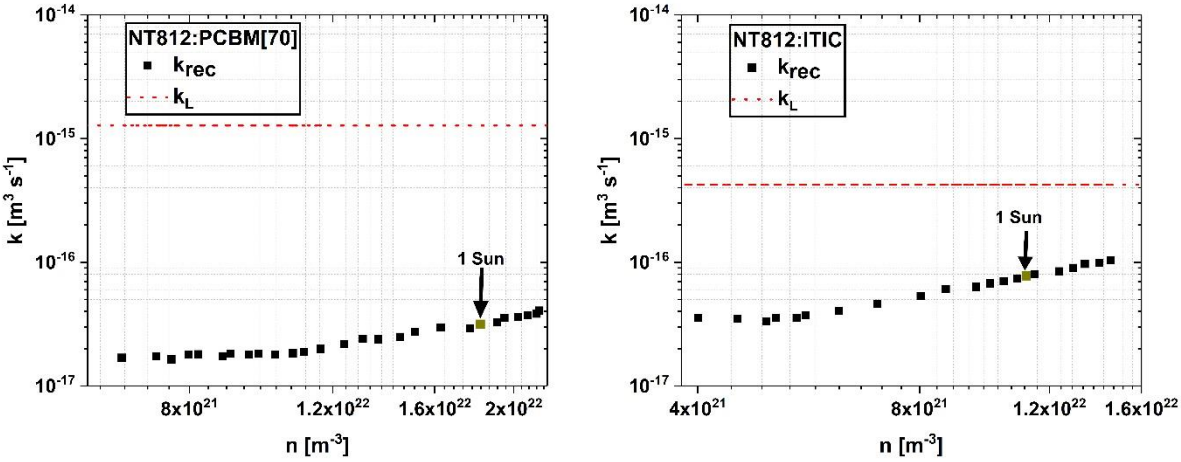

Figure 4.2. Bimolecular recombination coefficient as a function of carrier intensity, obtained from BACE measurement (solid squares) and Langevin recombination (dash line) for NT812:PCBM[70] and NT812:ITIC.

Concerning charge recombination, from pre-bias dependent TDCF measurements at different delay times between excitation and extraction, we observe that whilst both devices exhibit a dependence of extraction on pre-bias, the PCBM device however, shows an almost invariant behaviour with the delay time, whilst the ITIC system shows a strong dependence of extracted carriers on the delay time. One can see that in the range of -1 V to V_{OC}, in the ITIC system almost 50% of charges have survived from recombination at 200 ns compared to 80% at 20 ns. In PCBM however, 80% of charges survive recombination at 200 ns, compared to 85% at 20 ns. Of particular interest is that in the PCBM system, loss in extraction due to the delay time, independent of fluence, only occurs at around 50 mV below its V_{OC}, whilst the ITIC system shows loss of extraction from an early pre-bias of -0.5 V. These results illustrate important findings. First, a slightly stronger field dependence is present in the ITIC system. Secondly, this field dependence of the extracted charges is strongly dependent on the delay time in NT812:ITIC device, suggesting a fast non-geminate recombination. In the PCBM system, however, the recombination is strikingly very slow and almost invariant in time. Consequently, the TDCF results at a delay of 4 ns suggest that in fact, whilst generation of free charge carriers occurs equally efficient up to J_{SC} for both systems (Figure 4.1) the rate of recombination of these photogenerated charges differs significantly (Figure 4.3). The importance of these findings are reflected when considering the superposition principle. Superposition principle is

often used to describe the total *JV* characteristics of solar cells in which the current flowing in illuminated devices at a bias voltage *V* is the shift of a voltage-independent saturated photocurrent and the dark current – explained by the Shockley diode equation. The *JV* curve of the NT812:ITIC device under illumination cannot to be reconstructed from the dark *JV* as shown in Figure 4.4, and reflects the invalidity of the superposition approximation for this (and most organic semiconductor) systems when the photocurrent is assumed voltage independent. NT812:PCBM on the other hand, shows that the shifted dark current does reproduce the *JV* curve under illumination reasonably well.

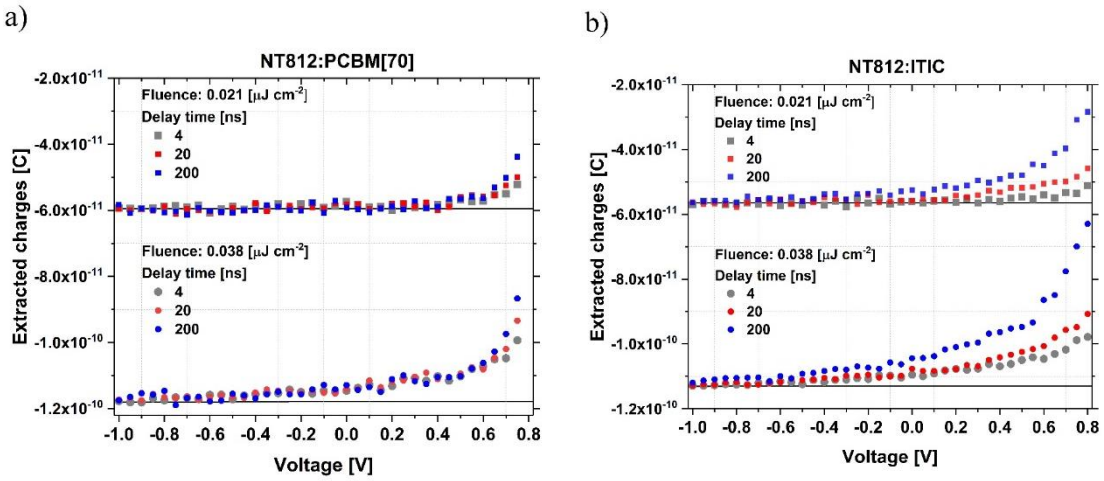

Figure 4.3. Extracted charges versus pre-bias voltage at different delay times between the pre-bias and the collection voltage for a) NT812:PCBM[70] and b) NT812:ITIC devices at two laser intensities.

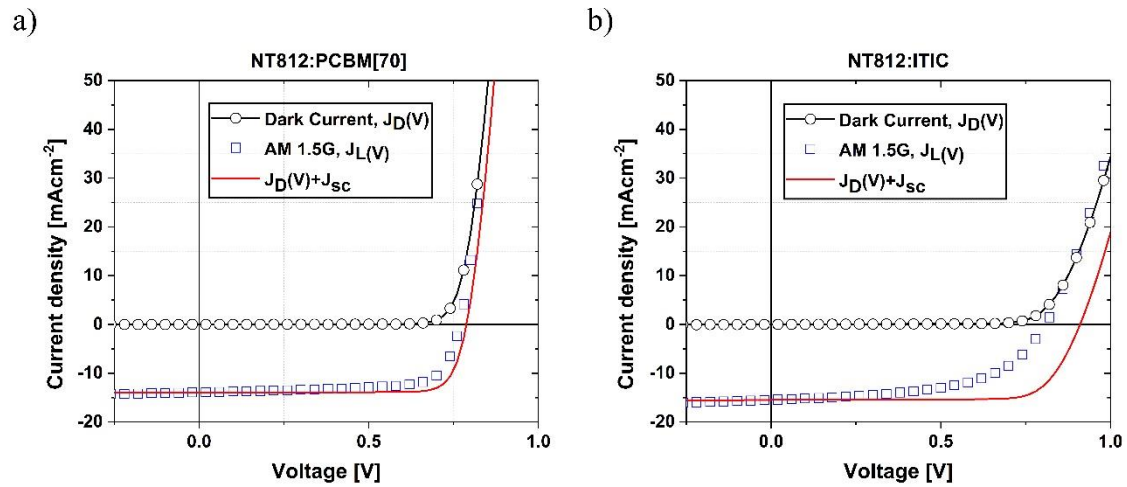

Figure 4.4. JV characteristics of a) NT812:PCBM[70] and b) NT812:ITIC under simulated AM 1.5G light calibrated to 100mW cm^{-2}. The circle with black line and blue squares shows dark and light current, respectively. Shifted dark by J_{sc} is shown with red solid line.

The study herein addresses the factors determining the fill factor of blend devices employing NT812 with ITIC and with PCBM[70]. Overall, we find that the variation in FF between these two acceptors is not primarily determined by variations in light absorption, nor by variations in exciton separation efficiency. Rather this variation is determined by differences in charge recombination affecting charge collection efficiency.

Among the many studies of organic solar cells employing NFAs, most studies have focused rather on the importance of exciton separation and/or carrier mobility in limiting photocurrent generation. However, the consideration of CT state losses, with respect to Langevin recombination in limiting bimolecular recombination has been completely absent from the NFA literature to date.

In Figure 4.5 we have plotted the predicted diffusion limited reduction factors (γ_{geo}) for different domain sizes based on the model of Heiber et al.[29] [Equation (4.40)] versus the square root of the mobilities product assuming an electron mobility of 1.4 x 10^{-4} cm^2 V^{-1} s^{-1}. Plotting the measured reduction factor (γ) of the NT812:ITIC and NT812:PCBM[70] system on the same figure demonstrates that the ITIC reduction factor is only five times larger than the predicted encountered recombination whilst PCBM[70]'s reduction factor significantly departs from the model, regardless of the domain size or the nano-morphology. This implies that the origin of the fast recombination in the ITIC system and the non-Langevin recombination in the PCBM[70] device is predominantly controlled by the kinetics of the CT state.

This raises the question of the importance of the charge transfer state (CTS). All recombination occurs through CT states. Whilst encounter limited recombination is indeed relevant for forming the intermediate CTS, the final loss mechanism is, however, limited by the back electron transfer of ^{3}CT to triplet excitons or geminate recombination of the ^{1}CT state to the ground state.[106] In NT812:PCBM[70], the suppressed recombination is assigned to the slower loss decay and back electron transfer rate of the CT states compared to their dissociation rate which results in equilibrium between the CTS and free charges.[95] We note that this kinetic completion is very sensitive to the active layer's morphology and even for the same material system, one can observe different kinetics by changing the processing conditions or the molecular weight of the polymer. In contrast, in case of the ITIC system, the recombination rate is mostly encounter limited.

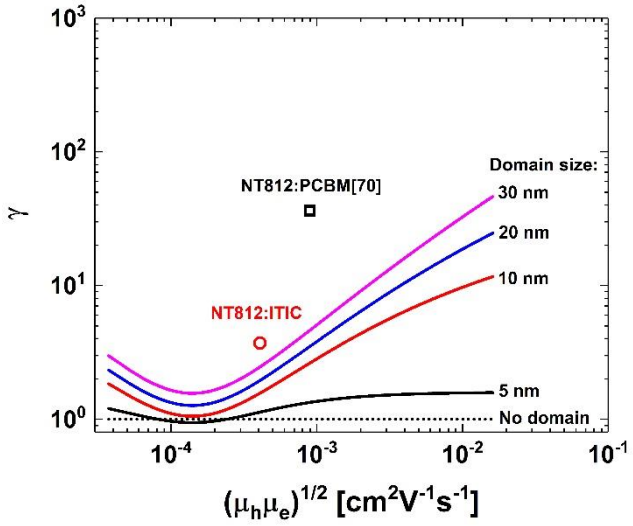

Figure 4.5. Predicted diffusion controlled reduction factors of the bimolecular recombination for different domain sizes (coloured lines, calculated based on Heiber et al.[61]) as a function of the square root of the mobilities assuming an electron mobility of 1.4 x 10^{-4} cm^2 V^{-1} s^{-1}, compared the measured reduction factor for NT812:ITIC and NT812:PCBM[70].

It is of interest that despite the smaller energy offsets and moderately lower photoluminescence quenching of the excitons in the ITIC system, the loss in CTS generation does not translate into a loss in EGE or photocurrent; rather similar EGE and photocurrent at J_{SC} are generated in this blend compared to the PCBM[70] blend. This is consistent with previous studies on comparison of charge generation between fullerene and non-fullerene blends, where it has been concluded that NFA blends show as efficient (if not better) charge generation.[107–110] However, in contrast to previously reported NFA, perylene diimides systems in particular, the increased non-geminate recombination in ITIC is not assigned to spatially trapped charge carriers in isolated domains, rather to faster recombination of the free carriers.

4.3 Experimental Section/Methods

Solar-Cell Fabrication and Characterization

Patterned indium tin oxide (ITO)-glass substrates were pre-cleaned successively with detergent, acetone, de-ionized (DI) water and IPA and dried by nitrogen. The dried substrates were treated by oxygen plasma at room temperature for 4 min and then coated with PEDOT:PSS by spin-coating (3000 r.p.m. for 30 s, thickness of ≈40 nm) and were then baked at 150 °C for 15 min in air. For deposition of active layers, blend solution of polymer (NT812 with polydispersity index, PDI≈ 2) and PCBM[70] at a weight ratio of 1:1.5 dissolved in CB:DCB = 3:1 (with 0.5

vol% of 1-chloronaphthalene) and blend solution of polymer:ITIC at a weight ratio of 1.3:1, based on optimum device efficiency (see Table S1 for different blend ratio), dissolved in o-xylene (with 1 vol% of 1-Methyl-2-pyrrolidinone) were spin-cast on top of the PEDOT:PSS layer in a nitrogen-filled glove box. The active-layer thickness was controlled by changing the concentration of the solution; typically an active layer of 100 nm thickness can be achieved by 4 and 9 mg mL^{-1} solution (based on polymer concentration) for NT812:PCBM[70] and NT812:ITIC, respectively. Thermal annealing of the blend films was carried out by placing them on a hot plate at 100 °C for 15 min and 160 °C for 20 min for NT812:PCBM[70] and NT812:ITIC, respectively, in a nitrogen atmosphere. A 5 nm PFN-Br layer was then spin-coated from methanol solution onto the active layers. The thin films were transferred into a vacuum evaporator connected to the glove box, and Ag (100 nm) was deposited sequentially through a shadow mask under $\approx 1 \times 10^{-7}$ mbar, with an active area of the cells of A = 0.011 cm^2 for BACE and TDCF measurement, and A = 0.06 cm^2 for JV measurement.

UV-Visible absorption and Photoluminescence (PL) spectroscopy

UV-Visible spectra of the thin films were acquired with Cary 5000 UV-Vis-NIR spectrophotometer in air. The PL spectra were measured with a Fluorolog-3 spectrofluorometer (Horiba Jobin Yvon). All film samples were spin coated on glass substrates.

Time Delayed Collection Field

In the TDCF experiment, a laser pulse from a diode pumped, Q-switched Nd:YAG laser (NT242, EKSPLA) with 6 ns pulse duration and a typical repetition rate of 500 Hz working at 532 nm were used to generate charges in the device. A pulse generator (Agilent 81150A) was used to apply the pre- and collection bias which are amplified by a home-built amplifier. The current through the device was measured via a grounded 10 Ω resistor in series with the sample and with a differential current probe recorded with an oscilloscope (DSO9104H). The pulse generator was triggered with a fast photodiode (EOT, ET-2030TTL). The fluence was determined with a CCD-camera in combination with a calibrated photodiode sensor (Ophir) and a laser-cut high-precision shadow mask to define the illuminated area.

Bias Assisted Charge Extraction

The experimental setup required for BACE measurements was similar to the TDCF setup, except for the illumination conditions. The steady state condition was established by a high power 1 W, 638 nm laser diode (insaneware) with a switch off time of about 10 ns. The LED was operated at 500 Hz with a duty cycle of at least 50% of one period, which means 1ms of

illumination before the diode was switched off for 1 ms. After switching off the laser diode, a high reverse bias was applied and all charges were extracted. The fast switch off time of the diode and the fast pulse generator (Agilent 81150A) allowed for charge extraction as fast as 10–20 ns after the switch off. The current transients were measured via a grounded 10 Ω resistor and recorded with an oscilloscope (DSO9104H) in the same way as for the TDCF measurement.

Resistance dependent Photo Voltage

Photocurrent and photovoltage transients were recorded using a digital storage oscilloscope (DSO9104H) via a LabVIEW code. A pulsed second-harmonic Nd:YAG laser (NT242, EKSPLA) working at 450 nm was used with 6 ns pulse duration. The laser beam with ~50 mJ energy output was attenuated with a natural optical-density (OD) filter set. Low laser pulse fluences (~OD 7) were used for the RPV mobility measurements in order to prevent a redistribution (screening) of the internal electric field and maintaining quasi-short-circuit conditions regardless of the load resistance.

4.4 Conclusion

In summary, we compare device performance between ITIC and PCBM when blended with NT812 polymer. The ITIC system demonstrates a blend with balance carrier mobilities, and a high V_{OC} and J_{SC} whilst exhibiting a FF that is affected by field dependent mechanisms. We show that the field dependence limiting the FF stems from fast time-dependent non-geminate recombination. On the other hand, the PCBM system exhibits strikingly slow non-geminate recombination and reduced recombination. Slowing down the non-geminate recombination, to shift the balance towards non-Langevin systems, is important for both improving the power conversion efficiency and also for achieving thick junction devices.

Chapter 5. Putting Order into PM6:Y6 Solar Cells to Reduce the Langevin Recombination in 400 nm Thick Junction

In this chapter, we demonstrate that by regulating the packing and the crystallinity of the donor and the acceptor, through volumetric content of chloronaphthalene (CN) as a solvent additive, one can improve the FF of thick PM6:Y6 device (~400nm) from 58% to 68% (PCE enhances from 12.2% to 14.4%). Our data indicates that the origin of this enhancement is the reduction of the structural and energetic disorders in the thick device with 1.5%CN compared with 0.5%CN. This correlates with improved electron and hole mobilities (by 1.4 and 3.6 times, respectively) and a 50% suppressed bimolecular recombination, such that the non-Langevin reduction factor is 180 times. This work reveals the role of disorder on the charge extraction and bimolecular recombination of NFA based OSCs. The supplementary information of this paper can be accessed online at (https://onlinelibrary.wiley.com/doi/full/10.1002/solr.202000498).[111]

5.1 Introduction

In the last decade, organic solar cells (OSC) have experienced an important transformation. While much of the efficiency improvements were driven through judicious design of donor polymers, it is the engineering of the non-fullerene acceptors (NFA) through Y-series which have contributed to certified power conversion efficiencies (PCE) that rose to 15% in 2019 (or 18% in 2020).[11,12] However, the fill factor (FF) of these devices still lacks well behind the prediction of the Shockley-Queisser theory for the given open-circuit voltage (V_{OC}) values. Thus, further success in OSC can be achieved through improvements in FF in both thin and thick junctions; in particular, increasing the thickness of the device allows for commercialization of the technology. However, at present the active layer thickness of the optimum performance is limited to around 100 nm. Typically, OSCs thicker than 100 nm mostly suffer from reduced FFs with only a handful of exceptions.[63,81,95,112–114] Whilst it is now well-established that for the NFA systems charge generation is very efficient,[31,115–118] the loss in FF is primarily dictated by a competition between charge carrier extraction and non-geminate recombination.

Despite the advantages and prior success of solution-processed organic semiconductors, charge transport properties are not an inherent strength: the comparatively low chemical purity and the presence of structural and energetic disorder tend to limit their charge transport properties.

Charge transport in organic semiconductors has traditionally been thought to be limited to a low-mobility regime by pronounced energetic disorder. The consequence of the low mobilities is the higher probability of encountering between the free carriers (as opposed to extraction) which proceed via a second order process, described by the bimolecular recombination coefficient k_2. Recombination of free charge carriers in such semiconductors is common to be described by the Langevin theory:

$$k_L = (\mu_h + \mu_e)\frac{q}{\varepsilon_r \varepsilon_0} \quad (5.44)$$

where k_L is the Langevin recombination constant, q is the elementary charge; ε_r and ε_0 are the relative and vacuum permittivities, and μ_e and μ_h are the electron and hole mobilities, respectively.

Given the fact that k_L is proportional to the mean carrier mobility which needs to be maximized, a particular challenge lies in understanding why and to what extent recombination can be reduced relative to the Langevin limit. There is growing consensus that the encounter of charge carriers at the donor-acceptor interface goes along with the reformation of interfacial charge transfer (CT) states and that the main process behind suppressed recombination is the re-dissociation of such CT states.[105,119] In this picture, k_2 is written in terms of three factors: $k_2 = \gamma_{CT}\gamma_{en}k_L = \gamma k_L$. Here, $\gamma_{\mathrm{en}} = k_{\mathrm{en}}/k_L$ describes the reduction of encounter rate compared to the Langevin model due to phase separation, and $\gamma_{CT} = 1 - P$, is the CT recombination reduction factor, with P being the probability of (re-)dissociation of the formed CT states. As an important consequence, strongly suppressed recombination would be limited to systems with efficient (field-independent) CT dissociation. Recently, Kassal and co-workers[28] have shown that from the thermodynamic perspective energetic disorder facilitates charge separation. However, this effect is concomitant with reduced mobility and charge extraction.[120–122] In addition to disorder, other explanations for efficient charge generation have been proposed.[100,123] In 2019 we showed that free charge generation in the state of the art PM6:Y6 device is essentially barrierless with near-unity efficiency, assisted by an electrostatic interfacial field (which for crystallized Y6 is large enough to compensate the Coulomb dissociation barrier).[31] However, surprisingly, despite barrierless CT dissociation ($P = 1$) the recombination coefficient ($k_2 = 1.7 \times 10^{-17}$ m^3 s^{-1}) was fairly large, corresponding to a suppression of only 6 relative to Langevin recombination, consistent with the loss of the FF with increasing thickness.[11]

Here, we investigate the effect of disorder caused by variations in the device fabrication conditions on the performance of blends of PM6 (poly[(2,6-(4,8-5is(5-(2-ethylhexyl-3-fleoro)thiophen-2-yl)-5enzo[1,2-5:4,5-5']dithiophene))-alt-(5,5-(1',3'-di-2-thienyl-5',7'-

5is(2-ethylhexyl) 5enzo[1',2'-c:4',5'-c']dithiophene-4,8-dione)] and Y6 (2,20-((2Z,20Z)-((12,13-bis(2-ethylhexyl)-3,9-diundecyl-12,13-dihydro-[1,2,5]thiadiazolo[3,4-e]thieno[2,"30':4',50] thieno[20,30:4,5]pyrrolo[3,2-g]thieno[20,30:4,5]thieno[3,2-b]indole-2,10-diyl)bis(methanylylidene))bis(5,6-difluoro-3-oxo-2,3-dihydro-1H-indene-2,1-diylidene))dimalononitrile) as a non-fullerene acceptor (NFA) (see the chemical structure in Scheme S1a). In this study, we demonstrate that the performance of PM6:Y6 is thickness dependent, predominantly due to enhanced crystallization of Y6 with increasing thickness. This, in turn, enhances the mobility of Y6, causing space charge limited effect (due to further imbalanced carrier mobilities) in the thick junctions; sacrificing the FF. Herein, we report on over-coming this limitation by tuning the volumetric content of the additive chloronaphthalene (CN) to enhance the crystallinity and packing of the donor in thick junctions, resulting in substantial improvement in FF. In order to elucidate the nature of this phenomenon, energetic disorder and carrier mobility, as well as the bimolecular recombination and morphology have been studied by utilizing temperature-dependent space charge limit current (SCLC), bias assisted charge extraction (BACE) techniques and grazing incident wide angle x-ray spectroscopy (GIWAXS). Our results show that once the amount of CN is increased from 0.5%Vol to 1.5%Vol in the thick device, the energetic disorder of electrons and holes is reduced by 2% and 6%, respectively; subsequently, the electron and hole mobilities are enhanced. Now, this raises the question: "does the extraction of charge carriers overcome the recombination or is the recombination slowed down?" Our data indicates that not only does the lower energetic disorder improves the carrier mobilities in the thick device with 1.5%CN compared with 0.5%CN, but also it suppresses bimolecular recombination so that the FF loss is reduced compared to the optimum junction. This achievement sheds new light on the role of energetic disorder on recombination mechanism of NFA based OSCs. The combination of these results frames a constructive guideline to mitigate bimolecular recombination towards the development of thick junction high efficiency solar cells.

5.2 Results and Discussion

Figure 5.1 shows the current density–voltage (*J*–*V*) curves for the 100 nm and 400 nm thick PM6:Y6 in the form of bulk heterojunction (BHJ) solar cells under simulated AM 1.5G illumination. Both devices have been fabricated in the conventional structure (Scheme S1b).The device with the optimum thickness of 100nm exhibits 15.9% PCE with a V_{OC} of 0.82V, a J_{SC} of 26.3mA cm^{-2}, and a FF of 73.4%. We note that the device V_{OC} and J_{SC} (0.81V and 25.5mA cm^{-2}, respectively) show only minor thickness dependence. We have recently assigned the reason behind the invariant J_{SC} to be due to the extraordinarily long diffusion

length of Y6.[124] On the other hand, the trend in V_{OC} is very typical[125] and is therefore not discussed further. However, upon increasing the junction thickness to 400 nm, the FF drops dramatically to 58.5%, reducing the PCE to 12.2%.

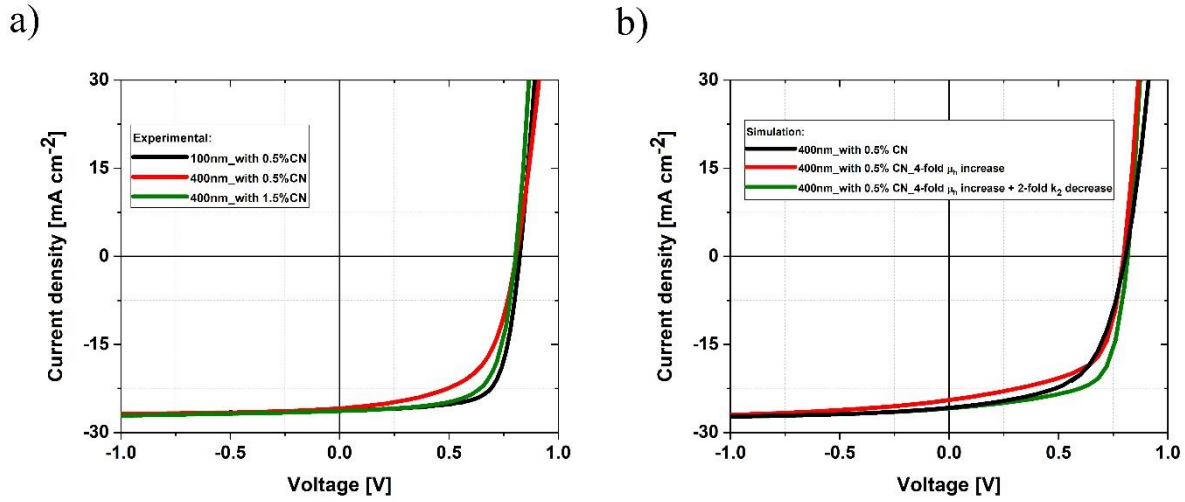

Figure 5.1. The current voltage (*J-V*) characteristics of PM6:Y6 solar cells: a) under simulated AM 1.5G light calibrated to 100 $mW\ cm^{-2}$ for different active layer thicknesses and solvent additive content, b) simulated device performance (AFORS-HET) for the 400nm thickness (with 0.5%CN) with different hole mobilities and bimolecular recombination coefficients.

As previously discussed in the literature, the drop in the FF can be understood in terms of increased bimolecular recombination losses[126,127] during charge transport or space charge effects either due to doping or imbalanced carrier mobilities.[128–131] The efficiency limitation that comes with lower FF in thick junction devices can be illustrated with numerical drift-diffusion (D-D) simulations. To this end we performed AFORS-HET simulations;[132] the simulation numerically solves the drift-diffusion equations that govern the *J–V* characteristics of the device, thus explicitly taking into account the effect of free carrier recombination coefficient, surface recombination, carrier mobilities of the active layer and layer thicknesses. This holistic approach allows us to determine to what extent the mobility of materials should be increased and / or the recombination coefficient should be reduced in order to obtain higher FF in PM6:Y6 thick-junctions device. Figure 5.1b showcases simulated *J-V* curves for the 400 nm device in three different scenarios: (1) parameters based on experimental data, (2) when the hole mobility is hypothesised to be 4 times higher than that measured, and (3) when k_2 is reduced by 50% and the hole mobility is also increased by a factor of 4. As demonstrated in Figure 5.1b, lowering k_2 by 2-fold to reach reduced-Langevin recombination and a 4-fold higher hole mobility, compared to what we have previously published for a thick PM6:Y6 system[31,124],

as input parameters, generates a FF in the range of 65-70% (see Table S1 and Figure S1 for details).

Previous approaches to balance charge transport have focused on inclusion of a third component. Various publications have suggested that by adding a small amount of either D or A to a binary BHJ, the third component gives rise to balanced transport and increased solar cell performance.[133–136] The addition of a small amount of a fullerene molecule in polymer/non-fullerene solar cells has also been widely adopted to increase device performance and stability. As a relevant example, adding the fullerene PCBM to the blend of PM6 with Y6 led to a substantial increase of both the hole and electron mobility. [137] This is in agreement with other examples using PCBM as the additive to NFA-based solar cells, where the addition of PCBM resulted in improved mobilities and device performance.[138] However, very little is known on how such changes of morphological properties relate to the energetic landscape of the blend and the competition between charge extraction and recombination. In addition, the optical and electrical contribution of the third component to the binary BHJ, makes the understanding difficult. Thus motivated by these findings and our understanding on the role of molecular additives[139–142], which can enhance polymer crystallization and packing, we changed the vol. % of the incorporated molecular additive in the blend for different junction thicknesses. We note that the best ratio of CN additive in the optimum thickness is 0.5% of the volume[11]; in contrast, with increasing the junction thickness this is no longer the case. By increasing the ratio of the CN to 1.5% (see Table S2 for device performance versus CN content) in the 400 nm thick junction device, the FF enhances to 68%; overall bringing up the PCE to 14.4% (Table 5.1).

Table 5.1. Photovoltaic parameters of PM6:Y6 for different thicknesses and solvent additive ratios.

Thickness[nm]	Additive ratio	J_{sc} $[mA\ cm^{-2}]$	V_{oc} $[V]$	FF [%]	PCE [%]
100*	0.5%CN	26.3	0.82	73.4	15.9
400*	0.5%CN	25.5	0.81	58.5	12.2
400*	1.5%CN	26.3	0.81	68.1	14.4
400[1]	0.5%CN	25.7	0.81	58.0	12.0
400[2]	0.5%CN	24.4	0.80	60.7	11.8

400[3]	0.5%CN	25.8	0.82	66.8	14.1

* Experimental data

Simulation:

[1] based on experimental parameters

[2] based on experimental parameters except $\boldsymbol{\mu_h}$ 4-fold increased

[3] based on experimental parameters except $\boldsymbol{\mu_h}$4-fold increased and $\boldsymbol{k_2}$ 2-fold decreased

Figure S2 shows the comparison of the external quantum efficiency (EQEPV) of the two thick junction devices where we indeed observe the shape of the absorption edge of the CT state to be visibly affected. In the following, to reveal the origin behind this improvement in the FF just by changing the solvent additive ratio, we study the disorder and its implication on the charge transport properties and non-geminate recombination.

Energetic disorder values can be obtained from temperature-dependent SCLC measurements. To this end, we conducted temperature dependence of the *J-V* characteristic of PM6:Y6 hole-only and electron-only diodes to investigate their SCLC characteristics at different junction thicknesses and with the two different additive contents.

According to the Mott-Gurney quadratic equation[143], by assuming a uniform charge carrier mobility, the steady-state current density (J_{SCLC}) is theoretically a function of the applied voltage (V), the film thickness (d), and the steady-state charge carrier mobility (μ_{SCLC}):

$$J_{SCLC} = \frac{9}{8}\mu_{SCLC}\varepsilon_r\frac{V^2}{d^3} \tag{5.45}$$

The log-log dependence of the current density on the applied voltage is expressed by slope 2; however, in some systems, a slope higher than 2 has been observed which can originate from shallow traps or energetic disorder[22,144,145], carrier density dependent mobilities and deep traps[146–148]. In order to describe this feature, an extended version of Equation 5.45 was introduced by Murgatroyd and Gill[149]:

$$J_{SCLC} = \frac{9}{8}\varepsilon_r\frac{V^2}{d^3}\mu_0 \,.\exp(0.89\gamma\sqrt{\frac{V}{d}}) \tag{5.46}$$

where μ_0 and γ are the (temperature-dependent) zero-field mobility and field enhancement factor, respectively.

According to the Gaussian disorder model (GDM)[22,149], the zero-field mobility is described by:

$$\mu_0(T) = \mu^* \exp\left(-0.44(\frac{\sigma}{k_BT})^2\right) \tag{5.47}$$

where μ^*, k_B, T and σ are the mobility at infinite temperature, Boltzmann constant, temperature and the static Gaussian energetic disorder parameter, respectively. Table 5.2 summarizes the energetic disorders for the highest occupied molecular orbital (HOMO) - σ_{IE} - and the lowest unoccupied molecular orbital (LUMO) - σ_{EA} - in PM6:Y6 devices which have been calculated from GDM fitting of the SCLC data at different temperatures (see Figure S3 and Figure S4). We conclude that energetic disorder for electrons σ_{EA} and holes σ_{IE} of PM6:Y6 at 100 nm thickness with 0.5%CN solvent additive to be as low as 59 and 63 meV, respectively. These values are in agreement with recent publication by Durrant and co-workers measuring low charge trapping (in thin junctions).[150] We note that we have previously reported higher values of $\sigma_{EA} = 71\text{meV}$ and $\sigma_{IE} = 83\text{meV}$.[31] The lower energetic disorder values reported here most likely arise from a higher purity and less defects in PM6 and Y6 batches we have used in this work; which may be a possible reason for higher device performance than other similar works.[11,151–153] By increasing the active layer thickness to 400nm, the σ_{EA} and σ_{IE} change to 54 and 65meV, respectively, which suggests a slightly higher order in Y6, while compromising the order in PM6. Very strikingly, we observe that by increasing the concentration of the solvent additive (from 0.5%CN to 1.5%CN) for the thick device reduces the energetic disorder mostly in PM6 so that now the σ_{EA} and σ_{IE} are as low as 53 and 61meV, respectively. The low energetic disorder of Y6 LUMO is consistent with the morphology data by Yuan et al., where GIWAXS measurements show well-ordered domains of Y6 in the blend.[11] It is anticipated that these domains are further ordered in thick junctions. 2D-GIWAXS was employed to investigate the bulk molecular packing structures of thin and thick PM6:Y6 films. The 2D-GIWAXS patterns and the corresponding line-cut profiles of the different blends are shown in Figure 5.2. With the addition of extra CN, the peaks at q_{xy}= 0.42 Å^{-1} (from Y6), 0.64 Å^{-1} (from PM6), and 0.28-29 Å^{-1} (from both PM6 and Y6, Figure S5) along the in-plane (IP) direction were intensified, which suggests the crystalline packing in both donor and acceptor phases are enhanced. The d-spacing of π-π stacking (010) diffraction in the out-of-plane (OOP) decreased from 3.70 Å for the pristine PM6:Y6 blend films to 3.65 Å and 3.57 Å for 100 nm thick and 400 nm thick blends with 0.5% CN and 3.59 Å for the 1.5% CN in 400 nm thick sample, showing tightly packed structures with CN addition. In addition, the crystal coherence length (L_C) of the OOP (010) scattering shows the same tendency: 2.19 nm (100 nm thick without CN), 2.37 nm (400 nm thick with 0.5% CN), and 2.55 nm (400 nm thick with 1.5% CN) for PM6: Y6 blend films, respectively. These observations suggest that increasing the CN content causes a more phase-separated morphology, with a higher composition contrast and an improved crystallinity of the individual domains. In addition, the elevated crystalline packing in both donor and acceptor

phases increases the coherence length which may indicate enhancement of the phase purity; this in turns may be responsible for reduced recombination by stabilising separated charges in respective domains.

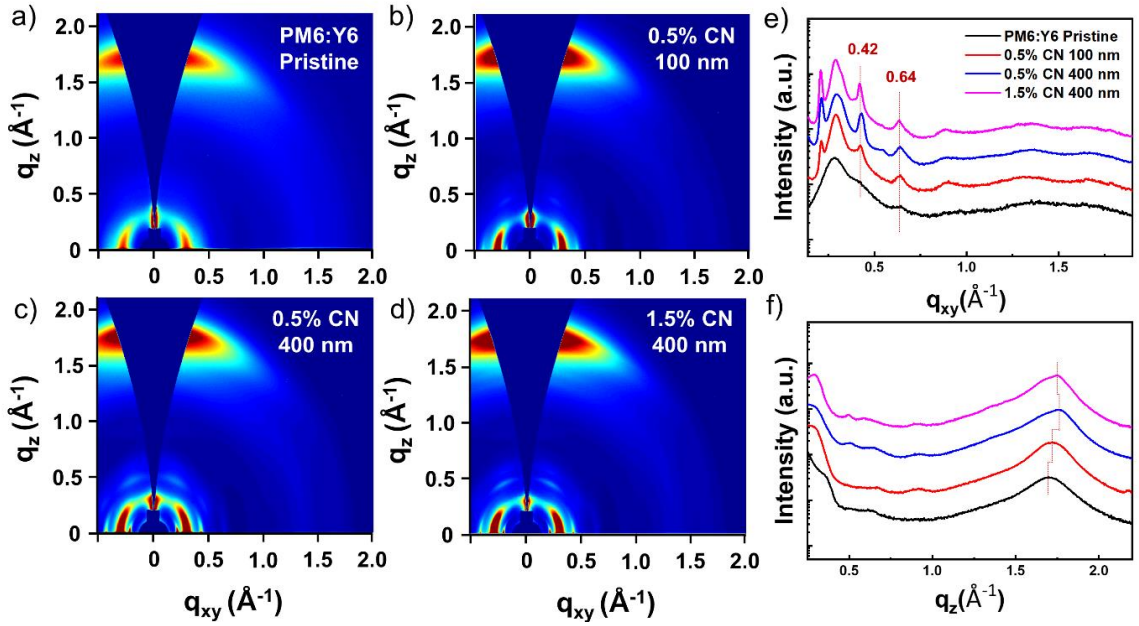

Figure 5.2. 2D-GWAXS images (a-d) and corresponding in-plane (e) and out-of-plane (f) line-cuts of PM6:Y6 blend films with varying film thickness and CN contents.

From SCLC data at room temperature we can also extract the electron and hole mobilities (μ_e and μ_h) of all three devices.

The *J-V* curves for electron-only and hole-only PM6:Y6 diodes show that the voltage dependence is significantly stronger than what is expected from Mott–Gurney's law (see Figure S3); therefore, to obtain the zero-field mobilities at room temperature, Equation 5.46 has been employed. Table 5.2 lists the obtained electron and hole mobilities of PM6:Y6. It is striking to observe the carrier mobilities depend on the thickness of the material instead of being an intrinsic property of the material, such that by increasing the active layer thickness from 100 nm to 400 nm, the μ_e increases from 1.2×10^{-4} $cm^2V^{-1}s^{-1}$ to 1.1×10^{-3} $cm^2V^{-1}s^{-1}$; however, μ_h decreases from 7.1×10^{-5} $cm^2V^{-1}s^{-1}$ to 2.1×10^{-5} $cm^2V^{-1}s^{-1}$. Whilst the latter observation in organic systems is typically assigned to traps/ disorder, the increase in carrier mobility with thickness appears to be rare.[154] On the other hand, when the ratio of the solvent additive increases from 0.5%CN to 1.5%CN for the thick devices, whilst μ_e is only slightly improved to 1.5×10^{-3} $cm^2V^{-1}s^{-1}$, the hole mobility increases by almost 3.6 folds (7.5×10^{-5} $cm^2V^{-1}s^{-1}$).

Table 5.2. Energetic disorder parameter for the LUMO ($\boldsymbol{\sigma_{EA}}$) and HOMO ($\boldsymbol{\sigma_{IE}}$), and electron ($\boldsymbol{\mu_e}$) and hole ($\boldsymbol{\mu_h}$) mobilities in PM6:Y6 for different thicknesses and solvent additive ratios.

Thickness[nm]	Additive ratio	$\sigma_{EA}\ [meV]$	$\sigma_{IE}\ [meV]$	$\mu_e[$ $\times 10^{-4}\ cm^2V^{-1}s^{-1}]$	$\mu_h\ [$ $\times 10^{-4}\ cm^2V^{-1}s^{-1}]$
100	0.5%CN	59	63	1.2	0.71
400	0.5%CN	54	65	11	0.21
400	1.5%CN	53	61	15	0.75

The changes in the carrier mobility with thickness and additive content are consistent with the changes in the observed structural and energetic disorder measured and the hopping model whereby reduction of the energetic disorder results in better carrier mobility. However, from the D-D simulations (Figure 5.1b) it is apparent that a 4-fold increase of hole mobility alone is not sufficient to have FF values for the 400 nm device close to that at 100 nm (73%). Thus, we now turn our attention to exam the impact of the disorder on recombination coefficient.

To investigate bimolecular recombination, we employed bias assisted charge extraction (BACE) technique. In a BACE measurement, the device is initially illuminated with a constant light intensity when it is held at a pre-bias voltage that is exactly the V_{OC} of the device at a given illumination intensity. Under this condition, the recombination of free carriers is equal to the charge generation (G), so that

$$G = R = \frac{J_G}{q.d} \tag{5.48}$$

where J_G is the generation current and equals to the saturated photocurrent (J_{sat}) at a reverse bias voltage, since charge generation is field independent. When the illumination which is a light emitting diode (LED) is turned off, the external bias is rapidly changed to a reverse bias in order to extract all charge carriers present in the device; hence, the recombination coefficient for bimolecular recombination (k_{eff}) is determined. Figure 5.3 shows the bimolecular recombination coefficient as a function of charge carrier density for all three devices. Steady-state measurements (BACE) yield second order recombination properties. For the original thin and thick devices the bimolecular recombination coefficient is $2.9 \times 10^{-17}\ \mathrm{m^3 s^{-1}}$ and $9.1 \times 10^{-18}\ \mathrm{m^3 s^{-1}}$, respectively (despite of the lower bimolecular recombination coefficient in the thick device, the mobilities start to deviate toward imbalanced, leading to lower FF). However, in the thick device with 1.5% additive, the bimolecular recombination coefficient is suppressed

by 50%, so that at one sun illumination condition this value reduces from 9.1×10^{-18} m^3s^{-1} to 4.5×10^{-18} m^3s^{-1}. The recombination coefficient in the 1.5% vol containing CN thick device is over 180 times less than its Langevin recombination limit (k_L) for this system.

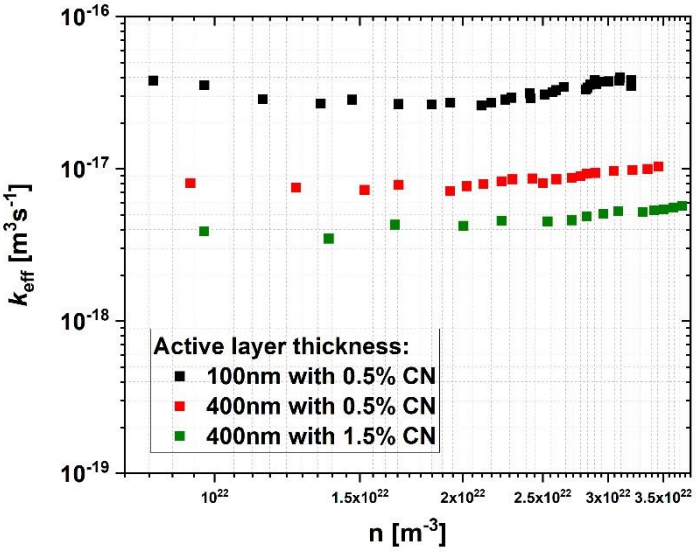

Figure 5.3. Bimolecular recombination coefficient as a function of charge carrier density, obtained from BACE measurements for PM6:Y6 with 100nm thickness (black solid squares) and 400nm thickness with 0.5% CN (red solid squares) and 1.5% CN (green solid squares).

It has recently been proposed that PM6:Y6 suffers from back electron transfer (BET) from the CT3 to form triplet excitons.[155] In this regard we anticipate that perhaps by reducing disorder, the pathway and the rate for formation of triplet excitons is hindered, which then subsequently results in lower k_2.[60,119]

5.3 Experimental Section/Methods

Solar cell devices fabrication

The polymer PM6 was purchased from 1-Materials. The small molecule electron acceptor Y6 was synthesized according to literature.[11] The solvents chloroform ($CHCl_3$) and the additive 1-chloronaphthalene (CN) were purchased from Carl Roth and Alfa Aesar, respectively. Patterned indium tin oxide (ITO) substrates were precleaned in an ultrasonic bath with Hellmanex, deionized water, acetone, and isopropyl alcohol for 20 min for each of them and then dried by nitrogen. The cleaned substrates were treated by oxygen plasma at room temperature for 4 min at 200 W. After that, they were spin coated with PEDOT:PSS (poly(3,4-ethylenedioxythiophene) polystyrene sulfonate) (at 5000 rpm for 30 s) and then annealed at

150°C for 20 min in air. PM6 and Y6 at a weight ratio of 1:1.2 were dissolved in chloroform (with 0.5 vol% of CN as an additive) with total concentration of 11 mg/ml (for 100nm thickness) and 25 mg/ml (for 400nm thickness) and stirred at room temperature for 4 hours inside the glovebox. Then, active blend solution was spin coated (at 3000rpm for 50 s) on top of PEDOT:PSS layer. Subsequently, the substrates were annealed at 110°C for 10 min. After cooling down, 15 nm PDINO (N,N-dimethyl-ammonium N-oxide)propyl perylene diimide) which was dissolved in methanol with 1 mg/ml concentration, was spin coated on top of the active layer. The substrates were transferred into a vacuum evaporator connected to the glovebox, and 100nm silver was deposited sequentially through a shadow mask under $\approx 1 \times 10^{-7}$ mbar, with an active area of the cells of A =0.011 cm^2 for BACE measurement and A = 0.06 cm^2 for the *J-V* measurement.

SCLC devices fabrication: Hole-only device following the same process as the solar cell device fabrication except for the top contacts which were 20 nm MoO_3 and 100 nm gold. For electron only device, ZnO nanoparticles (Avantama N-10) dissolved on isopropanol were filtered through a 0.45 μm PTFE filter and spin coated onto ITO at 5000 rpm for 30 s in air. The ZnO substrates were annealed at 120°C for 30 min. The layers on top of ZnO are the same as solar cell devices.

Current density-voltage characteristics

J-V curves were measured by using a Keithley 2400 system in a 2-wire source configuration. Simulated AM1.5G irradiation at 100 $mWcm^{-2}$ was provided by a filtered Oriel Class AAA Xenon lamp and the intensity was monitored simultaneously with a Si photodiode. The sun simulator is calibrated with a KG5 filtered silicon solar cell (certified by Fraunhofer ISE). For the *J-V* measurements as function of temperature, the sample was placed in a nitrogen cryostat. And then the *J-V* curves were measured by using the same Keithley.

Bias-assisted charge extraction

To establish steady-state conditions, we used a high power 1 W, 638 nm laser diode (insaneware) with a switch-off time of 10 ns. The laser diode was operated at 500 Hz with a duty cycle of 50%, such that illumination lasted 1 ms and the diode was switched off for also 1 ms. A pulse generator (Agilent 81150A) was used to apply the prebias (V_{OC}) and collection bias which are amplified by a home-built amplifier, allowing a fast extraction time of 10-20 ns. The current transients were measured via a 10 Ω resistor in series with the sample and recorded with an oscilloscope (Agilent DSO9104H).

2D-GWAXS measurement

2D-GIWAXS measurement was performed at the beamline 9A in the Pohang Accelerator Laboratory (South Korea, beam energy: 11.07 keV, X-ray wavelength: 1.12002 Å and the incident angles: 0.12-0.14°). 2D-GIWAXS samples were prepared on bare Si substrates under same fabrication conditions used for the optimized devices.

5.4 Conclusion

To conclude, in this study, we succeed in improving the PCE of 400nm thick PM6:Y6 device from 12.2% to14.4% (increasing the FF from 58% to 68%) by adjustment of the amount of the solvent additive in the active blend solution. Our investigations represent that changing the volumetric content of solvent additive from 0.5%CN to 1.5%CN in the thick PM6:Y6 device leads to increases in both electron and hole mobilities. Our data from temperature-dependent SCLC and morphology measurements show that the origin behind these enhancements in the mobilities comes from the lower disorders in the thick device with 1.5%CN. Simultaneously we observe a reduction in the recombination coefficient of free carriers, which may be due to phase purity or higher order in the blend. Simulation data confirm our experimental findings that performance of PM6:Y6 device in thick junctions can be improved through controlling the packing, purity and crystallinity of PM6 and Y6 to suppress the bimolecular recombination whilst enhancing the carrier mobility. Our findings are likely to have important applications for improving not only the charge transport and recombination properties of polymer diodes, light-emitting diodes, and solar cells, but might also allow the improvement of other characteristics of these devices, including reducing trap-assisted non-radiative recombination.

Chapter 6. Extraordinarily long diffusion length in PM6: Y6 organic solar cells

In this chapter, we analyse PM6:Y6 solar cell to understand the observed independence of the short-circuit current upon photoactive layer thickness. We employ a range of optoelectronic measurements and analyses, including Mott-Schottky analysis, CELIV, photoinduced absorption spectroscopy, Kelvin-probe potential measurements and simulations, to conclude that, for the device series studied, the invariant photocurrent for devices with different active layer thicknesses is associated with the Y6 diffusion length exceeding 300 nm. This is despite an unintentional doping that occurs in PM6 and the associated space-charge effect, which is expected to be even more profound upon photogeneration. This extraordinarily long diffusion length - which is an order of magnitude larger than typical values for organics - dominates transport in the flat-band region of thick junctions. Our work suggests that the performance of the doped PM6:Y6 organic solar cells resembles that of inorganic devices with diffusion transport playing a pivotal role. Ultimately, this is expected to be a key requirement for the fabrication of efficient, high-photocurrent, thick organic solar cells. The supplementary information of this paper can be accessed online at (https://pubs.rsc.org/en/content/articlelanding/2020/TA/D0TA03016C#!divAbstract).[124]

6.1 Introduction

In 2019, the non-fullerene acceptor (NFA) Y6 blended with PM6 achieved power conversion efficiencies (PCE) of 15%.[156] In 2020 Y6 blended with an alternative polymer gave 17.6% certified efficiency.[12] With the PCE of NFA based organic photovoltaic devices reaching the performance level of first-generation polycrystalline silicon technologies, the feasibility of commercial solutions is becoming increasingly realistic.[157–159] One of the significant obstacles which must still be overcome en route to commercialization is the low thickness of most typical organic active layers which rarely exceeds the 100 nm range.[160] Determination of, and addressing the causes of such limitations requires building a general energetic picture of photovoltaic semiconductor junctions, which is a very important tool for understanding of the role of different materials and electronic processes. Conventional understanding of solar cell operation which has been initiated and driven by the studies of inorganic crystalline materials is mainly based on the models of the p-n junction and p-i-n solar cell, where the electric field is of little relevance for charge collection at short circuit, while instead charge separation relies on interfacial kinetics, energy steps at interfaces and diffusion driven transport.[161,162] However with the discovery of the bulk heterojunction organic solar cells (BHJ), due to the low charge

mobilities and low diffusion coefficients (the charge carrier diffusion lengths are typically <20 nm[96,163,164]) a series of new device models has been established where the role of charge collection by electric fields (drift transport) is essential to the solar cell performance, since purely diffusive transport does not lead to efficient charge extraction.[165] One consequence of this reliance on drift transport is that organic solar cells are typically thin – on the order of hundreds of nanometres – compared to their inorganic counterparts – microns to tens of microns thick cells. In this regard, it has previously been shown that low charge mobilities may consequently limit both the short-circuit current (JSC) and the fill factor (FF) of organic solar cells.[30,85,96] In particular, organic bulk heterojunctions typically show lower JSC values for thicknesses above a particular threshold, despite an increase in the number of absorbed photons.[164]

Among the organic blends demonstrating promising output characteristics at higher active layer thicknesses, the PM6:Y6 (PM6: poly[(2,6-(4,8-5is(5-(2-ethylhexyl-3-fleoro)thiophen-2-yl)-5enzo[1,2-5:4,5-5']dithiophene))-alt-(5,5-(1',3'-di-2-thienyl-5',7'-5is(2-ethylhexyl)5enzo[1',2'-c:4',5'-c']dithiophene-4,8-dione)]; Y6: 2,20-((2Z,20Z)-((12,13-bis(2-ethylhexyl)-3,9-diundecyl-12,13-dihydro-[1,2,5]thiadiazolo[3,4-e]thieno[2,"30':4',50]-thieno[20,30:4,5]pyrrolo[3,2-g]thieno[20,30:4,5]thieno[3,2-b]indole-2,10-diyl)bis(methanylylidene))-bis(5,6-difluoro-3-oxo-2,3-dihydro-1H-indene-2,1-diylidene))dimalononitrile) NFA based blend has recently gained much attention showing PCE of around 15% in 100 nm and even still impressive 13% for the 300-nm thick active layer devices.[156] We have previously studied the mechanism of charge generation in a 100-nm thick PM6:Y6 device and found that photocurrent generation is essentially barrierless with near-unity efficiency. Theoretical modelling suggests that efficient charge separation is related to the ability of Y6 to form crystalline domains in the optimized blend. Thereby, the dissociation of the interfacial CT state is assisted by an electrostatic interfacial field which for crystallized Y6 is large enough to compensate the Coulomb dissociation barrier. [31] Profiting from this crystallinity effect are the high JSC and electron mobility values obtained in the PM6:Y6 blends. However, a question of interest which still remains lucid is how the photocurrent depends on thickness, particularly in thicker junctions. The observed constant JSC for different active layer thicknesses indicates insignificant bimolecular recombination.[96,166] In this paper, we employ Mott-Schottky analysis of the PM6:Y6 depletion region, supported by CELIV, to study the thickness dependence of the device behavior. To interpret the experimental observations, we use numerical simulations that incorporate the effect of doping on the device electrostatics. We demonstrate that high performance in thicker PM6:Y6 devices is due to the

significantly enhanced electron diffusion length, enabling efficient operation even for doped blends.

6.2 Results and discussion

For comparison of operation of thin and thick PM6:Y6 devices two active layer thicknesses of 100 nm and 300 nm were employed. Figure 6.1 shows the *J-V* curves of the two devices in the dark and under 1 Sun illumination. Similar to the results reported previously,[156] the increase in the active layer thickness in these standard architecture devices does not cause a notable change in the V_{OC} and J_{SC}, while the FF is reduced, albeit less significantly than what is typically observed in organic photovoltaic blends.[164] Whilst the drop in the FF can be assigned to increased recombination, it is striking that the J_{SC} barely changes with thickness up to several hundreds of nanometers. This observation is different to most other organic systems where the J_{SC} increases due to enhanced light absorption until the optimum value at a finite junction thickness, followed by noticeable decrease (such as in the case of PCDTBT) for thicknesses thereafter.[164]

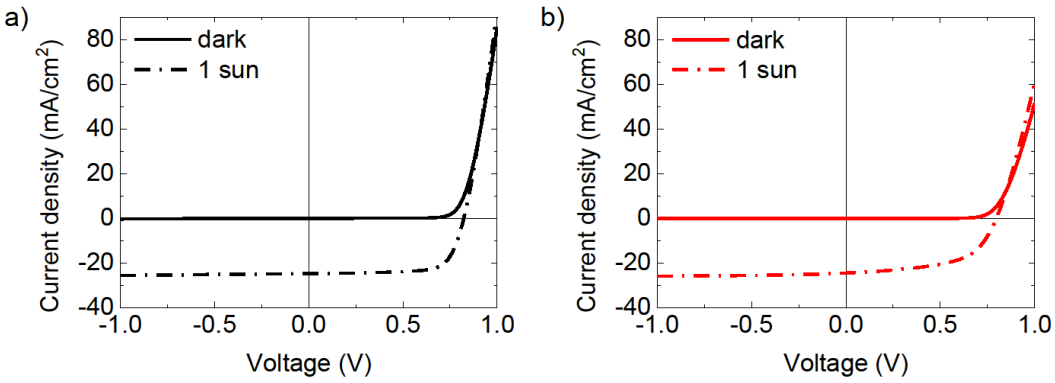

Figure 6.1. *J-V* characteristics of the PM6:Y6 devices with active layer thicknesses of 100 nm (a) and 300 nm (b).

Figure 6.2 shows the external quantum efficiencies of the two devices. It can be seen that consistent with the invariant J_{SC}, the EQE also remains significantly unchanged in magnitude across the entire wavelength spectrum.

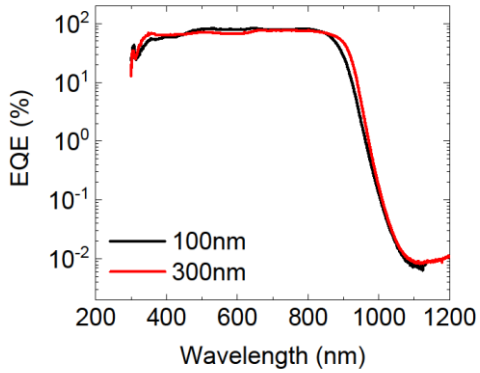

Figure 6.2. External quantum efficiency spectra of the PM6:Y6 devices with active layer thicknesses of 100 nm and 300 nm.

It has previously been shown that photocurrent generation in organic solar cells can be correlated with the depletion layer width with respect to the junction thickness.[164,167] Thus, undoped devices with the depletion region extending throughout the active layer are expected to show better performance than the doped devices with similar device architecture.[168] To determine the depletion region in the device, capacitance-voltage experiments were performed. Capacitance-voltage measurements are an established technique used to determine the doping density of a semiconductor.[169] The capacitance-voltage analysis of organic solar cells, based on Mott-Schottky formalism, enables to obtain some of the important device parameters, including active layer doping, depletion layer width etc., thereby helping to build a more comprehensive model of the device operation.[167] By conducting the measurements in the dark, where the mobility of the carriers does not affect the device electrostatics, we can establish the depletion region caused by unintentional doping rather than a mobility imbalance.[167,170]

The results of the capacitance-voltage experiments in the dark and the Mott-Schottky plots for the 100-nm and 300-nm devices, along with the derivative doping profiles across the active layer width are demonstrated in Figure 6.3. The doping profiles were obtained similarly to Refs. [31] and [166]. The linear descending region of the Mott-Schottky plot in Figures 6.3a and 6.3b is expected to follow the expression:

$$\frac{A^2}{C^2} = \frac{2(V_{BI}-V)}{q\varepsilon\varepsilon_0 N_{app}} \tag{6.49}$$

where A is the device area, C is the capacitance, V_{BI} is the built-in voltage, q is the elementary charge, ε is the relative permittivity of the active layer, ε_0 is the vacuum permittivity and N_{app} is the doping concentration. This enables to estimate the apparent bulk doping level within the active layer: $N_{app} = 2\times10^{16}$ cm^{-3} for the 100 nm cell, and $N_{app} = 8\times10^{15}$ cm^{-3} for the 300 nm cell. Although the difference in the obtained doping concentrations is not significant, previous reports of validity of the Mott-Schottky analysis suggested that the values obtained for thinner

active layers are less reliable since the junction is almost fully depleted and dark injection becomes dominant.[171,172] As such, we will employ the doping concentration obtained for the 300 nm device for further analysis.

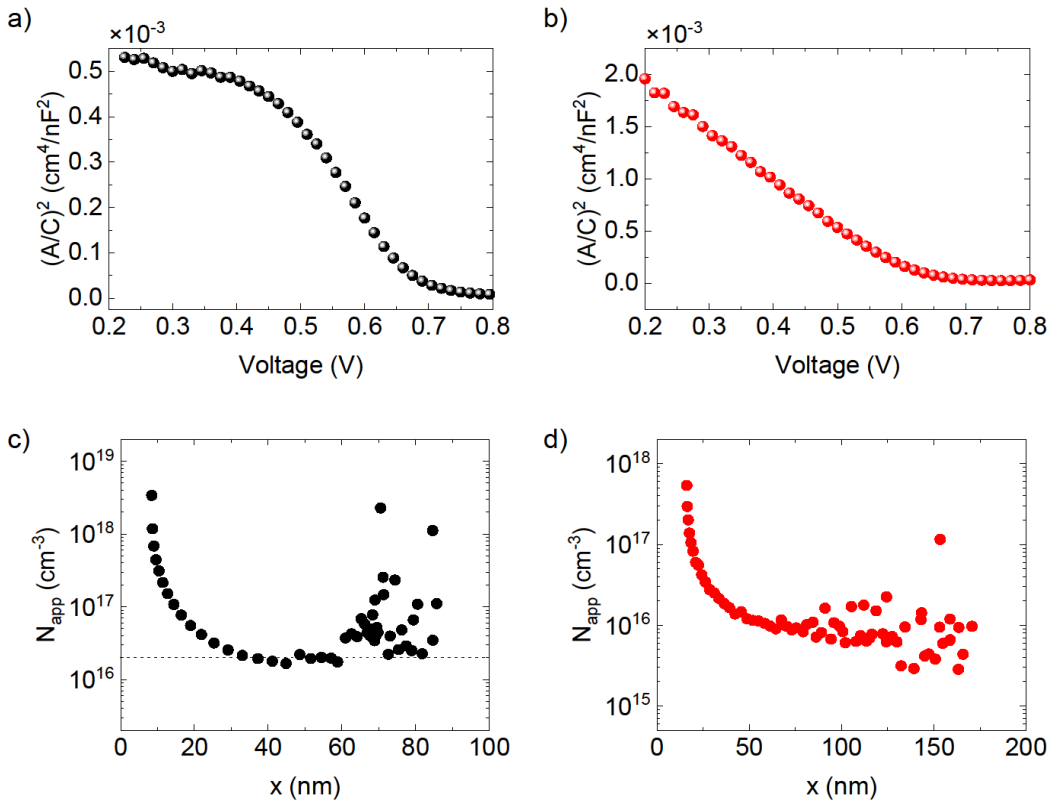

Figure 6.3. Mott-Shottky plots (a, b) and apparent doping profiles (c, d) of the PM6:Y6 devices with active layer thicknesses of 100 nm (a, c) and 300 nm (b, d).

The doping concentration in the 300 nm PM6:Y6 device was confirmed via the charge extraction by linearly increasing voltage (CELIV)[173] measurements, yielding the value of 8.7×10^{15} cm^{-3}. Experimental current density transients in Figure 6.4 are presented in the form of j^{-2} as a function of (Rt + U_{off}), where R is the pulse ramp-up rate, t is time, and U_{off} is the offset voltage. The pulse ramp-up rate of 0.8V/50μs and the offset voltage of -0.5 V were used in the measurement. The red lines represent linear fits, enabling to estimate the carrier concentration via expression:

$$slope = \frac{2}{q\varepsilon\varepsilon_0 R^2 N_p} \tag{6.50}$$

where q is the elementary charge, ε is the dielectric constant and N_p is the doping concentration.[174]

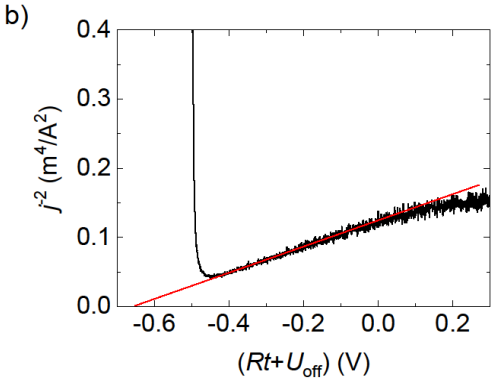

Figure 6.4. Experimental current density transient obtained in the CELIV measurement for the 300-nm thick PM6:Y6 device at the pulse ramp-up rate of 0.8V/50μs and the offset voltage of -0.5 V.

The C-V measurements enable to estimate the width of the depletion region x via

$$x = \frac{\varepsilon\varepsilon_0 A}{C} \tag{6.51}$$

which at J_{SC} (V = 0V) is equal to 85 nm for the 100-nm device and 170 nm for the 300-nm device. This suggests that a significant part of the active layer within the 300 nm cell remains in the flat-band condition. It has previously been suggested that the discrepancy between the depletion width and the photoactive layer thickness d ($x < d$) can lead to substantial losses in photocurrent due to an inefficient collection of charges generated in the low-field part of the cell outside the high-field depletion region. However, our measured effective space charge width in the 300 nm junction device, cannot explain the J_{SC} value similar to that obtained in the thinner optimized cell.

The above depletion width picture is confirmed by simulations of the device band diagrams and the *J-V* characteristics, using AFORS-HET,[132] where the active layer doping level obtained from the Mott-Schottky analysis was employed (see Table 6.1 for simulation parameter details). The respective simulated energy band diagrams taking into account the impact of doping on band bending within the active layer are given in Figure 6.5. It is evident, that while the 100-nm cell is almost fully depleted at J_{SC} (V = 0 V), resulting in the electric field which extends across the whole width of the active layer, in the 300-nm cell the active layer is only partly depleted. In the thick device, the depletion region will occupy about half of the active layer closest to the cathode. The remaining half of the device thickness is defined as the neutral region and in this part of the device there is little electric field. Therefore, while in the 100-nm cell the dominant charge transport mechanism is bound to be the drift of the carriers, for the 300-nm

device however, carrier diffusion has to play a more significant role in order to avoid loss in the photocurrent.

Table 6.1. Parameters for the AFORS-HET simulation of energy band diagrams and performance of the organic solar cells with structure ITO/PEDOT:PSS/PM6:Y6/PDINO/Ag for various active layer thicknesses.[132]

Parameter	PEDOT:PSS	PM6:Y6	PDINO
Thickness [nm]	30	100, 300	5
Relative dielectric constant	2.2	3.5	5
Band gap [eV]	3.0	1.27	2.6
Electron affinity [eV]	2.2	4.1	3.7
Effective density of states [cm^{-3}]	10^{21}	10^{20}	1.5×10^{20}
Band-to-band recombination coefficient [cm^3s^{-1}]		1.7×10^{-11}	
Electron mobility [$cm^2\ V^{-1}\ s^{-1}$]	10^{-7}	$1\text{-}2.5\times10^{-3}$	5×10^{-1}
Hole mobility [$cm^2\ V^{-1}\ s^{-1}$]	0.77	2×10^{-4}	10^{-7}
Doping concentration [cm^{-3}]	2.25×10^{20}	8×10^{15}	10^{10}
Anode hole surface recombination velocity [cm s^{-1}]	10^7	-	-
Anode electron surface recombination velocity [cm s^{-1}]	10^2	-	-
Cathode electron surface recombination velocity [cm s^{-1}]	-	-	10^7
Cathode hole surface recombination velocity [cm s^{-1}]	-	-	10^2

Typically in inorganic thin film solar cells, the ratio x/d varies from around 10% in $Cu(In,Ga)Se_2$ (CIGS) to 100% in fully depleted devices like amorphous Si.[175–177] When going from small to large values of x/d, the mechanism by which charge generation occurs changes. While devices with low x/d are controlled by diffusion such as in the case of c-Si and dye-sensitized solar cells (DSSC), the larger the space charge region becomes relative to the absorber thickness, as in a typical 100 nm organic solar cell, the more drift will affect charge carrier collection.

The diffusion length, l_d can be calculated using the formula:

$$l_d = \sqrt{\frac{k_B T}{q} \mu \tau} \tag{6.52}$$

where μ is mobility, and τ is the carrier recombination lifetime. The space-charge limited current (SCLC) measurements (Figure 6.6)[119] in the 300 nm device, yields mobility values of $\mu_e = 4\times10^{-3}$ cm^2 V^{-1} s^{-1} and $\mu_h = 2\times10^{-4}$ cm^2 V^{-1} s^{-1} for the electrons and the holes, respectively. It is interesting to note that the electron mobility is about an order of magnitude higher than most other NFAs reported recently.[178–180] The carrier recombination lifetime, obtained from photoinduced absorption (PIA) measurements[112] at the open circuit condition (Figure 6.7), is 9.8×10^{-6} s. It should be noted that the open circuit condition is relevant in this case since carrier diffusion in the neutral region of the active layer is being considered. As a result, the electron and hole diffusion lengths are estimated to be 330 nm and 70 nm, respectively. These rather high estimated carrier diffusion length values in the 300-nm cell may provide an explanation to the observed device performance, specifically, the high J_{SC} value.[168]

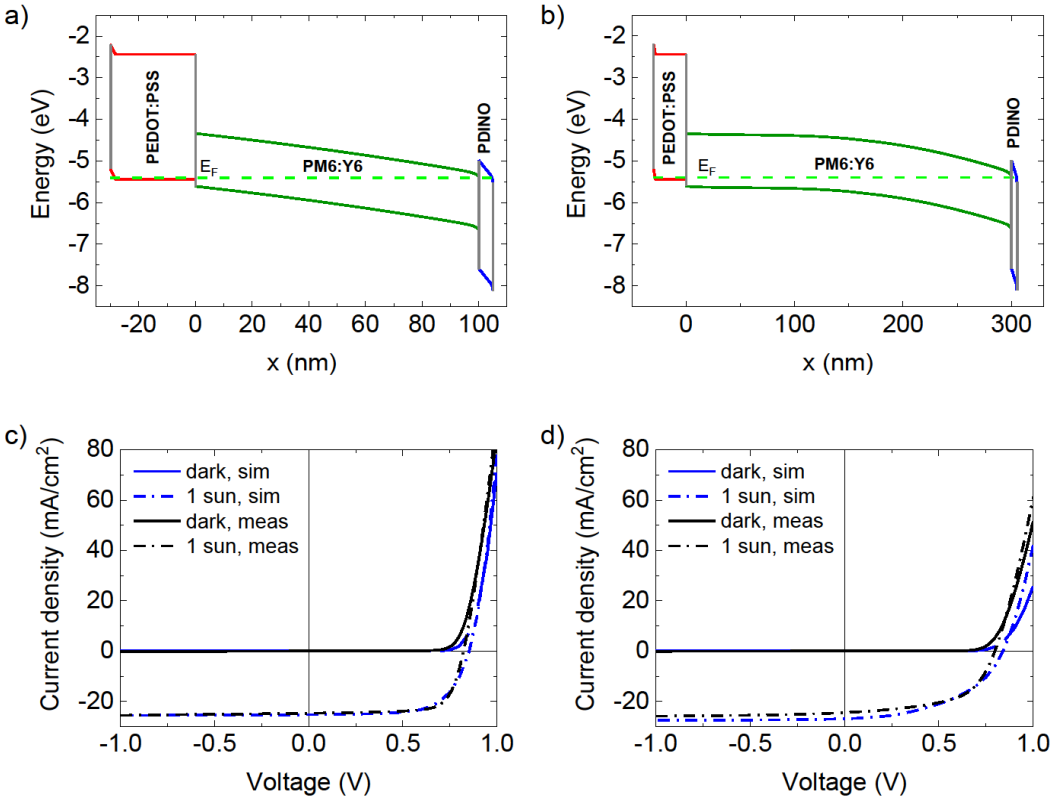

Figure 6.5. Simulated energy band diagrams at the "short circuit" condition (a, b) and comparison of simulated and measured *J-V* characteristics (c, d) of the PM6:Y6 devices with active layer thicknesses of 100 nm (a, c) and 300 nm (b, d). See Table 6.1 for simulation parameter details.

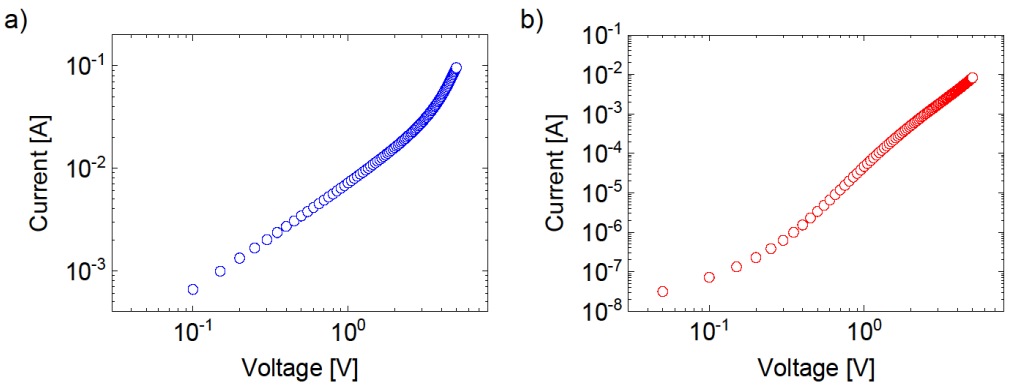

Figure 6.6. Space-charge limited current (SCLC) vs. voltage curves for the 300 nm-thick PM6:Y6 devices with the following structures: a) ITO/ZnO/PM6:Y6/PDINO/Ag, b) ITO/PEDOT:PSS/PM6:Y6/MoO_3/Au.

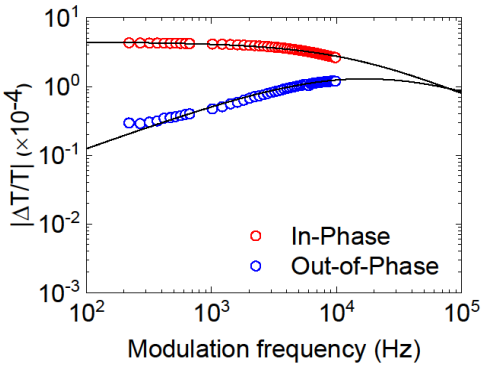

Figure 6.7. Photoinduced absorption spectroscopy characteristics of the ITO/PEDOT:PSS/PM6:Y6/PDINO/Ag (35 nm) photovoltaic devices at the open circuit condition. Global fitting of the measured in-phase and out-of-phase data points provides the average carrier lifetime value of 9.8×10^{-6} s.

Our analyses above show that PM6:Y6 exhibits high electron mobility and slow carrier recombination which result in the large carrier diffusion length. This diffusion length is greater than the width of the flat-band region and can be responsible for the efficient photocurrent in thick junctions where the depletion region does not extend over the entire active layer thickness. In this respect, the operation of the thicker PM6:Y6 device resembles that of conventional silicon cells and DSSCs, in terms of a significant part of the active layer remaining in the flat-band condition and charge transport relying mainly on diffusion. Another advantage of the long diffusion length and low *x*/d, is the reduced Shockley–Read–Hall (SRH) recombination in the neutral region, since the minority carrier concentration is smaller than the majority carrier concentration.[181]

6.3 Experimental Section/Methods

Solar cell devices fabrication

PM6 was purchased from 1-material and Y6 was provided by Central South University and synthesized according to literature.[156] For device fabrication, ITO-coated glass substrates were cleaned in an ultrasonic bath using detergent, deionized water, acetone and isopropyl alcohol (IPA), the dried substrates were treated by oxygen plasma at room temperature for 4 min. PEDOT:PSS (poly(3,4-ethylenedioxythiophene): poly(styrene sulfonate)) (Baytron PVP Al 4083) was spin-coated on ITO and annealed for 15 min at 150°C in the air. PM6 and Y6 were mixed in the 1:1.2 proportion, dissolved in chloroform and, following addition of 1-chloronaphthalene (CN) (0.5% by volume), spin-cast on top of PEDOT:PSS. An electron-injecting interlayer of PDINO was then spin-cast onto the active layer from the 1 mg/mL solution in methanol. The Ag top electrode was thermally deposited in vacuum at the base pressure of ca. 10^{-6} mbar. The device fabrication was completed by glass-on-glass encapsulation in order to perform measurements in the air.

Current-voltage measurements

The solar cell *J-V* characteristics were measured in a 2-wire configuration on a Keithley 2400 system. The light *J-V* measurements were performed using a filtered Oriel class AAA Xenon lamp and calibrated using a Si photodiode.

Capacitance-voltage measurements

The dark C-V measurements were performed using the Keysight E5061B Vector Network Analyzer with the frequency measurement range of 5 Hz to 500 MHz. Prior to the measurements, the tool was calibrated using the 85032E Type N calibration kit. This was followed by the tool compensation procedure using the “Open”, “Short” and “50 Ohm” measurements at the device connection fixture. The measurements were performed in the C_p mode.[170] The performance of the devices was tested both prior to and after the C-V measurements with no sign of degradation.

Mobility measurements

Carrier mobilities were measured in the space-charge limited conduction (SCLC) experiments in nitrogen using non-encapsulated single-carrier devices with the following architectures: ITO/PEDOT:PSS/PM6:Y6/MoO_3/Au for hole-only devices and ITO/ZnO/PM6:Y6/PDINO/Ag for electron-only devices. Extraction of the mobility values was performed by fitting of the

space-charge limited current vs. voltage curves using the Mott-Gurney law, followed by extrapolation to zero bias.

Photoinduced absorption measurements

In the photoinduced absorption (PIA) measurements, wavelength-tunable monochromatic light extracted from a tungsten halogen lamp by a monochromator was directed to a sample as the probe beam, and a 405-nm cw diode laser modulated by an optical chopper was utilised as the excitation beam. The change in intensity of the transmitted probe light induced by the modulated excitation beam was recorded by a Si photodiode and a lock-in amplifier, which was referenced to the modulation frequency of the excitation light. The average lifetime of free carriers then was evaluated based on the modulation-frequency-dependent PIA data.

6.4 Conclusions

In conclusion, using the Mott-Schottky analysis of 100 and 300 nm PM6:Y6 solar cells, supplemented by mobility, PIA measurements and simulations, this paper puts the spotlight on carrier diffusion as an important charge transport mechanism facilitating efficient operation of devices with higher active layer thickness. Specifically, the impact of enhanced carrier diffusion is expected to be significant for doped active layers, with the present work estimating the doping concentration of the order of 10^{16} cm^{-3} for the used PM6:Y6 batch. Although such doping levels would still be compatible with the depletion region extending throughout the whole active layer width within the thinner devices, for the thicker devices it would result in the significant part of the active layer remaining at “flat band”, i.e. with almost no electric field driving carrier transport. In this case, enhanced diffusion, via high carrier mobilities, appears to play an important part in carrier transport, resulting in the better-than-expected device performance.

Chapter 7. Decoding Charge Recombination Through Charge Generation in Organic Solar Cells

In this chapter, we present a meta-analysis of the device performance for numerous bulk heterojunction organic solar cells for which field dependent photogeneration, charge carrier mobility and fill factor are determined. From this analysis we introduce a 'spin-related factor' which is dependent on the ratio of back electron transfer of the triplet CT states to the decay rate of the singlet CT states. We show that this factor links the recombination reduction factor to the charge generation efficiency. As a consequence it's only the systems with very efficient charge generation and very fast CT dissociation that the free carrier recombination is strongly suppressed, regardless of the spin-related factor. The supplementary information of this paper can be accessed online at (https://onlinelibrary.wiley.com/doi/full/10.1002/solr.201900184).[119]

7.1 Introduction

Over the past years, organic photovoltaics (OPV) has evolved considerably. The introduction of the bulk-heterojunction (BHJ) architecture[9] allowed to combine efficient exciton harvesting with efficient free charge generation, which has subsequently lead to development of organic solar cells with power conversion efficiencies (PCEs) now reaching 16%.[182–186] Ease of fabrication has always been the motivation behind OPV, however, deposition of the typically thin active layer (<100nm) over large areas using solution processing is challenging. This thickness limitation is mainly due to the short carrier lifetime relative to the transit time in disordered organic semiconductors. Recent high-efficiency devices underline that free carriers are readily generated within sub-nanosecond time scale of photoexcitation with a high efficiency independent of the internal electric field.[107,187,188] The loss mechanism in organic solar cells is apparently what occurs at longer time scales to the free carriers *i.e.* non-geminate bimolecular recombination of charges. This recombination process with its associated rates is in competition with charge extraction (given by the internal electric field and typically poor charge carrier mobilities). Therefore it is intuitive to understand the non-geminate recombination loss as a voltage dependent process. The fill factor (FF) which is the manifestation of the field dependence of all processes from charge generation to charge collection is believed to be the result of the above competition.[43,44,189]

Because the charge extraction rate is thickness dependent, the recombination loss often scales with active layer thickness and remains as the primary loss factor in thick BHJ solar cells.[190–193] It has been traditionally believed that in organic solar cells with much lower charge carrier mobilities compared to their inorganic counterparts, the recombination can be regarded as a

transport-controlled process in similarity to that occurring in single phase organic compounds or an ionised gas. This is expressed as Langevin-like recombination with a rate constant directly related to the carrier mobilities. However, many systems exhibit reduced bimolecular recombination relative to Langevin rate – beneficial for the operation of the cell in thick junctions. Yet, only very few material systems have shown a significant reduction.[63,95,194] Material and device properties - including morphologic and energetic properties of organic semiconductors - have been examined to extend the Langevin model.[195–197] Recently, several studies suggested that a highly reduced recombination cannot originate solely from the geometric confinement of electrons and holes in their respective nano-domains[196] and any significantly reduced recombination should be related to very efficient re-dissociation of charge transfer states.[63,198,199] The basic idea behind the concept is that the encounter of free carriers causes the re-formation of CT states, meaning that fast dissociation of CT states lowers their steady-state density and thereby reduces the overall recombination via the CT decay to the ground state or to the triplet exciton states. Provided that the same manifold of CT states is involved in free charge formation and recombination, systems with strongly reduced recombination should also exhibit nearly perfect charge photogeneration. However, such correlation cannot be directly observed from internal quantum efficiency (IQE). This is mainly because the IQE is not only affected by the photogeneration but also by the pseudo-first order and second order recombination of free charges. Therefore, establishing the most relevant physical model to relate the recombination and photogeneration has remained a challenge to date; which demands for approaches to treat the competition between charge extraction and recombination of free carriers with respect to their photogeneration rate.

In this study, based upon new and previously published data, we analyse over 20 donor:acceptor blends systems (chemical structures given in Scheme 7.1) employing fullerene and non-fullerene acceptors blended with ten different donors, at different blend ratios and processing conditions – to study the role of charge generation kinetics upon non-geminate recombination. We show for the first time how field dependent charge generation, obtained from time delayed collection field (TDCF), and bimolecular recombination coefficient obtained from bias assisted charge extraction (BACE) at operating charge carrier densities, and mobilities (using space charge limited current (SCLC), resistance dependent photovoltage (RPV) or TDCF) are related to one another and correlate with the fill factor. We will unify previous models for suppression of bimolecular recombination by introducing a ‘spin related factor’ which is dependent on the ratio of back electron transfer rate of the triplet CT states to the decay rate of the singlet CTs.

From the meta-analysis it will be shown that geometrical confinement plays no role on the suppression of bimolecular recombination.

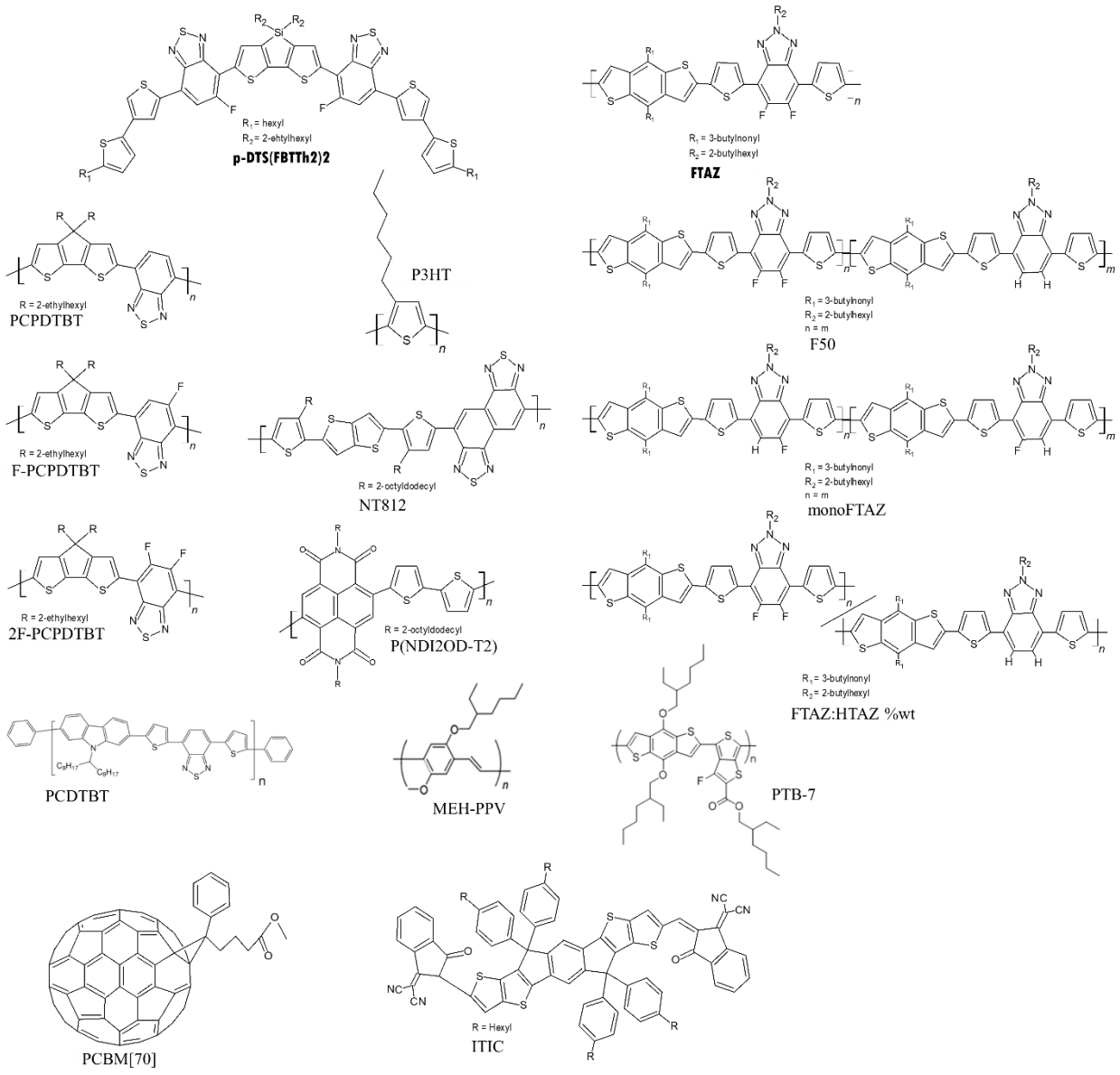

Scheme 7.1: Chemical structure of the donors and acceptors studied in this work.

The work presents a satisfying understanding of the relation between field dependent photogeneration, charge collection and the FF. The results presented here, for the first time visualise that efficient CT state dissociation as seen from field independent photogeneration suppresses bimolecular recombination and increases the FF. Furthermore, we provide a model to explain the role of spin in the interplay between charge photogeneration and recombination in various donor:acceptor systems and introduce a spin-related factor which quantifies the relative strength of triplet and singlet CT state loss channels.

When the dissociation yield of excitons is nearly perfect, charge generation efficiency can be approximated as the dissociation efficiency of the CT states

$$\eta_{\mathrm{CG}} \approx \eta_{\mathrm{diss,CT}} = \frac{k_d}{k_f + k_d}, \tag{7.53}$$

in which k_d is the dissociation rate constant of the CT states to free charges and k_f the CT decay rate constant to the ground state. Assuming similar dissociation efficiency for both singlet (^{1}CT) and triplet CT (^{3}CT) states, the free charge carrier generation rate is $k_d(n_{1\mathrm{CT}} + n_{3\mathrm{CT}})$, where $n_{1\mathrm{CT}}$ and $n_{3\mathrm{CT}}$ are carrier densities for singlet and triplet CT states, respectively. We note that triplet CT states can be generated via intersystem crossing of singlet CT states[200] or via encountering spin uncorrelated free electrons and holes.[201]

At open circuit and steady state condition the net current is zero where the photocurrent is balanced out by the injection current. Kinetics of the charge carriers and the CT states can be written as:

$$\frac{dn_{\mathrm{CS}}}{dt} = -k_{\mathrm{en}} n_{\mathrm{CS}}^2 + k_d(n_{1\mathrm{CT}} + n_{3\mathrm{CT}}) = 0, \tag{7.54}$$

$$\frac{\mathrm{dn}_{1\mathrm{CT}}}{dt} = \frac{1}{4} k_{\mathrm{en}} n_{CS}^2 - \left(k_d + k_f\right) n_{1\mathrm{CT}} + k_{\mathrm{diss,EX}} n_{1\mathrm{EX}} - k_{\mathrm{ISC}}(n_{1\mathrm{CT}} - n_{3\mathrm{CT}}) = 0, \tag{7.55}$$

$$\frac{dn_{3\mathrm{CT}}}{dt} = \frac{3}{4} k_{\mathrm{en}} n_{\mathrm{CS}}^2 - (k_d + k_{\mathrm{BET}}) n_{3\mathrm{CT}} + k_{\mathrm{ISC}}(n_{1\mathrm{CT}} - n_{3\mathrm{CT}}) = 0 \tag{7.56}$$

where n_{CS} is the density of free carriers, k_{en} is the bimolecular encounter rate constant of free carriers with $k_{\mathrm{en}} n_{\mathrm{CS}}^2$ being the rate of regeneration of CT states, $k_{\mathrm{diss,EX}} n_{1\mathrm{EX}}$ is the rate at which singlet CT states are generated from excitons which in ideal quenching condition equals the optical generation rate, G_{opt}. k_{BET} is the rate constant of back electron transfer of triplet charge transfer (3CT) states to form triplet excitons on either the donor or acceptor, k_{ISC} is the intersystem crossing rate between the singlet and triplet CTS. The fractions in equations 7.55 and 4 come from spin statistics: there are 3 combinations of ½ spin that yield a triplet and one that results in a singlet. The encounter rate can be reduced for several reasons, one being due to the geometrical confinement, as well as other morphological reasons[202]– as such all the different factors are termed together under the reduction term 'γ_{en}'' taking into account for any possible mechanism for lowering the encounter rate of the charge carriers. k_{en} can be written in terms of geometrically reduced Langevin rate such that

$$k_{\mathrm{en}} = \gamma_{\mathrm{en}} k_L, \tag{7.57}$$

where $k_L = (\mu_e + \mu_h)e/\epsilon\epsilon_0$ is the Langevin encounter rate and γ_{en} (< 1) the reduction factor due to the confinement of opposite charges in their nano-domains in a BHJ system. It is important to emphasise that all charge recombination occurs via CTS; so the recombination rate is given by the consideration of all loss channels and dead-ends; namely the decay of the singlet

CTS to the ground state and back electron transfer of the triplet CT states to triplet excitons. As such, the recombination rate to the ground state (R) is not simply given by $k_{\mathrm{en}}n_{\mathrm{CS}}^2$, since not all the re-formed CT states are dead-ends; due to CT re-dissociation. Rather, an effective bimolecular recombination coefficient, k_2, of free carriers to the ground state is introduced, which is experimentally observable and defined by

$$R = k_f n_{1\mathrm{CT}} + k_{\mathrm{BET}} n_{3\mathrm{CT}} \equiv k_2 n_{\mathrm{CS}}^2, \tag{7.58}$$

where R is the total recombination rate of the re-formed singlet and triplet CT states. In general, k_2 can be related to the free charge encounter coefficient via $k_2 = \gamma_{CT} k_{en}$, yielding

$$k_2 = \gamma_{CT}\gamma_{en}k_L = \gamma k_L, \tag{7.59}$$

where γ_{CT} is the CT recombination reduction factor and $\gamma = \gamma_{CT}\gamma_{en}$ is the bimolecular recombination reduction factor.

Now let's consider different conditions of CT state kinetics with the corresponding state diagram shown in Figure 7.1.

a) $k_d \ll k_f$ and k_{BET}

When CTS dissociation is much slower than the two loss rates (a very poor generation efficiency), the total recombination rate is entirely encounter limited and given by:

$$R = k_2 n_{\mathrm{cs}}^2 = k_{\mathrm{en}} n_{\mathrm{cs}}^2 = \gamma_{\mathrm{en}} k_L n_{\mathrm{cs}}^2. \tag{7.60}$$

In such case the total reduction factor relative to the Langevin rate is $\gamma = \gamma_{\mathrm{en}}$, merely due to the geometrical confinement of the electrons and holes in their respective domains. It has been shown based on Monte Carlo simulations that in BHJ solar cells with domain sizes of less than 10 nm this geometrical reduction can never be significant.[196]

b) Fast intersystem crossing and dissociation rates: $k_{\mathrm{ISC}} >> k_{\mathrm{BET}}$ and $k_d \gg k_f$, $k_{\mathrm{d}} >> k_{\mathrm{BET}}$

When the dissociation rate of CT states is much faster than the decay rate of ^{1}CT and back electron transfer rate of ^{3}CT, the CT states are in equilibrium with free carriers i.e., the chemical potential of the CT states equals the quasi Fermi level splitting of the electrons and holes. The same scenario can happen even if k_d is not necessarily faster than k_{BET} but the intersystem crossing for ^{3}CT-^{1}CT is very fast ($k_{ISC} \gg k_{BET}$). This will depopulate the triplet CT states and the kinetics is similar to the case that spin is neglected.

In this case of fast dissociation rate, one can write

$$k_{\mathrm{en}} n_{\mathrm{CS}}^2 = k_d n_{CT} \tag{7.61}$$

where $n_{CT} = n_{1CT}$ due to ISC from ^{3}CT to ^{1}CT. Then recombination rate is

$$R = k_2 n_{\mathrm{CS}}^2 = k_f n_{\mathrm{CT}} = \frac{k_f}{k_d + k_f} k_{\mathrm{en}} n_{\mathrm{CS}}^2 = \gamma_{\mathrm{CT}} \gamma_{\mathrm{en}} k_L n_{\mathrm{CS}}^2 \quad (7.62)$$

where we used the geometrically reduced encounter rate $k_{\mathrm{en}} = \gamma_{\mathrm{en}} k_L$. In the limiting case of very small domain size $\gamma_{\mathrm{en}} \approx 1$, the reduction factor is

$$\gamma = \gamma_{\mathrm{CT}} = \frac{k_f}{k_d + k_f}. \quad (7.63)$$

Thereby, one can deduce a reverse correlation between generation efficiency (Equation 7.53) for steady state recombination.

$$\gamma_{\mathrm{CT}} = 1 - \eta_{\mathrm{diss,CT}}, \quad (7.64)$$

where $\eta_{\mathrm{diss,CT}} = \frac{k_d}{k_d + k_f}$ (Equation 7.53) is the efficiency of CT dissociation into free charges.

c) Slow intersystem crossing and fast dissociation rates: $k_d \gg k_f$ and $k_d \gg k_{BET}$

In this section we consider the general case in which upon recombination of free carriers to CT states, a 1:3 ratio of singlet:triplet CTS is maintained. This is expressed as

$$k_{\mathrm{en}} n_{\mathrm{CS}}^2 = k_d (n_{1\mathrm{CT}} + n_{3\mathrm{CT}}) \quad (7.65)$$

and the recombination rate is given by:

$$R = k_2 n_{\mathrm{CS}}^2 = k_f n_{1\mathrm{CT}} + k_{\mathrm{BET}} n_{3\mathrm{CT}} = \frac{k_f}{k_d + k_f} k_{\mathrm{en}} n_{\mathrm{CS}}^2 = \gamma_{\mathrm{CT}} \gamma_{\mathrm{en}} k_L n_{\mathrm{CS}}^2 \quad (7.66)$$

where

$$\gamma_{\mathrm{CT}} = \frac{\rho k_f}{\rho k_f + k_d}, \quad (7.67)$$

in which

$$\rho = \frac{1}{4} + \frac{3}{4} \frac{k_{\mathrm{BET}}}{k_f}. \quad (7.68)$$

We label parameter ρ as "spin-related factor" which plays an important role in defining the regime of bimolecular recombination. When $k_{\mathrm{BET}} = k_f$ ($\rho = 1$), the singlet and triplet states have the same loss kinetics and thereby "undisguisable" in terms of their decay rate to the environment. In this regime, Equation (7.67) is reduced to Equation (7.63) in which the role of spin is ignored. When $k_{\mathrm{BET}} \ll k_f$, $\rho = \frac{1}{4}$ and γ_{CT} will be defined by the ratio k_f/k_d, however 4 times less than what is predicted when spin is neglected. When $k_{\mathrm{BET}} \gg k_f$, ρ diverges and γ_{CT} will be dependent on the ratio of $\rho k_f/k_d$ and approaching to 1 if $\rho k_f \gg k_d$.

Similar to Equation 7.64 we obtain an expression between reduction factor and charge generation efficiency but now taking spin into account

$$\gamma_{CT} = \frac{\rho(1-\eta_{diss,CT})}{\rho(1-\eta_{diss,CT})+\eta_{diss,CT}}, \tag{7.69}$$

which yields equation 7.64 when ρ =1.

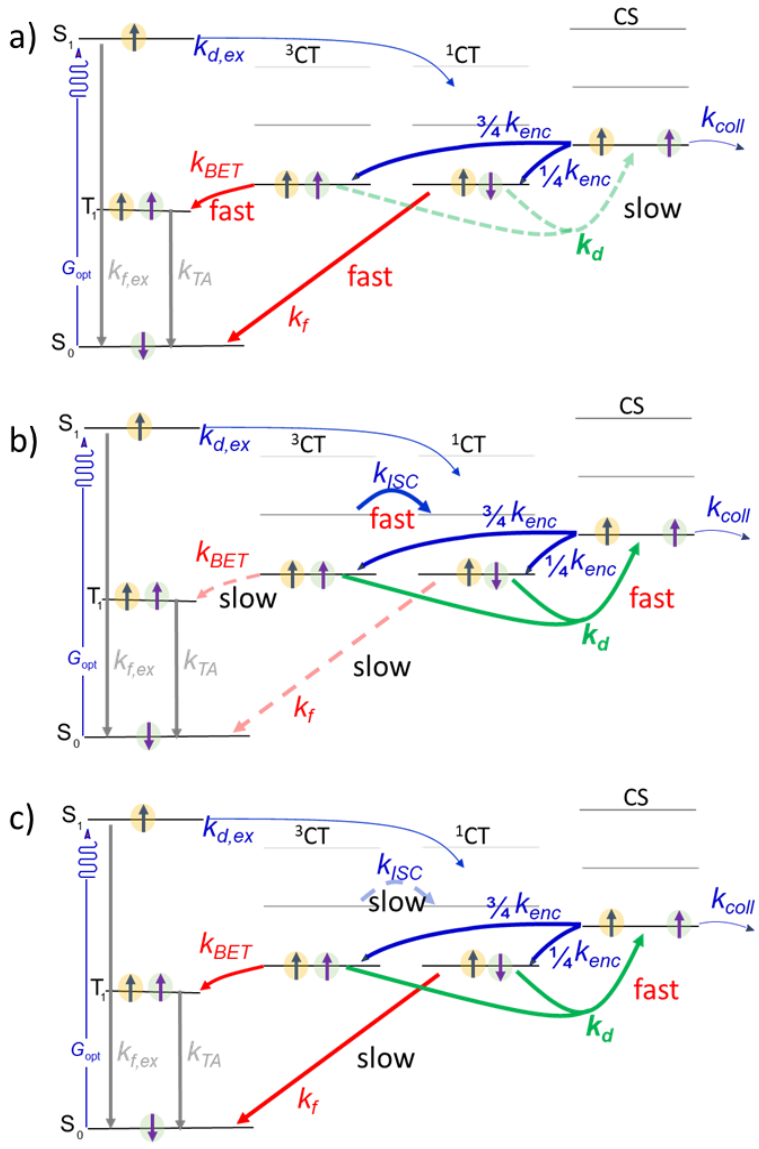

Figure 7.1 State diagram of the BHJ solar cells for the three different conditions of the CT state when: a) poor charge generation b) fast intersystem crossing and dissociation rates and c) slow intersystem crossing and fast dissociation rates. The two main loss pathways of the CT states to the ground states are the decay of singlet CT states at the rate k_f to the ground state and the loss of the triplet CT states through back electron transfer to triplet excitons at rate k_{BET}.

7.2 Experimental results

We now turn to consideration of experimental data on the extent to which the proposed variation in reduced recombination can be correlated with variations in charge generation efficiency. In this regard we present a large amount of published and unpublished data from our own group and others, of over 20 systems (chemical structures shown in schematic 1) where field-dependent charge generation efficiency, recombination coefficient and mobilities have been measured. Importantly these systems are mostly characterised with same techniques, minimising technique-related variations. Device performance characteristics are listed in Tables 1 and 2 (with exemplary TDCF and BACE data for NT:ITIC and NTPCBM given in the SI). Figure 7.2 shows *JV* curves for two model systems with and without a gradient of charge generation at short circuit under simulated 100 mWcm^{-2} AM1.5 illumination, along with the external generation efficiency (EGE) obtained from time delayed collection field (TDCF) measurements, as described elsewhere.[81,203] As can be observed, both *JV* curves are well described by the estimated EGE at reverse bias, where recombination is reduced by the effect of the applied field. It is also evident that, whereas for the device with a gradient *JV* the effect of bias on generation is relatively large (EGE decreases by 25% from -2 to V_{OC}), compared to the effect of the electric field on the EGE is very small in the other device (<5%). Generally, the EGE is determined in these systems as a function voltage can be written as

$$\mathrm{EGE}(V) = \mathrm{IGE}(V) \times \eta_{\mathrm{abs}} = \eta_{\mathrm{diss.ex}}\eta_{\mathrm{dissCT}}(V)\eta_{\mathrm{abs}} \tag{7.70}$$

in which IGE is the internal generation efficiency, η_{dissex} the exciton quenching yield, and η_{abs} absorption of the active layer. The latter two are nearly independent of the applied voltage.

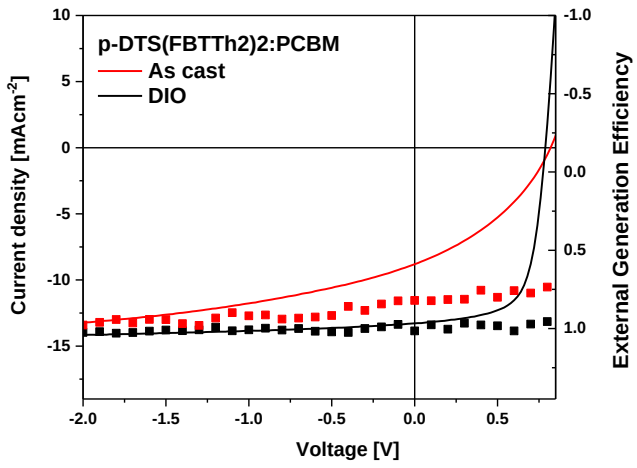

Figure 7.2. The external generation efficiency (EGE) and current density-voltage characteristics under simulated AM 1.5 G light calibrated to 100 mW cm^{-2} data reproduced from [190].

In order to estimate $\eta_{\mathrm{diss,CT}}(V_{\mathrm{OC}})$ at open circuit condition [relevant Equations (7.64) and (7.69)], we normalised experimentally determined external charge generation efficiency at V_{OC} against the EGE at -2V at which in most cases a saturated photocurrent and EGE is achieved:

$$\eta_{\mathrm{diss,CT}}(V_{\mathrm{OC}}) = \frac{\mathrm{EGE}(V_{\mathrm{OC}})}{\mathrm{EGE}(J_{sat})}. \tag{7.71}$$

This normalisation ensures that imperfect exciton quenching, light reflection and parasitic absorption by non-active layers are ruled out and $\eta_{\mathrm{diss,CT}}(V_{\mathrm{oc}})$ is a direct indicator of efficiency of dissociation of initially generated interfacial polaron pairs into dissociated charges.

To relate the efficiency of charge generation at V_{OC} to recombination, we employed steady state bias assisted charge extraction to measure the recombination rate k_2 under steady state illumination at V_{OC}. Furthermore, the carrier mobility for each system has also been measured - under device operational conditions when carriers have thermalized - in order to calculate k_{L}; all values are presented in Table 7.2. Figure 7.3 shows the correlation between this assay of $\eta_{\mathrm{diss,CT}}$ and reduced recombination of free carriers, as presented in Equation (7.64). The reduction factor γ was estimated from dividing the experimentally measured bimolecular recombination rate constant by the inferred Langevin rate from experimentally measured electron and hole mobilities.

For all systems presented in Figure 7.3, a good correlation is observed between $\eta_{\mathrm{diss,CT}}$ and its corresponding bimolecular recombination reduction factor; whereby we observe the reduction factor decreasing (recombination becoming slower) with increasing charge generation efficiency. When charge generation is field independent ($\eta_{\mathrm{diss,CT}} > 95\%$), strongly reduced recombination is heuristically achieved. However, at lower $\eta_{\mathrm{diss,CT}}$ when the charge generation is field dependent, pointing to a small dissociation rate k_{d}, encounter limited recombination or very modestly reduced recombination is observed, as predicted by Equation (7.69). On the other hand, there are some systems which have a quite efficient generation however with a fairly large γ, implying recombination proceeds mostly through back electron transfer. The dashed lines on Figure 7.3 show Equation (7.69) for different values of ρ. Most systems lie on $\rho = 0.4 - 1$ suggesting a k_{BET}/k_f ratio between 0.2 and 1.0 respectively. The most efficient system with strongly reduced recombination has $\rho = 0.25$ indicating negligible back electron transfer.

This model showcases the importance of suppressing triplet loss channel to achieve reduced recombination and efficient charge generation. Notably, none of the data points lie below the $\rho = 0.25$ line. As $\gamma = \gamma_{CT}\gamma_{en}$ refers to the Langevin recombination rate, the absence of data points below this lines implies that reduced recombination stems almost entirely from the dissociation of re-formed CT states (expressed by γ_{CT}<1), and that reduced encounter rate of free carries plays an insignificant role in the reduction of bimolecular recombination ($i.e, \gamma_{\text{en}} \cong$ 1) in most of the studied blends.

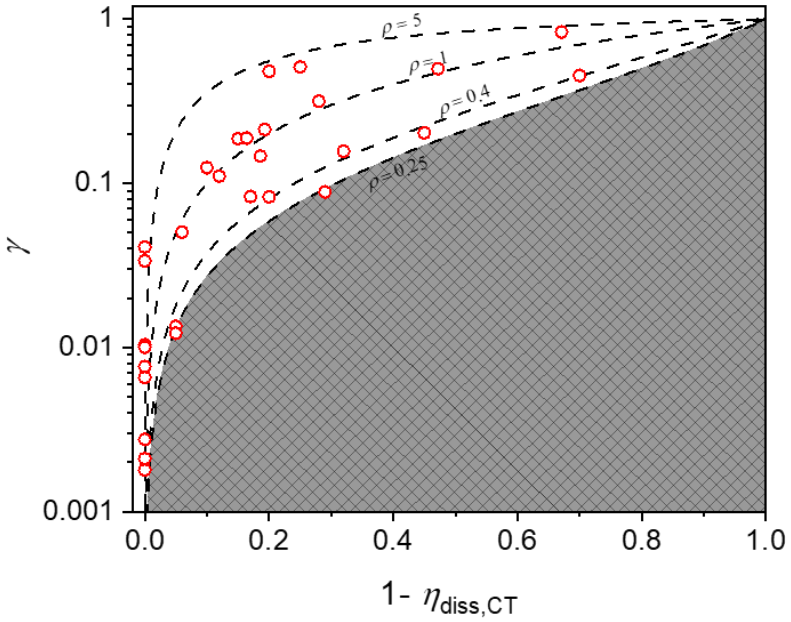

Figure 7.3 Correlation of data from Table 1 between γ (bimolecular recombination reduction factor) and the CT state dissociation efficiency, $\eta_{\text{diss,CT}}$ under operational conditions. The dashed lines represent Equation (7.69) for different values of the spin-related factor ρ. The absence of data points below ρ=0.25 line indicates that geometrical confinement plays no role in the suppression of bimolecular recombination so that γ= γ_{CT} in the 24 systems studied herein.

7.3 Limitations and outlook of the model

Our model represents a general frame for the relationship between charge generation and the Langevin reduction factor, which has the assumption that rate of dissociation of the CT state formed through photogenerated carriers and that formed due to the encountering of free carriers through space, are proportional. The model should be refined for system in which hot CT state or delocalization determines the rate of photogenerated CT state dissociation involving charge generation. Yet, this should only affect the systems with high charge generation efficiency.

Additional shortcoming of our model comes from the experimental limitation in determining the exact charge generation yield in systems with nearly unity quantum yields. This is not only a limitation of the methodology we employed but a problem that the community has not yet overcome: how to detect near unity charge generation quantum yield. The technical limitation is mainly due to the variations in the TDCF data versus the voltage which arises from laser fluctuations and uncertainty of the extracted charges evaluated by integration of the current transients as well as very precise determination of the number of photons. As such, our experimental methodology is not able to quantitatively explain systems above 99% quantum yield. However, and given this limitation, even in these systems the expected trend as shown by the dashed lines in Figure 7.3 is still observable, that is, the larger the charge generation quantum yields the smaller the reduction factor.

7.4 Interrelation between the efficiency of CT dissociation and the fill factor

We now turn to the consideration of the FF by focusing on the same material systems as above. FF is a sensitive parameter as it summarizes all field-dependent processes. As such, it depends on the CT dissociation efficiency, the electron and hole mobility, the recombination coefficient, but also the thickness of the active layer. For high mobility materials, the current voltage characteristics is given by the Shockley diode equation and the FF is a sole function of the V_{oc}, the ideality factor and the temperature. Recently Neher et al., reported a modified Shockley equation, which takes into account transport limitations in organic solar cells due to low mobilities.[44] If free charge generation is independent of bias, the model also allows to predict the FF from a unit-less parameter $\alpha = \left(\frac{qk_2d^3J_G}{4\mu_h\mu_e(kT)^2}\right)^{1/2}$, which contains information on the transport and recombination properties of the active layer such that d is the active layer thickness, k the Botlzmann constant, T the absolute temperature and J_G is the generation current. Here we have evaluated the generation current from the saturated photocurrent. Figure 7.4a demonstrates the experimentally determined FFs at AM1.5G illumination for various systems as a function of α, based upon the modified Shockley equation (the black rectangles). Also plotted on the same figure is the calculated values of the FF for each system based on the approach presented by Neher et al.[44] (red circles) figure of merit model. Although the model predicts the overall FF trend, there is a large spread observed in the experimental FF data. In particular, the prediction overestimates the FF for systems exhibiting field dependent charge generation, which is reasonable since the model neglects any field-dependence of free charge generation. However, recent studies reported voltage-dependent charge photogeneration in BHJ solar cells and discussed the impact of this on the device FF.[87,204] In fact, several of the blend

systems in Table 1 reveal field dependent charge generation. In this regard, we correct the measured FF data to take account of the variations in field dependence by defining

$$FF_{corrected} = \frac{FF - FF_0(1-EGE)}{EGE}, \tag{7.72}$$

where FF is the measured value and FF_0 is a value which would correspond to a linear JV profile in the power generating quadrant (i.e. FF = 0.25): in the limiting case of poor charge generation, photocurrent is determined by the field dependence of generation, which is assumed to be linearly dependent on voltage. On the other hand, when charge generation is field independent (EGE =1), $FF_{corrected}$ = FF. As such by correcting the measured FF values by the field dependent charge generation efficiency (equation (7.72)) to yield the upper limit for FF, as shown in Figure 7.4b, we observe a better agreement between the calculated and the measured values (corrected for field dependence). For each system, the FF predicted by the model of Neher et al (red rectangles in Figure 7.4) is the upper limit of the FF which could be achieved if the charge generation for that given system was independent of the electric field. The remaining data spread can be due to series and shunt resistances, which are not considered in the model.

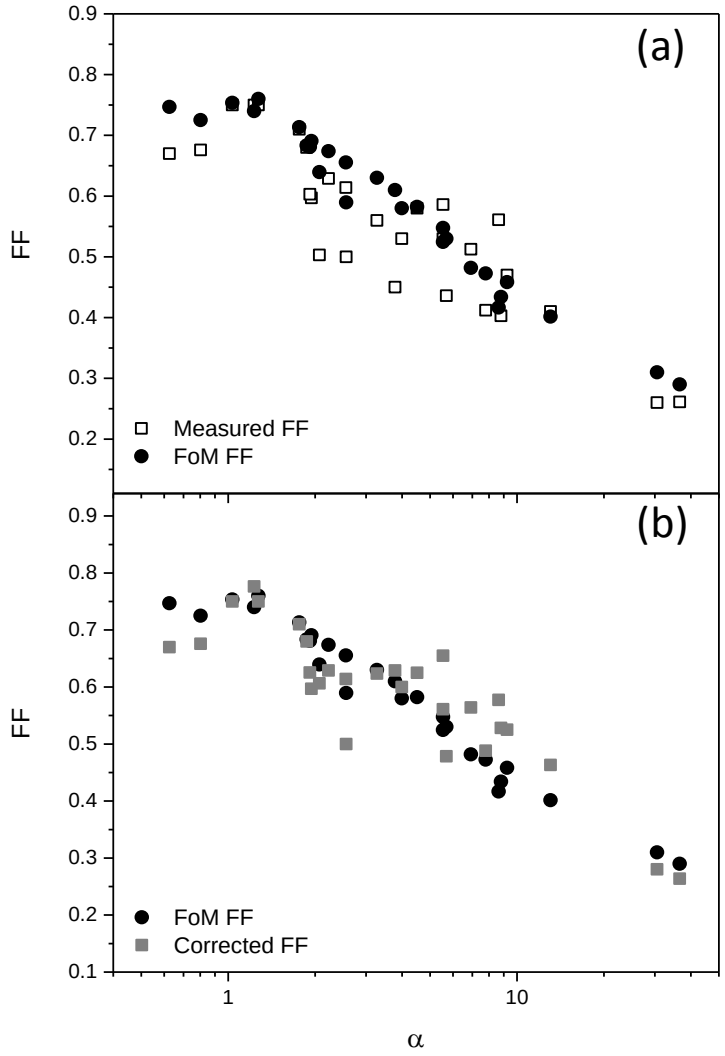

Figure 7.4. Theoretically predicted FF as a function of alpha based upon the modified Shockley diode equation given in the citation [9] together with (a) experimentally measured FFs (b) the measured FF from a, normalised for field dependent charge generation.

Following the discussions above, when k_d is large enough already at zero field, and consequently the CT splitting proceeds at a higher rate than their recombination, it results in a very efficient charge generation quantum yield even under open circuit condition. Thereby field independent efficient charge generation is expected. Thus it is clear that within this model, a key kinetic competition in achieving high FF is between the dissociation of CT state and the loss decays of the CT states (when $k_d >> k_f + k_{BET}$). This emphasise the importance and influence of field dependent charge generation on FF; in systems where charge collection is inefficient due to significant recombination (encountered limited), the FF is not only governed by the direct field dependence of the first-order charge generation but also competition between

charge extraction and bimolecular recombination due to the lower dissociation rate of CT state which itself also causes a field dependent charge generation.

7.5 Experimental section/Methods

Solar cell devices fabrication

Most data points used in this study are taken from previous published works. Few new systems are also used including NT812:PCBM[70], NT812:ITIC, MEH:PPV, P3HT:PCBM and PTB7:PCBM[70]. For these systems, prepatterned indium tin oxide (ITO)-glass substrates were pre-cleaned successively with detergent, acetone, de-ionized (DI) water and IPA and dried by nitrogen. The dried substrates were treated by oxygen plasma at room temperature for 4 min and then coated with PEDOT:PSS by spin-coating (3000 r.p.m. for 30 s, thickness of ≈40 nm) and were then baked at 150 °C for 15 min in air. For deposition of active layers, blend solution of polymer (NT812 with polydispersity index, PDI≈2) with PCBM[70] or ITIC at different weight ratios were dissolved in CB:DCB = 3:1 (with 0.5 vol% of 1-chloronaphthalene) and blend solution of polymer:ITIC at different weight ratio were dissolved in o-xylene (with 1 vol% of 1-Methyl-2-pyrrolidinone) and were spin-coated on top of the PEDOT:PSS layer in a nitrogen-filled glove box. Typically an active layer of 100 nm thickness can be achieved using a polymer concertation of 4 and 9 mg mL^{-1} for NT812:PCBM[70] and NT812:ITIC, respectively. Thermal annealing of the blend films was carried out by placing the films on a hot plate at 100 °C for 15 min and 160 °C for 20 min for NT812:PCBM[70] and NT812:ITIC, respectively, in a nitrogen atmosphere. A 5 nm PFN-Br layer was then spin-coated from methanol solution onto the active layers.

To fabricate the PTB-7:PCBM active layers, PTB-7 and PCBM were separately dissolved in DIO:chlorobenzene (3:97 vol%) and then mixed to different blend ratios (by weight) solution with a total concentration of 25 g L^{-1} and subsequently spin coated at 1000 rpm, yielding an active layer thickness of 100 nm.

For the P3HT:PC60BM devices, 30 mg of PC60BM was dissolved in 1 mL of DCB at 70 °C and then stirred at room temperature overnight. The PC60BM solution was then filtered before adding 30 mg of P3HT and the final mixture was left on the hot plate at 70 °C for 1 h. The blend solution was spin-coated once it had cooled down to room temperature within ~15 min. 90 nm thick films were deposited by spin-coating 15 mg/mL solutions at 600 rpm, and subject to solvent annealing over night. After top electrode evaporation the device was thermally annealed for 2 minutes at 170 °C.

The blend of MEH-PPV:PCBM (1:4 by weight ratio with a total concentration of 25 mg) in chlorobenzene solution was spin-coated at 800 rpm for 50 s, yielding an active layer thickness of 100 nm.

The thin films were transferred into a vacuum evaporator connected to the glove box, and Ag (100 nm for the NT812 devices), Al (100 nm for P3HT:PCBM) and LiF/Al (0.8 nm and 100 nm for MEH-PPV) was deposited sequentially through a shadow mask under $\approx 1 \times 10^{-7}$ mbar, with an active area of the cells of A = 0.011 cm^2 for BACE and TDCF measurements, and A = 0.06 cm^2 for JV measurement.

UV-Visible absorption and Photoluminescence (PL) spectroscopy

UV-Visible spectra of the thin films were acquired with Cary 5000 UV-Vis-NIR spectrophotometer in air. The PL spectra were measured with a Fluorolog-3 spectrofluorometer (Horiba Jobin Yvon). All film samples were spin coated on glass substrates. The UV/Vis and PL were used to determine excitation wavelengths as well as documenting the crude morphology as reflect in absorption and photoluminescence.

Time Delayed Collection Field (TDCF)

In the TDCF experiment, a laser pulse from a diode pumped, Q-switched Nd:YAG laser (NT242, EKSPLA) with 6 ns pulse duration and a typical repetition rate of 500 Hz working at 532 nm were used to generate charges in the device. A pulse generator (Agilent 81150A) was used to apply the pre- and collection bias which are amplified by a home-built amplifier. The current through the device was measured via a grounded 10 Ω resistor in series with the sample and with a differential current probe recorded with an oscilloscope (DSO9104H). The pulse generator was triggered with a fast photodiode (EOT, ET-2030TTL). The fluence was determined with a CCD-camera in combination with a calibrated photodiode sensor (Ophir) and a laser-cut high-precision shadow mask to define the illuminated area.

Bias Assisted Charge Extraction (BACE)

The experimental setup required for BACE measurements was similar to the TDCF setup, except for the illumination conditions. The steady state condition was established by a high power 1 W, 638 nm laser diode (insaneware) with a switch off time of about 10 ns. The LED was operated at 500 Hz with a duty cycle of at least 50% of one period, which means 1ms of illumination before the diode was switched off for 1 ms. After switching off the laser diode, a high reverse bias was applied and all charges were extracted. The fast switch off time of the diode and the fast pulse generator (Agilent 81150A) allowed for charge extraction as fast as 10–20 ns after the switch off. The current transients were measured via a grounded 10 Ω resistor and recorded with an oscilloscope (DSO9104H) in the same way as for the TDCF measurement.

Resistance dependent PhotoVoltage (RPV)

Photocurrent and photovoltage transients were recorded using a digital storage oscilloscope (DSO9104H) via a LabVIEW code. A pulsed second-harmonic Nd:YAG laser (NT242, EKSPLA) working at 450 nm was used with 6 ns pulse duration. The laser beam with ~50 mJ energy output was attenuated with a natural optical-density (OD) filter set. Low laser pulse fluences (~OD 7) were used for the RPV mobility measurements in order to prevent a redistribution (screening) of the internal electric field and maintaining quasi-short-circuit conditions regardless of the load resistance.

Space Charge Limited Current (SCLC)

Electrical measurements were carried out on devices fabricated using ITO /PEDOT:PSS /active layer /MoO_3 /Au for hole only and ITO /Ca /active layer /PFN /Al for electron only devices with NT812:PCBM[70] and NT812:ITIC as the BHJ active layers.

7.6 Conclusion

In conclusion, we have investigated the generality of previously hypothesized explanation on reduced recombination for numerous different systems and have shown for the first time correlations between field dependent charge generation efficiency and reduction of bimolecular recombination, taking into account the effect of spin. We introduced a 'spin related factor' which quantifies the kinetics of singlet and triplet CT states. The results reported in this paper provides strong evidence that a key factor determining bimolecular recombination efficiency of photogenerated carriers and the fill factor, is the efficiency of charge generation, where the key kinetic competition in suppressing the recombination is between dissociation of CT state and the loss decays of the CT states such that that charge-neutral molecules in their ground state are restored. The experimental data is rationalised by appreciating how the CT state mediates the interplay between charge generation and bimolecular recombination. Our results also indicated that the geometric confinement of the holes in the donor domains and electrons in acceptor domains plays insignificant role in the suppression of bimolecular recombination. In addition, we have shown that the FF can suffer from inefficient generation in two ways: 1) charge generation itself being field dependent and subsequently 2) poor generation efficiency (i.e. field dependent) causes a less suppressed bimolecular recombination, therefore a higher k_2. Our results indicate that in order to reduce bimolecular recombination significantly with respect to the diffusion limited encounter rate of the charge carriers, and achieve FF close to the upper theoretical limit, one needs to suppress the loss channels from both singlet and triplet CT states simultaneously. This can be elegantly achieved by increasing the CT state's dissociation rate to

free carriers and obtaining field independent generation efficiencies of 100%. Whilst the origin of this rate concept is beyond the scope of this paper, we anticipate crystallinity, domain purity and effectively local mobility play important roles in determining the rate of k_d.

8. Summary, Conclusion and Outlook

The work described in this thesis was mainly focused on understanding the free charge carrier recombination dynamics in OSCs. The research can be divided into four parts:

In the first part of this thesis, I compared a fullerene acceptor named, PCBM[70] with a NFA named ITIC when they are combined with a donor polymer, named NT812. Our results have shown a higher J_{SC} and V_{OC} in the NFA device, compared with the fullerene device, which mainly originates from the complementary absorption between donor and NFA, and the lower LUMO-LUMO energy offset, respectively. However, the PCE of the NFA device was suppressed by the modest FF in this device. To elucidate the reason behind it, field-dependent charge generation and recombination dynamics have been studied via TDCF and BACE techniques. Our results have shown that the low FF in the NFA device comes from the fast time-dependent bimolecular recombination whilst the fullerene blend exhibits reduced-Langevin recombination. It was shown that the reduced recombination cannot be explained by morphology alone, rather we suggested the reason behind having a higher reduction factor in the fullerene device may originate from the favorable kinetics of the CT state; in contrast, in the case of the ITIC system, the recombination rate is mostly encounter limited.

In the second part of this work, I focused to study an NFA, named Y6 which at the time achieved a PCE above 15% when blended with PM6 polymer as a donor. Our results have illustrated that by increasing the active layer thickness of PM6:Y6, the FF reduces; however, the J_{SC} and V_{OC} remain almost constant. To demonstrate the reason behind this phenomenon, charge extraction (via T-SCLC technique), bimolecular recombination (via BACE technique), and morphology (via GIWAXS technique) of thin and thick PM6:Y6 devices were studied. Our data have shown that by increasing the active layer thickness of PM6:Y6, the energetic and structural disorders of hole transport increase, as well the ratio between electron and hole mobility start to deviate. Drift-Diffusion simulation of *JV* characteristics revealed that the thick PM6:Y6 device has the potential to obtain a higher PCE via simultaneously enhancing the hole mobility and reducing the bimolecular recombination. Experimentally, this approach was achieved by tuning the morphology and order of the thick device via optimizing the concentration of the solvent additive in the solution. As a result, I succeeded to improve the PCE of thick PM6:Y6 from 12.2% to 14.4%, by enhancing the FF from 58% to 68%. GIWAX and T-SCLC data reveal that the optimized thick device has a more phase-separated morphology, an improved crystallinity of the individual domains, and lower HOMO/LUMO energetic disorders. The results indicate

that optimizing the solvent additive content reduces the energetic and structural disorders and enhanced both electron and hole mobilities toward balancing. Simultaneously, a reduction in the bimolecular recombination coefficient of free carriers was measured, with a reduction factor of 180 times. This achievement sheds new light on the role of energetic disorder on the recombination mechanism of NFA based OSCs.

The reason behind the invariant J_{SC} with increasing the active layer thickness of PM6:Y6 has been studied in the third part of this thesis. Mott-Schokley analysis through impedance measurement enabled to estimate the width of the depletion region; 85 nm for the 100 nm junction device and 170 nm for the 300 nm junction device. This suggests that a significant part of the active layer in the thick device remains in the flat-band condition. Therefore, an inefficient collection of charges generated in the flat-field part of the cell outside the high-field depletion region is expected. However, the J_{SC} of the thick device is still efficient compared with the thin device. The diffusion length of both carriers was calculated by measuring the mobilities (via SCLC technique) and carrier recombination lifetime (via PIA technique). The data shows that the electron and hole diffusion lengths - in the thick device - are estimated to be 330 nm and 70 nm, respectively. Thus it can be concluded that the rather high estimated electron diffusion length in the thick PM6:Y6 device may provide an explanation to the observed high J_{SC} value.

In the last part of this thesis, we established a model to describe the role of the kinetics of singlet and triplet CT states in suppressing the recombination. In this model, we introduced a 'spin-related factor' which quantifies the kinetics of singlet and triplet CT states. Our results indicated that the geometric confinement of the holes in the donor domains and electrons in acceptor domains plays an insignificant role in the suppression of bimolecular recombination. On the other hand, the suppression of the loss channels from both singlet and triplet CT states, significantly, reduces the bimolecular recombination, achieving a FF close to the upper theoretical limit.

The results from this thesis provided important ideas about FF which is crucial for further optimization of OSCs. In particular, the drop in FF for NFA devices has been investigated. Our data show that the drop in the FF for NFA (based-ITIC) devices is due to faster time-dependent non-geminate recombination relative to the fullerene (PCBM[70]-based) devices. We illustrated that slowing down the non-geminate recombination, to shift the balance toward non-Langevin systems, is important for both improving the FF and achieving thick junction devices.

Following this study, we investigated the role of disorder on non-geminate recombination of thick NFA (Y6-based) devices. Such that reducing the energetic disorder and putting order into thick PM6:Y6 devices suppresses the non-geminate recombination. Consequently, we succeeded to improve the FF of thick PM6:Y6 by manipulating the energetic and structural disorder (which causes 180 times reduction toward non-Langevin system) through tuning the morphology. In addition, thickness dependence of photocurrent in PM6:Y6 was studied. Our investigation shows that the extraordinarily long diffusion length of Y6 tackles the thickness independence of the short circuit current in this system. This sheds new light on the fabrication of efficient, high-photocurrent, thick OSCs. Finally, by studying a broad selection of fullerene and non-fullerene blends, we illustrated that to achieve FF close to the upper theoretical limit through reducing the non-geminate recombination with respect to the diffusion-limited encounter rate of the charge carriers, one needs to suppress the loss channels from both singlet and triplet CT states simultaneously. This can be achieved by increasing the CT state's dissociation rate to free carriers and obtaining field-independent generation efficiencies of 100%.

As an outlook, our studies thoroughly investigated the importance and impact of charge recombination and energetic disorder on the FF of NFA devices. Such that playing down the charge recombination and putting structural order into NFA devices lead to enhance the PCE, through improving the FF. Therefore, subsequent developments would most obviously focus on strengthening the conclusions around the relationships between these two factors.

Appendix

A.1 Non-Radiative Voltage Loss Calculation

The V_{OC} limited by the radiative recombination is given by:

$$V_{OC,rad} = \frac{k_B T}{e} \ln\left(\frac{J_{sc}}{J_{0,rad}} + 1\right) \quad \text{(A.1)}$$

On the other hand, the measured V_{OC} is expressed by:

$$V_{OC} = \frac{k_B T}{e} \ln\left(\frac{J_{sc}}{J_0} + 1\right) \quad \text{(A.2)}$$

where J_0 is defined by (according to the detailed balance principle by Rau[73]):

$$J_0 = \frac{e}{EQE_{EL}} \int_{Eg}^{\infty} EQE_{PV}(E).\varphi_{BB}(E).dE \quad \text{(A.3)}$$

by using equations 27, 28, and A.3 into equations A.1 and A.2, we can get the non-radiative voltage loss:

$$V_{OC,rad} - V_{OC} = \frac{k_B T}{e} ln\left(\frac{\int_{Eg}^{\infty} EQE_{PV}(E).\varphi_{sun}(E).dE}{\int_{Eg}^{\infty} EQE_{PV}(E).\varphi_{BB}(E).dE}\right) - \frac{k_B T}{e} ln\left(\frac{\int_{Eg}^{\infty} EQE_{PV}(E).\varphi_{sun}(E).dE}{\int_{Eg}^{\infty} EQE_{PV}(E).\varphi_{BB}(E).dE} \times EQE_{EL}\right) =$$

$$\frac{k_B T}{e} \ln(EQE_{EL}) \quad \text{(A.4)}$$

A.2 Calibration for Absolute EL Measurements

The radiant flux Φ_0 into a solid angle increment dΩ is given by:

$$\Phi_0 = \int_0^{2\pi} d\varphi \int_0^{\theta_0} I(\theta) \sin(\theta)\, d\theta \quad \text{(A.5)}$$

according to Lambert's law,

$$I(\theta) = I \cos(\theta) \quad \text{(A.6).}$$

After calculating the integral,

$$\Phi_0 = \pi I \, sin^2(\theta_0) \quad \text{(A.7)}$$

as shown in Figure A.1, $\sin(\theta_0)$ is:

$$\sin(\theta_0) = \frac{\sqrt{a^2+R^2}}{R} \quad \text{(A.8)}$$

where a is the distance between the silicon detector and the device and R is the radius of the silicon detector (which is 5.642mm). On the other hand, the total radiant flux is:

$$\Phi_{total} = I\pi \quad \text{(A.9).}$$

The output of the calibrated silicon detector is current (i_m), and the total current (i_{total}) which is related to the whole sphere is expressed by:

$$\frac{i_{total}}{i_m} = \frac{\Phi_{total}}{\Phi_0} = \frac{I\pi}{I\pi\frac{\sqrt{a^2+R^2}}{R}} \quad \text{(A.10).}$$

In order to determine the total current, the distance between the silicon detector and the device needs to be measured precisely; therefore, the device was mounted on top of a portable micrometer stage and the measurement was done three times with three different distances so

that $a = r_0 + r_i$, where r_0 is the initial distance and r_i is the movement by a micrometer. In this regard, the total current should be the same for each distances; consequently, a is determined accurately. Finally, the total current is calculated by:

$$i_{total}=i_m \cdot (\frac{\sqrt{(r_0+r_i)^2+R^2}}{R})^2 \quad \text{(A.11).}$$

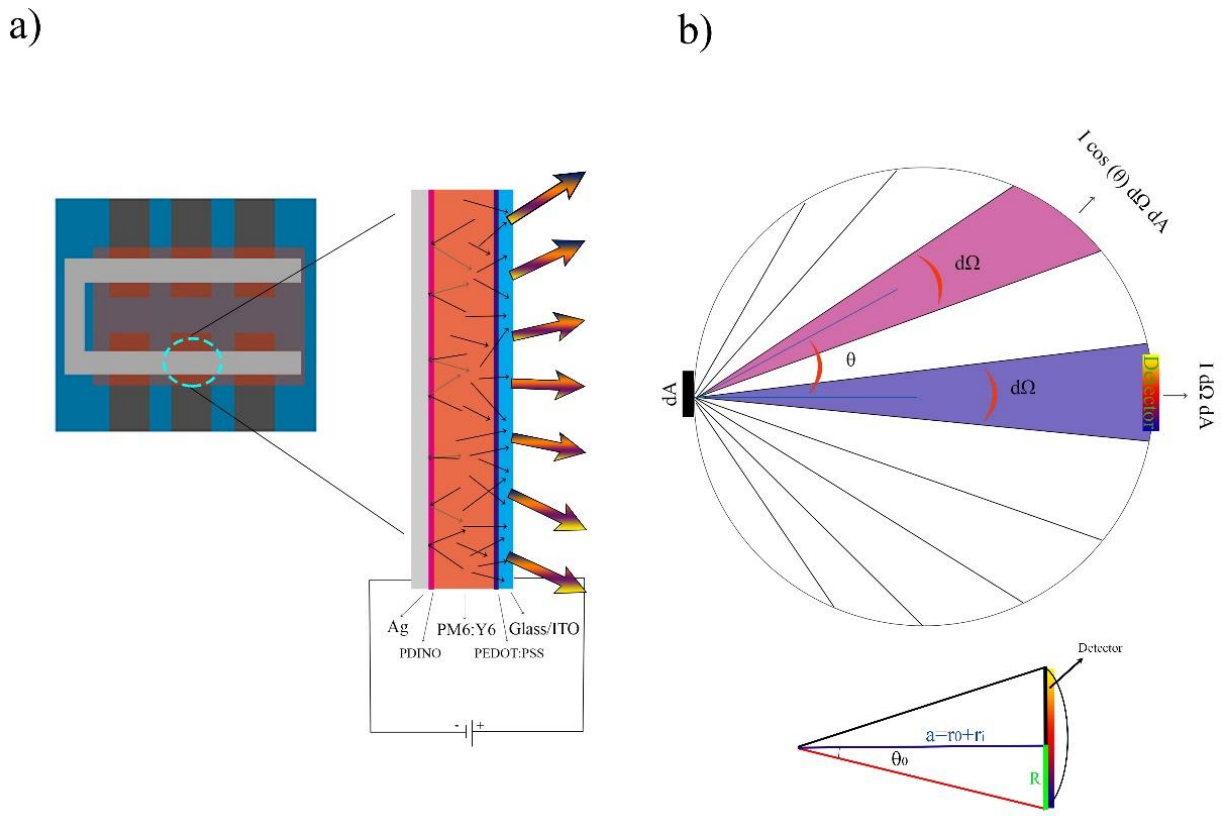

Figure A.1. a) Sketched picture of the OSC (e.g. PM6:Y6) emitting in a normal and off-normal directions. b) OSC is assumed as a Lambert's emitter which is shown by dA and the calibrated silicon detector is mounted in front of it in order to determine the number of emitted photons.

Biography

(1) Renewables 2020 global status report, 2020. https://www.ren21.net/wp-content/uploads/2019/05/gsr_2020_full_report_en.pdf (accessed Jun 1, 2021).

(2) BP Statistical Review of World Energy, 2021. https://www.bp.com/ (accessed Jun 1, 2021).

(3) Becquerel, M. E. Mémoire Sur Les Effets Électriques Produits Sous l'influence Des Rayons Solaires. *C. R. Hebd. Seances Acad. Sci.* **1839**, *9*, 561–567.

(4) Pochettino, A.; Sella, A. Photoelectric Behavior of Anthracene. *Acad. Lincei Rend* **1906**, *15*, 355–363.

(5) Pope, M.; KMlmann, H. P. Mag~ Ante P J. *Chem. Phys* **1963**, *38*, 2042-2O43.

(6) Pope, M.; Swenberg, C. E. *Electronic Processes in Organic Crystals and Polymers*; Oxford University Press on Demand, 1999.

(7) Tang, C. W.; Albrecht, A. C. Photovoltaic Effects of Metal–Chlorophyll-a–Metal Sandwich Cells. *J. Chem. Phys.* **1975**, *62* (6), 2139–2149.

(8) Tang, C. W. Two-layer Organic Photovoltaic Cell. *Appl. Phys. Lett.* **1986**, *48* (2), 183–185.

(9) Yu, G.; Gao, J.; Hummelen, J. C.; Wudl, F.; Heeger, A. J. Polymer Photovoltaic Cells: Enhanced Efficiencies via a Network of Internal Donor-Acceptor Heterojunctions. *Science (80-.).* **1995**, *270* (5243), 1789. https://doi.org/10.1126/science.270.5243.1789.

(10) Halls, J. J. M.; Walsh, C. A.; Greenham, N. C.; Marseglia, E. A.; Friend, R. H.; Moratti, S. C.; Holmes, A. B. Efficient Photodiodes from Interpenetrating Polymer Networks. *Nature* **1995**, *376* (6540), 498–500.

(11) Yuan, J.; Zhang, Y.; Zhou, L.; Zhang, G.; Yip, H. L.; Lau, T. K.; Lu, X.; Zhu, C.; Peng, H.; Johnson, P. A.; Leclerc, M.; Cao, Y.; Ulanski, J.; Li, Y.; Zou, Y. Single-Junction Organic Solar Cell with over 15% Efficiency Using Fused-Ring Acceptor with Electron-Deficient Core. *Joule* **2019**, *3* (4), 1140–1151. https://doi.org/10.1016/j.joule.2019.01.004.

(12) Liu, Q.; Jiang, Y.; Jin, K.; Qin, J.; Xu, J.; Li, W.; Xiong, J.; Liu, J.; Xiao, Z.; Sun, K.; Yang, S.; Zhang, X.; Ding, L. 18% Efficiency Organic Solar Cells. *Sci. Bull.* **2020**, *65* (4), 272–275. https://doi.org/10.1016/j.scib.2020.01.001.

(13) Xiong, J.; Xu, J.; Jiang, Y.; Xiao, Z.; Bao, Q.; Hao, F.; Feng, Y.; Zhang, B.; Jin, Z.; Ding, L. Fused-Ring Bislactone Building Blocks for Polymer Donors. *Sci Bull* **2020**, *65*, 1792.

(14) Zhang, T.; An, C.; Bi, P.; Lv, Q.; Qin, J.; Hong, L.; Cui, Y.; Zhang, S.; Hou, J. A Thiadiazole-Based Conjugated Polymer with Ultradeep HOMO Level and Strong Electroluminescence Enables 18.6% Efficiency in Organic Solar Cell. *Adv. Energy Mater.* **2021**, *11* (35), 2101705.

(15) Lin, Y.; Firdaus, Y.; Isikgor, F. H.; Nugraha, M. I.; Yengel, E.; Harrison, G. T.; Hallani, R.; El-Labban, A.; Faber, H.; Ma, C. Self-Assembled Monolayer Enables Hole Transport Layer-Free Organic Solar Cells with 18% Efficiency and Improved Operational Stability. *ACS Energy Lett.* **2020**, *5* (9), 2935–2944.

(16) Cui, Y.; Yao, H.; Zhang, J.; Xian, K.; Zhang, T.; Hong, L.; Wang, Y.; Xu, Y.; Ma, K.; An, C. Single-junction Organic Photovoltaic Cells with Approaching 18% Efficiency. *Adv. Mater.* **2020**, *32* (19), 1908205.

(17) Liu, F.; Zhou, L.; Liu, W.; Zhou, Z.; Yue, Q.; Zheng, W.; Sun, R.; Liu, W.; Xu, S.; Fan, H. Organic Solar Cells with 18% Efficiency Enabled by an Alloy Acceptor: A Two-in-one Strategy. *Adv. Mater.* **2021**, *33* (27), 2100830.

(18) Atkins, P.; De Paula, J.; Friedman, R. *Quanta, Matter, and Change: A Molecular*

Approach to Physical Chemistry; Oxford University Press, 2009.
(19) Peierls, R. E. Quantum Theory of Solids–Oxford UP. *London, Engl.* **1955**, 108.
(20) Schaur, S.; Stadler, D. I. P. *Electrochemical Doping of Organic Field-Effect Transistors to Improve Contact Resistances*; na, 2010.
(21) Miller, A.; Abrahams, E. Impurity Conduction at Low Concentrations. *Phys. Rev.* **1960**, *120* (3), 745.
(22) Bässler, H. Charge Transport in Disordered Organic Photoconductors a Monte Carlo Simulation Study. *Phys. Status Solidi* **1993**, *175* (1), 15–56. https://doi.org/10.1002/pssb.2221750102.
(23) Bässler, H.; Köhler, A. Charge Transport in Organic Semiconductors. In *Unimolecular and supramolecular electronics I*; Springer, 2011; pp 1–65.
(24) Baranovski, S. *Charge Transport in Disordered Solids with Applications in Electronics*; John Wiley & Sons, 2006; Vol. 17.
(25) Kippelen, B.; Brédas, J.-L. Organic Photovoltaics. *Energy Environ. Sci.* **2009**, *2* (3), 251–261.
(26) Palik, E. D. Handbook of Optical Constants of Solids. Academic Press, New York.(Ed.). **1985**.
(27) Thompson, B. C.; Fréchet, J. M. J. Polymer-Fullerene Composite Solar Cells. *Angew. Chemie - Int. Ed.* **2008**, *47* (1), 58–77. https://doi.org/10.1002/anie.200702506.
(28) Hood, S. N.; Kassal, I. Entropy and Disorder Enable Charge Separation in Organic Solar Cells. *J. Phys. Chem. Lett.* **2016**, *7* (22), 4495–4500. https://doi.org/10.1021/acs.jpclett.6b02178.
(29) Deibel, C.; Strobel, T.; Dyakonov, V. Origin of the Efficient Polaron-Pair Dissociation in Polymer-Fullerene Blends. *Phys. Rev. Lett.* **2009**, *103* (3), 36402.
(30) Shoaee, S.; Stolterfoht, M.; Neher, D. The Role of Mobility on Charge Generation, Recombination, and Extraction in Polymer-Based Solar Cells. *Adv. Energy Mater.* **2018**, *8* (28), 1703355. https://doi.org/10.1002/aenm.201703355.
(31) Perdigón-Toro, L.; Zhang, H.; Markina, A.; Yuan, J.; Hosseini, S. M.; Wolff, C. M.; Zuo, G.; Stolterfoht, M.; Zou, Y.; Gao, F.; Andrienko, D.; Shoaee, S.; Neher, D. Barrierless Free Charge Generation in the High-Performance PM6:Y6 Bulk Heterojunction Non-Fullerene Solar Cell. *Adv. Mater.* **2020**, *32* (9), 1906763. https://doi.org/10.1002/adma.201906763.
(32) Ratcliff, E. L.; Zacher, B.; Armstrong, N. R. Selective Interlayers and Contacts in Organic Photovoltaic Cells. *J. Phys. Chem. Lett.* **2011**, *2* (11), 1337–1350.
(33) Servaites, J. D.; Ratner, M. A.; Marks, T. J. Organic Solar Cells: A New Look at Traditional Models. *Energy Environ. Sci.* **2011**, *4* (11), 4410–4422.
(34) Wagenpfahl, A.; Rauh, D.; Binder, M.; Deibel, C.; Dyakonov, V. S-Shaped Current-Voltage Characteristics of Organic Solar Devices. *Phys. Rev. B* **2010**, *82* (11), 115306.
(35) Wagenpfahl, A.; Deibel, C.; Dyakonov, V. Organic Solar Cell Efficiencies under the Aspect of Reduced Surface Recombination Velocities. *IEEE J. Sel. Top. Quantum Electron.* **2010**, *16* (6), 1759–1763.
(36) Strobel, T.; Deibel, C.; Dyakonov, V. Role of Polaron Pair Diffusion and Surface Losses in Organic Semiconductor Devices. *Phys. Rev. Lett.* **2010**, *105* (26), 266602.
(37) der internationalen Norm, I. E. C. 904-3, 1989: Photovoltaic Devices. Part.
(38) Monestier, F.; Simon, J.-J.; Torchio, P.; Escoubas, L.; Flory, F.; Bailly, S.; de Bettignies, R.; Guillerez, S.; Defranoux, C. Modeling the Short-Circuit Current Density of Polymer Solar Cells Based on P3HT: PCBM Blend. *Sol. energy Mater. Sol. cells* **2007**, *91* (5), 405–410.

(39) Burkhard, G. F.; Hoke, E. T.; McGehee, M. D. Accounting for Interference, Scattering, and Electrode Absorption to Make Accurate Internal Quantum Efficiency Measurements in Organic and Other Thin Solar Cells. *Adv. Mater.* **2010**, *22* (30), 3293–3297.
(40) Gadisa, A.; Svensson, M.; Andersson, M. R.; Inganäs, O. Correlation between Oxidation Potential and Open-Circuit Voltage of Composite Solar Cells Based on Blends of Polythiophenes/Fullerene Derivative. *Appl. Phys. Lett.* **2004**, *84* (9), 1609–1611.
(41) Vandewal, K.; Tvingstedt, K.; Gadisa, A.; Inganäs, O.; Manca, J. V. On the Origin of the Open-Circuit Voltage of Polymer-Fullerene Solar Cells. *Nat. Mater.* **2009**, *8* (11), 904–909. https://doi.org/10.1038/nmat2548.
(42) Koster, L. J. A.; Mihailetchi, V. D.; Ramaker, R.; Blom, P. W. M. Light Intensity Dependence of Open-Circuit Voltage of Polymer:Fullerene Solar Cells. *Appl. Phys. Lett.* **2005**, *86* (12), 1–3. https://doi.org/10.1063/1.1889240.
(43) D. Bartesaghi J. Kniepert, S. Roland, M. Turbiez, D. Neher & L.J.A. Koster, I. d. C. P. Competition between Recombination and Extraction of Free Charges Determines the Fill Factor of Organic Solar Cells. *Nat. Commun.* **2015**, *6* (7083), 1–10.
(44) Neher, D.; Kniepert, J.; Elimelech, A.; Koster, L. J. A. A New Figure of Merit for Organic Solar Cells with Transport-Limited Photocurrents. *Sci. Rep.* **2016**, *6*, 1–9. https://doi.org/10.1038/srep24861.
(45) Green, M.; Dunlop, E.; Hohl-Ebinger, J.; Yoshita, M.; Kopidakis, N.; Hao, X. Solar Cell Efficiency Tables (Version 57). *Prog. photovoltaics Res. Appl.* **2021**, *29* (1), 3–15.
(46) Shockley, W.; Queisser, H. J. Detailed Balance Limit of Efficiency of P-n Junction Solar Cells. *J. Appl. Phys.* **1961**, *32* (3), 510–519. https://doi.org/10.1063/1.1736034.
(47) Würfel, P.; Würfel, U. Physics of Solar Cells: From Basic Principles to Advanced Concepts (Physics Textbook). Wiley-VCH 2009.
(48) Onsager, L. Initial Recombination of Ions. *Phys. Rev.* **1938**, *54* (8), 554.
(49) Tachiya, M. Breakdown of the Onsager Theory of Geminate Ion Recombination. *J. Chem. Phys.* **1988**, *89* (11), 6929–6935.
(50) Braun, C. L. Electric Field Assisted Dissociation of Charge Transfer States as a Mechanism of Photocarrier Production. *J. Chem. Phys.* **1984**, *80* (9), 4157–4161.
(51) Mihailetchi, V. D.; Koster, L. J. A.; Hummelen, J. C.; Blom, P. W. M. Photocurrent Generation in Polymer-Fullerene Bulk Heterojunctions. *Phys. Rev. Lett.* **2004**, *93* (21), 216601.
(52) Koster, L. J. A.; Smits, E. C. P.; Mihailetchi, V. D.; Blom, P. W. M. Device Model for the Operation of Polymer/Fullerene Bulk Heterojunction Solar Cells. *Phys. Rev. B - Condens. Matter Mater. Phys.* **2005**, *72* (8), 85205. https://doi.org/10.1103/PhysRevB.72.085205.
(53) Clarke, T. M.; Durrant, J. R. Charge Photogeneration in Organic Solar Cells. *Chem. Rev.* **2010**, *110* (11), 6736–6767.
(54) Langevin, P. Recombinaison et Mobilites Des Ions Dans Les Gaz. *Ann. Chim. Phys.* **1903**, *28* (433), 433–530.
(55) Adriaenssens, G. J.; Arkhipov, V. I. Non-Langevin Recombination in Disordered Materials with Random Potential Distributions. *Solid State Commun.* **1997**, *103* (9), 541–543.
(56) Koster, L. J. A.; Mihailetchi, V. D.; Blom, P. W. M. Bimolecular Recombination in Polymer/Fullerene Bulk Heterojunction Solar Cells. *Appl. Phys. Lett.* **2006**, *88* (5), 52104.
(57) Mozer, A. J.; Sariciftci, N. S.; Lutsen, L.; Vanderzande, D.; Österbacka, R.; Westerling,

M.; Juška, G. Charge Transport and Recombination in Bulk Heterojunction Solar Cells Studied by the Photoinduced Charge Extraction in Linearly Increasing Voltage Technique. *Appl. Phys. Lett.* **2005**, *86* (11), 112104.

(58) Deibel, C.; Wagenpfahl, A.; Dyakonov, V. Origin of Reduced Polaron Recombination in Organic Semiconductor Devices. *Phys. Rev. B - Condens. Matter Mater. Phys.* **2009**, *80* (7), 75203. https://doi.org/10.1103/PhysRevB.80.075203.

(59) Hilczer, M.; Tachiya, M. Unified Theory of Geminate and Bulk Electron-Hole Recombination in Organic Solar Cells. *J. Phys. Chem. C* **2010**, *114* (14), 6808–6813. https://doi.org/10.1021/jp912262h.

(60) Schwarz, K. N.; Geraghty, P. B.; Jones, D. J.; Smith, T. A.; Ghiggino, K. P. Suppressing Subnanosecond Bimolecular Charge Recombination in a High-Performance Organic Photovoltaic Material. *J. Phys. Chem. C* **2016**, *120* (42), 24002–24010. https://doi.org/10.1021/acs.jpcc.6b08354.

(61) Heiber, M. C.; Baumbach, C.; Dyakonov, V.; Deibel, C. Encounter-Limited Charge-Carrier Recombination in Phase-Separated Organic Semiconductor Blends. *Phys. Rev. Lett.* **2015**, *114* (13), 136602. https://doi.org/10.1103/PhysRevLett.114.136602.

(62) Kniepert, J.; Lange, I.; Van Der Kaap, N. J.; Koster, L. J. A.; Neher, D. A Conclusive View on Charge Generation, Recombination, and Extraction in as-Prepared and Annealed P3HT:PCBM Blends: Combined Experimental and Simulation Work. *Adv. Energy Mater.* **2014**, *4* (7), 1301401. https://doi.org/10.1002/aenm.201301401.

(63) Armin, A.; Subbiah, J.; Stolterfoht, M.; Shoaee, S.; Xiao, Z.; Lu, S.; Jones, D. J. D. J.; Meredith, P. Reduced Recombination in High Efficiency Molecular Nematic Liquid Crystalline: Fullerene Solar Cells. *Adv. Energy Mater.* **2016**, *6* (22), 1600939. https://doi.org/10.1002/aenm.201600939.

(64) Roland, S. Charge Carrier Recombination and Open Circuit Voltage in Organic Solar Cells : From Bilayer-Model Systems to Hybrid Dissertation. **2017**, 1–152.

(65) Kelly, M. A.; Roland, S.; Zhang, Q.; Lee, Y.; Kabius, B.; Wang, Q.; Gomez, E. D.; Neher, D.; You, W. Incorporating Fluorine Substitution into Conjugated Polymers for Solar Cells: Three Different Means, Same Results. *J. Phys. Chem. C* **2017**, *121* (4), 2059–2068. https://doi.org/10.1021/acs.jpcc.6b10993.

(66) Mihailetchi, V. D.; Blom, P. W. M.; Hummelen, J. C.; Rispens, M. T. Cathode Dependence of the Open-Circuit Voltage of Polymer: Fullerene Bulk Heterojunction Solar Cells. *J. Appl. Phys.* **2003**, *94* (10), 6849–6854.

(67) Scharber, M. C.; Mühlbacher, D.; Koppe, M.; Denk, P.; Waldauf, C.; Heeger, A. J.; Brabec, C. J. Design Rules for Donors in Bulk-heterojunction Solar Cells—Towards 10% Energy-conversion Efficiency. *Adv. Mater.* **2006**, *18* (6), 789–794.

(68) Werner, J.; Nogay, G.; Sahli, F.; Yang, T. C.-J.; Bräuninger, M.; Christmann, G.; Walter, A.; Kamino, B. A.; Fiala, P.; Löper, P. Complex Refractive Indices of Cesium–Formamidinium-Based Mixed-Halide Perovskites with Optical Band Gaps from 1.5 to 1.8 EV. *ACS Energy Lett.* **2018**, *3* (3), 742–747.

(69) Filip, M. R.; Eperon, G. E.; Snaith, H. J.; Giustino, F. Steric Engineering of Metal-Halide Perovskites with Tunable Optical Band Gaps. *Nat. Commun.* **2014**, *5* (1), 1–9.

(70) Baran, D.; Kirchartz, T.; Wheeler, S.; Dimitrov, S.; Abdelsamie, M.; Gorman, J.; Ashraf, R. S.; Holliday, S.; Wadsworth, A.; Gasparini, N.; Kaienburg, P.; Yan, H.; Amassian, A.; Brabec, C. J.; Durrant, J. R.; McCulloch, I. Reduced Voltage Losses Yield 10% Efficient Fullerene Free Organic Solar Cells with >1 V Open Circuit Voltages. *Energy Environ. Sci.* **2016**, *9* (12), 3783–3793. https://doi.org/10.1039/c6ee02598f.

(71) Kirchartz, T.; Taretto, K.; Rau, U. Efficiency Limits of Organic Bulk Heterojunction Solar

Cells. *J. Phys. Chem. C* **2009**, *113* (41), 17958–17966.
(72) Koster, L. J. A.; Shaheen, S. E.; Hummelen, J. C. Pathways to a New Efficiency Regime for Organic Solar Cells. *Adv. Energy Mater.* **2012**, *2* (10), 1246–1253.
(73) Rau, U. Reciprocity Relation between Photovoltaic Quantum Efficiency and Electroluminescent Emission of Solar Cells. *Phys. Rev. B - Condens. Matter Mater. Phys.* **2007**, *76* (8), 85303. https://doi.org/10.1103/PhysRevB.76.085303.
(74) Benduhn, J.; Tvingstedt, K.; Piersimoni, F.; Ullbrich, S.; Fan, Y.; Tropiano, M.; McGarry, K. A.; Zeika, O.; Riede, M. K.; Douglas, C. J.; Barlow, S.; Marder, S. R.; Neher, D.; Spoltore, D.; Vandewal, K. Intrinsic Non-Radiative Voltage Losses in Fullerene-Based Organic Solar Cells. *Nat. Energy* **2017**, *2* (6), 17053. https://doi.org/10.1038/nenergy.2017.53.
(75) Duffy, N. W.; Peter, L. M.; Rajapakse, R. M. G.; Wijayantha, K. G. U. A Novel Charge Extraction Method for the Study of Electron Transport and Interfacial Transfer in Dye Sensitised Nanocrystalline Solar Cells. *Electrochem. commun.* **2000**, *2* (9), 658–662.
(76) Kurpiers, J. Probing the Pathways of Free Charge Generation and Recombination in Organic Solar Cells. Universität Potsdam 2019.
(77) Mort, J.; Chen, I.; Troup, A.; Morgan, M.; Knights, J.; Lujan, R. Nongeminate Recombination of A-Si: H. *Phys. Rev. Lett.* **1980**, *45* (16), 1348.
(78) Offermans, T.; Meskers, S. C. J.; Janssen, R. A. J. Time Delayed Collection Field Experiments on Polymer: Fullerene Bulk-Heterojunction Solar Cells. *J. Appl. Phys.* **2006**, *100* (7), 74509.
(79) Kniepert, J.; Schubert, M.; Blakesley, J. C.; Neher, D. Photogeneration and Recombination in P3HT/PCBM Solar Cells Probed by Time-Delayed Collection Field Experiments. *J. Phys. Chem. Lett.* **2011**, *2* (7), 700–705. https://doi.org/10.1021/jz200155b.
(80) Mingebach, M.; Walter, S.; Dyakonov, V.; Deibel, C. Direct and Charge Transfer State Mediated Photogeneration in Polymer-Fullerene Bulk Heterojunction Solar Cells. *Appl. Phys. Lett.* **2012**, *100* (19), 106. https://doi.org/10.1063/1.4711849.
(81) Hosseini, S. M.; Roland, S.; Kurpiers, J.; Chen, Z.; Zhang, K.; Huang, F.; Armin, A.; Neher, D.; Shoaee, S. Impact of Bimolecular Recombination on the Fill Factor of Fullerene and Nonfullerene-Based Solar Cells: A Comparative Study of Charge Generation and Extraction. *J. Phys. Chem. C* **2019**, *123* (11), 6823–6830. https://doi.org/10.1021/acs.jpcc.8b11669.
(82) Zhang, G.; Zhao, J.; Chow, P. C. Y.; Jiang, K.; Zhang, J.; Zhu, Z.; Zhang, J.; Huang, F.; Yan, H. Nonfullerene Acceptor Molecules for Bulk Heterojunction Organic Solar Cells. *Chem. Rev.* **2018**, *118* (7), 3447–3507. https://doi.org/10.1021/acs.chemrev.7b00535.
(83) Green, M. A.; Emery, K.; Hishikawa, Y.; Warta, W. Solar Cell Efficiency Tables (Version 37). *Prog. photovoltaics Res. Appl.* **2010**, *1* (19), 84–92.
(84) Meredith, P.; Armin, A. LED Technology Breaks Performance Barrier. *Nature*. Nature Publishing Group 2018, pp 197–198. https://doi.org/10.1038/d41586-018-06923-y.
(85) Bartesaghi, D.; Pérez, I. D. C.; Kniepert, J.; Roland, S.; Turbiez, M.; Neher, D.; Koster, L. J. A. Competition between Recombination and Extraction of Free Charges Determines the Fill Factor of Organic Solar Cells. *Nat. Commun.* **2015**, *6*, 7083. https://doi.org/10.1038/ncomms8083.
(86) Heiber, M. C.; Okubo, T.; Ko, S. J.; Luginbuhl, B. R.; Ran, N. A.; Wang, M.; Wang, H.; Uddin, M. A.; Woo, H. Y.; Bazan, G. C.; Nguyen, T. Q. Measuring the Competition between Bimolecular Charge Recombination and Charge Transport in Organic Solar Cells under Operating Conditions. *Energy Environ. Sci.* **2018**, *11* (10), 3019–3032.

https://doi.org/10.1039/c8ee01559g.
(87) Marsh, R. A.; Hodgkiss, J. M.; Friend, R. H. Direct Measurement of Electric Field-Assisted Charge Separation in Polymer: Fullerene Photovoltaic Diodes. *Adv. Mater.* **2010**, *22* (33), 3672–3676. https://doi.org/10.1002/adma.201001010.
(88) Albrecht, S.; Schindler, W.; Kurpiers, J.; Kniepert, J.; Blakesley, J. C.; Dumsch, I.; Allard, S.; Fostiropoulos, K.; Scherf, U.; Neher, D. On the Field Dependence of Free Charge Carrier Generation and Recombination in Blends of PCPDTBT/PC 70BM: Influence of Solvent Additives. *J. Phys. Chem. Lett.* **2012**, *3* (5), 640–645. https://doi.org/10.1021/jz3000849.
(89) Wetzelaer, G. J. A. H.; Van Der Kaap, N. J.; Koster, J. A.; Blom, P. W. M. Quantifying Bimolecular Recombination in Organic Solar Cells in Steady State. *Adv. Energy Mater.* **2013**, *3* (9), 1130–1134. https://doi.org/10.1002/aenm.201300251.
(90) Guo, J.; Ohkita, H.; Benten, H.; Ito, S. Charge Generation and Recombination Dynamics in Poly(3-Hexylthiophene)/ Fullerene Blend Films with Different Regioregularities and Morphologies. *J. Am. Chem. Soc.* **2010**, *132* (17), 6154–6164. https://doi.org/10.1021/ja100302p.
(91) Rauh, D.; Deibel, C.; Dyakonov, V. Charge Density Dependent Nongeminate Recombination in Organic Bulk Heterojunction Solar Cells. *Adv. Funct. Mater.* **2012**, *22* (16), 3371–3377. https://doi.org/10.1002/adfm.201103118.
(92) Wheeler, S.; Deledalle, F.; Tokmoldin, N.; Kirchartz, T.; Nelson, J.; Durrant, J. R. Influence of Surface Recombination on Charge-Carrier Kinetics in Organic Bulk Heterojunction Solar Cells with Nickel Oxide Interlayers. *Phys. Rev. Appl.* **2015**, *4* (2), 24020. https://doi.org/10.1103/PhysRevApplied.4.024020.
(93) Sandberg, O. J.; Nyman, M.; Dahlström, S.; Sandén, S.; Smått, J.-H.; Österbacka, R. Quantifying Loss-Mechanisms Related to Charge Carrier Collection in Thin-Film Solar Cells (Conference Presentation); 2018; Vol. 10737, p 8. https://doi.org/10.1117/12.2323759.
(94) Jin, Y.; Chen, Z.; Dong, S.; Zheng, N.; Ying, L.; Jiang, X. F.; Liu, F.; Huang, F.; Cao, Y. A Novel Naphtho[1,2-c:5,6-C']Bis([1,2,5]Thiadiazole)-Based Narrow-Bandgap π-Conjugated Polymer with Power Conversion Efficiency Over 10%. *Adv. Mater.* **2016**, *28* (44), 9811–9818. https://doi.org/10.1002/adma.201603178.
(95) Armin, A.; Chen, Z.; Jin, Y.; Zhang, K.; Huang, F.; Shoaee, S. A Shockley-Type Polymer: Fullerene Solar Cell. *Adv. Energy Mater.* **2018**, *8* (7), 1701450. https://doi.org/10.1002/aenm.201701450.
(96) Kirchartz, T.; Agostinelli, T.; Campoy-Quiles, M.; Gong, W.; Nelson, J. Understanding the Thickness-Dependent Performance of Organic Bulk Heterojunction Solar Cells: The Influence of Mobility, Lifetime, and Space Charge. *J. Phys. Chem. Lett.* **2012**, *3* (23), 3470–3475. https://doi.org/10.1021/jz301639y.
(97) Mauer, R.; Howard, I. A.; Laquai, F. Effect of Nongeminate Recombination on Fill Factor in Polythiophene/ Methanofullerene Organic Solar Cells. *J. Phys. Chem. Lett.* **2010**, *1* (24), 3500–3505. https://doi.org/10.1021/jz101458y.
(98) Shoaee, S.; Subramaniyan, S.; Xin, H.; Keiderling, C.; Tuladhar, P. S.; Jamieson, F.; Jenekhe, S. A.; Durrant, J. R. Charge Photogeneration for a Series of Thiazolo-Thiazole Donor Polymers Blended with the Fullerene Electron Acceptors PCBM and ICBA. *Adv. Funct. Mater.* **2013**, *23* (26), 3286–3298. https://doi.org/10.1002/adfm.201203148.
(99) Philippa, B.; Stolterfoht, M.; Burn, P. L.; Juška, G.; Meredith, P.; White, R. D.; Pivrikas, A. The Impact of Hot Charge Carrier Mobility on Photocurrent Losses in Polymer-Based Solar Cells. *Sci. Rep.* **2014**, *4*, 5695. https://doi.org/10.1038/srep05695.

(100) Stolterfoht, M.; Armin, A.; Shoaee, S.; Kassal, I.; Burn, P.; Meredith, P. Slower Carriers Limit Charge Generation in Organic Semiconductor Light-Harvesting Systems. *Nat. Commun.* **2016**, *7* (May), 11944. https://doi.org/10.1038/ncomms11944.
(101) Armin, A.; Juska, G.; Ullah, M.; Velusamy, M.; Burn, P. L.; Meredith, P.; Pivrikas, A. Balanced Carrier Mobilities: Not a Necessary Condition for High-Efficiency Thin Organic Solar Cells as Determined by MIS-CELIV. *Adv. Energy Mater.* **2014**, *4* (4), 1300954. https://doi.org/10.1002/aenm.201300954.
(102) Athanasopoulos, S.; Tscheuschner, S.; Bässler, H.; Köhler, A. Efficient Charge Separation of Cold Charge-Transfer States in Organic Solar Cells Through Incoherent Hopping. *J. Phys. Chem. Lett.* **2017**, *8* (9), 2093–2098. https://doi.org/10.1021/acs.jpclett.7b00595.
(103) Mihailetchi, V. D.; Wildeman, J.; Blom, P. W. M. Space-Charge Limited Photocurrent. *Phys. Rev. Lett.* **2005**, *94* (12), 1–4. https://doi.org/10.1103/PhysRevLett.94.126602.
(104) Kurpiers, J.; Ferron, T.; Roland, S.; Jakoby, M.; Thiede, T.; Jaiser, F.; Albrecht, S.; Janietz, S.; Collins, B. A.; Howard, I. A.; Neher, D. Probing the Pathways of Free Charge Generation in Organic Bulk Heterojunction Solar Cells. *Nat. Commun.* **2018**, *9* (1), 2038. https://doi.org/10.1038/s41467-018-04386-3.
(105) Armin, A.; Durrant, J. R. J. R.; Shoaee, S. Interplay between Triplet-, Singlet-Charge Transfer States and Free Charge Carriers Defining Bimolecular Recombination Rate Constant of Organic Solar Cells. *J. Phys. Chem. C* **2017**, *121* (25), 13969–13976. https://doi.org/10.1021/acs.jpcc.7b04825.
(106) Ferguson, A. J.; Kopidakis, N.; Shaheen, S. E.; Rumbles, G. Dark Carriers, Trapping, and Activation Control of Carrier Recombination in Neat P3HT and P3HT:PCBM Blends. *J. Phys. Chem. C* **2011**, *115* (46), 23134–23148. https://doi.org/10.1021/jp208014v.
(107) Shoaee, S.; Deledalle, F.; Tuladhar, P. S. P. S.; Shivanna, R.; Rajaram, S.; Narayan, K. S. S.; Durrant, J. R. J. R. A Comparison of Charge Separation Dynamics in Organic Blend Films Employing Fullerene and Perylene Diimide Electron Acceptors. *J. Phys. Chem. Lett.* **2015**, *6* (1), 201–205. https://doi.org/10.1021/jz502385n.
(108) Shoaee, S.; Clarke, T. M.; Huang, C.; Barlow, S.; Marder, S. R.; Heeney, M.; McCulloch, I.; Durrant, J. R. Acceptor Energy Level Control of Charge Photogeneration in Organic Donor/Acceptor Blends. *J. Am. Chem. Soc.* **2010**, *132* (37), 12919–12926. https://doi.org/10.1021/ja1042726.
(109) Song, X.; Gasparini, N.; Ye, L.; Yao, H.; Hou, J.; Ade, H.; Baran, D. Controlling Blend Morphology for Ultrahigh Current Density in Nonfullerene Acceptor-Based Organic Solar Cells. *ACS Energy Lett.* **2018**, *3* (3), 669–676. https://doi.org/10.1021/acsenergylett.7b01266.
(110) Wadsworth, A.; Ashraf, R. S.; Abdelsamie, M.; Pont, S.; Little, M.; Moser, M.; Hamid, Z.; Neophytou, M.; Zhang, W.; Amassian, A.; Durrant, J. R.; Baran, D.; McCulloch, I. Highly Efficient and Reproducible Nonfullerene Solar Cells from Hydrocarbon Solvents. *ACS Energy Lett.* **2017**, *2* (7), 1494–1500. https://doi.org/10.1021/acsenergylett.7b00390.
(111) Hosseini, S. M.; Tokmoldin, N.; Lee, Y. W.; Zou, Y.; Woo, H. Y.; Neher, D.; Shoaee, S. Putting Order into PM6:Y6 Solar Cells to Reduce the Langevin Recombination in 400 Nm Thick Junction. *Sol. RRL* **2020**. https://doi.org/10.1002/solr.202000498.
(112) Phuong, L. Q.; Hosseini, S. M.; Koh, C. W.; Woo, H. Y.; Shoaee, S. Measuring Competing Recombination Losses in a Significantly Reduced Langevin System by Steady-State Photoinduced Absorption and Photocurrent Spectroscopy. *J. Phys. Chem. C* **2019**, *123* (45), 27417–27422. https://doi.org/10.1021/acs.jpcc.9b08901.

(113) Schwarz, K. N.; Geraghty, P. B.; Mitchell, V. D.; Khan, S. U. Z.; Sandberg, O. J.; Zarrabi, N.; Kudisch, B.; Subbiah, J.; Smith, T. A.; Rand, B. P.; Armin, A.; Scholes, G. D.; Jones, D. J.; Ghiggino, K. P. Reduced Recombination and Capacitor-like Charge Buildup in an Organic Heterojunction. *J. Am. Chem. Soc.* **2020**, *142* (5), 2562–2571. https://doi.org/10.1021/jacs.9b12526.
(114) Van Bavel, S.; Sourty, E.; De With, G.; Frolic, K.; Loos, J. Relation between Photoactive Layer Thickness, 3D Morphology, and Device Performance in P3HT/PCBM Bulk-Heterojunction Solar Cells. *Macromolecules* **2009**, *42* (19), 7396–7403. https://doi.org/10.1021/ma900817t.
(115) Yao, H.; Cui, Y.; Qian, D.; Ponseca, C. S.; Honarfar, A.; Xu, Y.; Xin, J.; Chen, Z.; Hong, L.; Gao, B.; Yu, R.; Zu, Y.; Ma, W.; Chabera, P.; Pullerits, T.; Yartsev, A.; Gao, F.; Hou, J. 14.7% Efficiency Organic Photovoltaic Cells Enabled by Active Materials with a Large Electrostatic Potential Difference. *J. Am. Chem. Soc.* **2019**, *141* (19), 7743–7750. https://doi.org/10.1021/jacs.8b12937.
(116) Yi, X.; Gautam, B.; Constantinou, I.; Cheng, Y.; Peng, Z.; Klump, E.; Ba, X.; Ho, C. H. Y.; Dong, C.; Marder, S. R.; Reynolds, J. R.; Tsang, S. W.; Ade, H.; So, F. Impact of Nonfullerene Molecular Architecture on Charge Generation, Transport, and Morphology in PTB7-Th-Based Organic Solar Cells. *Adv. Funct. Mater.* **2018**, *28* (32), 1802702. https://doi.org/10.1002/adfm.201802702.
(117) Tang, A.; Xiao, B.; Wang, Y.; Gao, F.; Tajima, K.; Bin, H.; Zhang, Z. G.; Li, Y.; Wei, Z.; Zhou, E. Simultaneously Achieved High Open-Circuit Voltage and Efficient Charge Generation by Fine-Tuning Charge-Transfer Driving Force in Nonfullerene Polymer Solar Cells. *Adv. Funct. Mater.* **2018**, *28* (6), 1704507. https://doi.org/10.1002/adfm.201704507.
(118) Liu, J.; Chen, S.; Qian, D.; Gautam, B.; Yang, G.; Zhao, J.; Bergqvist, J.; Zhang, F.; Ma, W.; Ade, H.; Inganäs, O.; Gundogdu, K.; Gao, F.; Yan, H. Fast Charge Separation in a Non-Fullerene Organic Solar Cell with a Small Driving Force. *Nat. Energy* **2016**, *1* (7), 16089. https://doi.org/10.1038/nenergy.2016.89.
(119) Shoaee, S.; Armin, A.; Stolterfoht, M.; Hosseini, S. M.; Kurpiers, J.; Neher, D. Decoding Charge Recombination through Charge Generation in Organic Solar Cells. *Sol. RRL* **2019**, *3* (11), 1900184. https://doi.org/10.1002/solr.201900184.
(120) Burke, T. M.; McGehee, M. D. How High Local Charge Carrier Mobility and an Energy Cascade in a Three-Phase Bulk Heterojunction Enable >90% Quantum Efficiency. *Adv. Mater.* **2014**, *26* (12), 1923–1928. https://doi.org/10.1002/adma.201304241.
(121) Gartstein, Y. N.; Conwell, E. M. High-Field Hopping Mobility in Molecular Systems with Spatially Correlated Energetic Disorder. *Chem. Phys. Lett.* **1995**, *245* (4–5), 351–358. https://doi.org/10.1016/0009-2614(95)01031-4.
(122) Groves, C.; Blakesley, J. C.; Greenham, N. C. Effect of Charge Trapping on Geminate Recombination and Polymer Solar Cell Performance. *Nano Lett.* **2010**, *10* (3), 1063–1069. https://doi.org/10.1021/nl100080r.
(123) Stolterfoht, M.; Shoaee, S.; Armin, A.; Jin, H.; Kassal, I.; Jiang, W.; Burn, P.; Meredith, P. Electric Field and Mobility Dependent First-Order Recombination Losses in Organic Solar Cells. *Adv. Energy Mater.* **2017**, *7* (4), 1601379.
(124) Tokmoldin, N.; Hosseini, S. M.; Raoufi, M.; Phuong, L. Q.; Sandberg, O. J.; Guan, H.; Zou, Y.; Neher, D.; Shoaee, S. Extraordinarily Long Diffusion Length in PM6:Y6 Organic Solar Cells. *J. Mater. Chem. A* **2020**, *8* (16), 7854–7860. https://doi.org/10.1039/d0ta03016c.
(125) Brendel, R.; Queisser, H. J. On the Thickness Dependence of Open Circuit Voltages of

P-n Junction Solar Cells. *Sol. Energy Mater. Sol. Cells* **1993**, *29* (4), 397–401. https://doi.org/10.1016/0927-0248(93)90098-N.
(126) Zhang, Y.; Dang, X. D.; Kim, C.; Nguyen, T. Q. Effect of Charge Recombination on the Fill Factor of Small Molecule Bulk Heterojunction Solar Cells. *Adv. Energy Mater.* **2011**, *1* (4), 610–617. https://doi.org/10.1002/aenm.201100040.
(127) Yu, H.; Yi, R.; Zhang, J.; Yu, A.; Peng, H.; Qin, J.; Hou, X. Effect of Diffusion Current on Fill Factor in Organic Solar Cells. *J. Phys. D. Appl. Phys.* **2016**, *49* (20), 3500–3505. https://doi.org/10.1088/0022-3727/49/20/205105.
(128) Tress, W.; Merten, A.; Furno, M.; Hein, M.; Leo, K.; Riede, M. Correlation of Absorption Profile and Fill Factor in Organic Solar Cells: The Role of Mobility Imbalance. *Adv. Energy Mater.* **2013**, *3* (5), 631–638. https://doi.org/10.1002/aenm.201200835.
(129) Tress, W.; Petrich, A.; Hummert, M.; Hein, M.; Leo, K.; Riede, M. Imbalanced Mobilities Causing S-Shaped IV Curves in Planar Heterojunction Organic Solar Cells. *Appl. Phys. Lett.* **2011**, *98* (6), 23. https://doi.org/10.1063/1.3553764.
(130) Stolterfoht, M.; Armin, A.; Philippa, B.; Neher, D. The Role of Space Charge Effects on the Competition between Recombination and Extraction in Solar Cells with Low-Mobility Photoactive Layers. *J. Phys. Chem. Lett.* **2016**, *7* (22), 4716–4721. https://doi.org/10.1021/acs.jpclett.6b02106.
(131) Wilken, S.; Sandberg, O. J.; Scheunemann, D.; Österbacka, R. Watching Space Charge Build Up in an Organic Solar Cell. *Sol. RRL* **2020**, *4* (3), 1900505.
(132) Varache, R.; Leendertz, C.; Gueunier-Farret, M. E.; Haschke, J.; Muñoz, D.; Korte, L. Investigation of Selective Junctions Using a Newly Developed Tunnel Current Model for Solar Cell Applications. *Sol. Energy Mater. Sol. Cells* **2015**, *141*, 14–23. https://doi.org/10.1016/j.solmat.2015.05.014.
(133) Song, J.; Li, C.; Zhu, L.; Guo, J.; Xu, J.; Zhang, X.; Weng, K.; Zhang, K.; Min, J.; Hao, X. Ternary Organic Solar Cells with Efficiency> 16.5% Based on Two Compatible Nonfullerene Acceptors. *Adv. Mater.* **2019**, *31* (52), 1905645.
(134) Bi, Z.; Zhu, Q.; Xu, X.; Naveed, H. B.; Sui, X.; Xin, J.; Zhang, L.; Li, T.; Zhou, K.; Liu, X. Efficient Quaternary Organic Solar Cells with Parallel-Alloy Morphology. *Adv. Funct. Mater.* **2019**, *29* (9), 1806804.
(135) Yang, C.; Sun, Y.; Li, Q.; Liu, K.; Xue, X.; Huang, Y.; Ren, K.; Li, L.; Chen, Y.; Wang, Z. Nonfullerene Ternary Organic Solar Cell with Effective Charge Transfer between Two Acceptors. *J. Phys. Chem. Lett.* **2020**, *11* (3), 927–934.
(136) Du, B.; Geng, R.; Li, W.; Li, D.; Mao, Y.; Chen, M.; Zhang, X.; Smith, J. A.; Kilbride, R. C.; O'Kane, M. E. 13.9% Efficiency Ternary Nonfullerene Organic Solar Cells Featuring Low-Structural Order. *ACS Energy Lett.* **2019**, *4* (10), 2378–2385.
(137) Pan, M.-A.; Lau, T.-K.; Tang, Y.; Wu, Y.-C.; Liu, T.; Li, K.; Chen, M.-C.; Lu, X.; Ma, W.; Zhan, C. 16.7%-Efficiency Ternary Blended Organic Photovoltaic Cells with PCBM as the Acceptor Additive to Increase the Open-Circuit Voltage and Phase Purity. *J. Mater. Chem. A* **2019**, *7* (36), 20713–20722.
(138) Zhu, Y.; Gadisa, A.; Peng, Z.; Ghasemi, M.; Ye, L.; Xu, Z.; Zhao, S.; Ade, H. Rational Strategy to Stabilize an Unstable High-efficiency Binary Nonfullerene Organic Solar Cells with a Third Component. *Adv. Energy Mater.* **2019**, *9* (20), 1900376.
(139) Singh, R.; Lee, J.; Kim, M.; Keivanidis, P. E.; Cho, K. Control of the Molecular Geometry and Nanoscale Morphology in Perylene Diimide Based Bulk Heterojunctions Enables an Efficient Non-Fullerene Organic Solar Cell. *J. Mater. Chem. A* **2017**, *5* (1), 210–220. https://doi.org/10.1039/C6TA08870H.

(140) Rogers, J. T.; Schmidt, K.; Toney, M. F.; Kramer, E. J.; Bazan, G. C. Structural Order in Bulk Heterojunction Films Prepared with Solvent Additives. *Adv. Mater.* **2011**, *23* (20), 2284–2288. https://doi.org/10.1002/adma.201003690.
(141) Zhang, S.; Ye, L.; Zhao, W.; Yang, B.; Wang, Q.; Hou, J. Realizing over 10% Efficiency in Polymer Solar Cell by Device Optimization. *Sci. China Chem.* **2015**, *58* (2), 248–256. https://doi.org/10.1007/s11426-014-5273-x.
(142) Jain, N.; Chandrasekaran, N.; Sadhanala, A.; Friend, R. H.; McNeill, C. R.; Kabra, D. Interfacial Disorder in Efficient Polymer Solar Cells: The Impact of Donor Molecular Structure and Solvent Additives. *J. Mater. Chem. A* **2017**, *5* (47), 24749–24757. https://doi.org/10.1039/c7ta07924a.
(143) FRÖHLICH, H. Electronic Processes in Ionic Crystals. *Nature* **1949**, *164* (4166), 377–377. https://doi.org/10.1038/164377a0.
(144) Felekidis, N.; Melianas, A.; Kemerink, M. Design Rule for Improved Open-Circuit Voltage in Binary and Ternary Organic Solar Cells. *ACS Appl. Mater. Interfaces* **2017**, *9* (42), 37070–37077. https://doi.org/10.1021/acsami.7b08276.
(145) Zuo, G.; Li, Z.; Andersson, O.; Abdalla, H.; Wang, E.; Kemerink, M. Molecular Doping and Trap Filling in Organic Semiconductor Host-Guest Systems. *J. Phys. Chem. C* **2017**, *121* (14), 7767–7775. https://doi.org/10.1021/acs.jpcc.7b01758.
(146) Mark, P.; Helfrich, W. Space-Charge-Limited Currents in Organic Crystals. *J. Appl. Phys.* **1962**, *33* (1), 205–215. https://doi.org/10.1063/1.1728487.
(147) Van Mensfoort, S. L. M.; Vulto, S. I. E.; Janssen, R. A. J.; Coehoorn, R. Hole Transport in Polyfluorene-Based Sandwich-Type Devices: Quantitative Analysis of the Role of Energetic Disorder. *Phys. Rev. B - Condens. Matter Mater. Phys.* **2008**, *78* (8), 85208. https://doi.org/10.1103/PhysRevB.78.085208.
(148) Nicolai, H. T.; Wetzelaer, G. A. H.; Kuik, M.; Kronemeijer, A. J.; De Boer, B.; Blom, P. W. M. Space-Charge-Limited Hole Current in Poly(9,9-Dioctylfluorene) Diodes. *Appl. Phys. Lett.* **2010**, *96* (17), 172107. https://doi.org/10.1063/1.3391668.
(149) Murgatroyd, P. N. Theory of Space-Charge-Limited Current Enhanced by Frenkel Effect. *J. Phys. D. Appl. Phys.* **1970**, *3* (2), 151–156. https://doi.org/10.1088/0022-3727/3/2/308.
(150) Wu, J.; Lee, J.; Chin, Y.-C.; Yao, H.; Cha, H.; Luke, J.; Hou, J.; Kim, J.-S.; Durrant, J. Exceptionally Low Charge Trapping Enables Highly Efficient Organic Bulk Heterojunction Solar Cells. *Energy Environ. Sci.* **2020**.
(151) Jiang, K.; Wei, Q.; Lai, J. Y. L.; Peng, Z.; Kim, H. K.; Yuan, J.; Ye, L.; Ade, H.; Zou, Y.; Yan, H. Alkyl Chain Tuning of Small Molecule Acceptors for Efficient Organic Solar Cells. *Joule* **2019**, *3* (12), 3020–3033. https://doi.org/10.1016/j.joule.2019.09.010.
(152) Zhan, L.; Li, S.; Lau, T. K.; Cui, Y.; Lu, X.; Shi, M.; Li, C. Z.; Li, H.; Hou, J.; Chen, H. Over 17% Efficiency Ternary Organic Solar Cells Enabled by Two Non-Fullerene Acceptors Working in an Alloy-like Model. *Energy Environ. Sci.* **2020**, *13* (2), 635–645. https://doi.org/10.1039/c9ee03710a.
(153) Karki, A.; Vollbrecht, J.; Dixon, A. L.; Schopp, N.; Schrock, M.; Reddy, G. N. M.; Nguyen, T. Q. Understanding the High Performance of over 15% Efficiency in Single-Junction Bulk Heterojunction Organic Solar Cells. *Adv. Mater.* **2019**, *31* (48), 1903868. https://doi.org/10.1002/adma.201903868.
(154) Murphy, L.; Hong, W.; Aziz, H.; Li, Y. Organic Photovoltaics with Thick Active Layers (~800 Nm) Using a High Mobility Polymer Donor. *Sol. Energy Mater. Sol. Cells* **2013**, *114*, 71–81. https://doi.org/10.1016/j.solmat.2013.02.033.
(155) Friend, R. Management of the Coulomb Interaction in Organic LEDs and Solar Cells. In

Proceedings of the 12th Online International Conference on Hybrid and Organic Photovoltaics; Fundació Scito: València, 2020. https://doi.org/10.29363/nanoge.onlinehopv.2020.012.
(156) Yuan, J.; Zhang, Y.; Zhou, L.; Zhang, G.; Yip, H.-L.; Lau, T.-K.; Lu, X.; Zhu, C.; Peng, H.; Johnson, P. A.; Leclerc, M.; Cao, Y.; Ulanski, J.; Li, Y.; Zou, Y. Single-Junction Organic Solar Cell with over 15% Efficiency Using Fused-Ring Acceptor with Electron-Deficient Core. *Joule* **2019**, *3* (4), 1140–1151. https://doi.org/https://doi.org/10.1016/j.joule.2019.01.004.
(157) Narayanan, S.; Zolper, J.; Yun, F.; Wenham, S. R.; Sproul, A. B.; Chong, C. M.; Green, M. A. 18% Efficient Polycrystalline Silicon Solar Cells. In *IEEE Conference on Photovoltaic Specialists*; 1990; pp 678–680 vol.1. https://doi.org/10.1109/PVSC.1990.111706.
(158) Zhan, L.; Li, S.; Lau, T.-K.; Cui, Y.; Lu, X.; Shi, M.; Li, C.-Z.; Li, H.; Hou, J.; Chen, H. Over 17% Efficiency Ternary Organic Solar Cells Enabled by Two Non-Fullerene Acceptors Working in Alloy-like Model. *Energy Environ. Sci.* **2020**. https://doi.org/10.1039/C9EE03710A.
(159) Song, J.; Li, C.; Zhu, L.; Guo, J.; Xu, J.; Zhang, X.; Weng, K.; Zhang, K.; Min, J.; Hao, X.; Zhang, Y.; Liu, F.; Sun, Y. Ternary Organic Solar Cells with Efficiency >16.5% Based on Two Compatible Nonfullerene Acceptors. *Adv. Mater.* **2019**, *31* (52), 1905645. https://doi.org/10.1002/adma.201905645.
(160) Berger, P. R.; Kim, M. Polymer Solar Cells: P3HT:PCBM and Beyond. *J. Renew. Sustain. Energy* **2018**, *10* (1), 13508. https://doi.org/10.1063/1.5012992.
(161) Würfel, P. *Physics of Solar Cells: From Principles to New Concepts*; John Wiley and Sons, 2007. https://doi.org/10.1002/9783527618545.
(162) Bisquert, J.; Cahen, D.; Hodes, G.; Rühle, S.; Zaban, A. Physical Chemical Principles of Photovoltaic Conversion with Nanoparticulate, Mesoporous Dye-Sensitized Solar Cells. *J. Phys. Chem. B* **2004**, *108* (24), 8106–8118. https://doi.org/10.1021/jp0359283.
(163) Street, R. A.; Schoendorf, M.; Roy, A.; Lee, J. H. Interface State Recombination in Organic Solar Cells. *Phys. Rev. B* **2010**, *81* (20), 205307. https://doi.org/10.1103/PhysRevB.81.205307.
(164) Wu, J.; Luke, J.; Lee, H. K. H.; Shakya Tuladhar, P.; Cha, H.; Jang, S.-Y.; Tsoi, W. C.; Heeney, M.; Kang, H.; Lee, K.; Kirchartz, T.; Kim, J.-S.; Durrant, J. R. Tail State Limited Photocurrent Collection of Thick Photoactive Layers in Organic Solar Cells. *Nat. Commun.* **2019**, *10* (1), 5159. https://doi.org/10.1038/s41467-019-12951-7.
(165) Cowan, S. R.; Banerji, N.; Leong, W. L.; Heeger, A. J. Charge Formation, Recombination, and Sweep-Out Dynamics in Organic Solar Cells. *Adv. Funct. Mater.* **2012**, *22* (6), 1116–1128. https://doi.org/10.1002/adfm.201101632.
(166) Tumbleston, J. R.; Liu, Y.; Samulski, E. T.; Lopez, R. Interplay between Bimolecular Recombination and Carrier Transport Distances in Bulk Heterojunction Organic Solar Cells. *Adv. Energy Mater.* **2012**, *2* (4), 477–486. https://doi.org/10.1002/aenm.201100677.
(167) Deledalle, F.; Kirchartz, T.; Vezie, M. S.; Campoy-Quiles, M.; Shakya Tuladhar, P.; Nelson, J.; Durrant, J. R. Understanding the Effect of Unintentional Doping on Transport Optimization and Analysis in Efficient Organic Bulk-Heterojunction Solar Cells. *Phys. Rev. X* **2015**, *5* (1), 11032. https://doi.org/10.1103/PhysRevX.5.011032.
(168) Sandberg, O. J.; Dahlström, S.; Nyman, M.; Wilken, S.; Scheunemann, D.; Österbacka, R. Impact of a Doping-Induced Space-Charge Region on the Collection of Photogenerated Charge Carriers in Thin-Film Solar Cells Based on Low-Mobility Semiconductors. *Phys. Rev. Appl.* **2019**, *12* (3), 34008.

https://doi.org/10.1103/PhysRevApplied.12.034008.
(169) Hilibrand, J.; Gold, R. D. Determination of the Impurity Distribution in Junction Diodes from Capacitance-Voltage Measurements. *RCA Rev.* **1960**, *21* (2), 245–252.
(170) Zonno, I.; Martinez-Otero, A.; Hebig, J.-C.; Kirchartz, T. Understanding Mott-Schottky Measurements under Illumination in Organic Bulk Heterojunction Solar Cells. *Phys. Rev. Appl.* **2017**, *7* (3), 34018. https://doi.org/10.1103/PhysRevApplied.7.034018.
(171) Kirchartz, T.; Gong, W.; Hawks, S. A.; Agostinelli, T.; MacKenzie, R. C. I.; Yang, Y.; Nelson, J. Sensitivity of the Mott–Schottky Analysis in Organic Solar Cells. *J. Phys. Chem. C* **2012**, *116* (14), 7672–7680. https://doi.org/10.1021/jp300397f.
(172) van Mensfoort, S. L. M.; Coehoorn, R. Determination of Injection Barriers in Organic Semiconductor Devices from Capacitance Measurements. *Phys. Rev. Lett.* **2008**, *100* (8), 86802. https://doi.org/10.1103/PhysRevLett.100.086802.
(173) Sandberg, O. J.; Nyman, M.; Österbacka, R. Direct Determination of Doping Concentration and Built-in Voltage from Extraction Current Transients. *Org. Electron.* **2014**, *15* (11), 3413–3420. https://doi.org/10.1016/j.orgel.2014.09.027.
(174) Nyman, M.; Sandberg, O. J.; Dahlström, S.; Spoltore, D.; Körner, C.; Zhang, Y.; Barlow, S.; Marder, S. R.; Leo, K.; Vandewal, K.; Österbacka, R. Doping-Induced Carrier Profiles in Organic Semiconductors Determined from Capacitive Extraction-Current Transients. *Sci. Rep.* **2017**, *7* (1), 5397. https://doi.org/10.1038/s41598-017-05499-3.
(175) Pettersson, J.; Törndahl, T.; Platzer-Björkman, C.; Hultqvist, A.; Edoff, M. The Influence of Absorber Thickness on Cu(In,Ga)Se2 Solar Cells With Different Buffer Layers. *IEEE J. Photovoltaics* **2013**, *3* (4), 1376–1382. https://doi.org/10.1109/JPHOTOV.2013.2276030.
(176) Gloeckler, M.; Sites, J. R. Potential of Submicrometer Thickness Cu(In,Ga)Se2 Solar Cells. *J. Appl. Phys.* **2005**, *98* (10), 103703. https://doi.org/10.1063/1.2128054.
(177) Carlson, D. E. Recent Developments in Amorphous Silicon Solar Cells. *Sol. Energy Mater.* **1980**, *3* (4), 503–518. https://doi.org/10.1016/0165-1633(80)90002-7.
(178) Mica, N. A.; Thomson, S. A. J.; Samuel, I. D. W. Electron Mobility of Non-Fullerene Acceptors Using a Time of Flight Method. *Org. Electron.* **2018**, *63*, 415–420. https://doi.org/10.1016/J.ORGEL.2018.08.027.
(179) Bristow, H.; Thorley, K. J.; White, A. J. P.; Wadsworth, A.; Babics, M.; Hamid, Z.; Zhang, W.; Paterson, A. F.; Kosco, J.; Panidi, J.; Anthopoulos, T. D.; McCulloch, I. Impact of Nonfullerene Acceptor Side Chain Variation on Transistor Mobility. *Adv. Electron. Mater.* **2019**, *5* (10), 1900344. https://doi.org/10.1002/aelm.201900344.
(180) Choi, H.; Lee, J.; Oh, C.-M.; Jang, S.; Kim, H.; Jeong, M. S.; Park, S. H.; Hwang, I.-W. Efficiency Enhancements in Non-Fullerene Acceptor-Based Organic Solar Cells by Post-Additive Soaking. *J. Mater. Chem. A* **2019**, *7* (15), 8805–8810. https://doi.org/10.1039/C9TA00468H.
(181) Wetzelaer, G. A. H.; Kuik, M.; Nicolai, H. T.; Blom, P. W. M. Trap-Assisted and Langevin-Type Recombination in Organic Light-Emitting Diodes. *Phys. Rev. B* **2011**, *83* (16), 165204. https://doi.org/10.1103/PhysRevB.83.165204.
(182) Zhao, W.; Li, S.; Yao, H.; Zhang, S.; Zhang, Y.; Yang, B.; Hou, J. Molecular Optimization Enables over 13% Efficiency in Organic Solar Cells. *J. Am. Chem. Soc.* **2017**, *139* (21), 7148–7151. https://doi.org/10.1021/jacs.7b02677.
(183) Baran, D.; Gasparini, N.; Wadsworth, A.; Tan, C. H.; Wehbe, N.; Song, X.; Hamid, Z.; Zhang, W.; Neophytou, M.; Kirchartz, T.; Brabec, C. J.; Durrant, J. R.; McCulloch, I. Robust Nonfullerene Solar Cells Approaching Unity External Quantum Efficiency Enabled by Suppression of Geminate Recombination. *Nat. Commun.* **2018**, *9* (1), 1–9.

https://doi.org/10.1038/s41467-018-04502-3.
(184) Zhang, S.; Qin, Y.; Zhu, J.; Hou, J. Over 14% Efficiency in Polymer Solar Cells Enabled by a Chlorinated Polymer Donor. *Adv. Mater.* **2018**, *30* (20), 1–7. https://doi.org/10.1002/adma.201800868.
(185) Yuan, J.; Zhang, Y.; Yuan, J.; Zhang, Y.; Zhou, L.; Zhang, G.; Yip, H.; Lau, T.; Lu, X.; Li, Y.; Zou, Y. Single-Junction Organic Solar Cell with over 15 % Efficiency Using Fused-Ring Acceptor with Electron-Deficient Core. *Joule* **2019**, *3*, 1140–1151.
(186) Cui, Y.; Yao, H.; Zhang, J.; Zhang, T.; Wang, Y.; Hong, L.; Xian, K.; Xu, B.; Zhang, S.; Peng, J.; Wei, Z.; Gao, F.; Hou, J. Over 16% Efficiency Organic Photovoltaic Cells Enabled by a Chlorinated Acceptor with Increased Open-Circuit Voltages. *Nat. Commun.* **2019**, *10* (1), 2515. https://doi.org/10.1038/s41467-019-10351-5.
(187) Etzold, F.; Howard, I. A.; Mauer, R.; Meister, M.; Kim, T.-D.; Lee, K.-S.; Baek, N. S.; Laquai, F. Ultrafast Exciton Dissociation Followed by Nongeminate Charge Recombination in PCDTBT:PCBM Photovoltaic Blends. *J. Am. Chem. Soc.* **2011**, *133* (24), 9469–9479. https://doi.org/10.1021/ja201837e.
(188) Bakulin, A. A.; Rao, A.; Pavelyev, V. G.; van Loosdrecht, P. H. M.; Pshenichnikov, M. S.; Niedzialek, D.; Cornil, J.; Beljonne, D.; Friend, R. H. The Role of Driving Energy and Delocalized States for Charge Separation in Organic Semiconductors. *Science (80-.).* **2012**, *335* (6074), 1340–1344. https://doi.org/10.1126/science.1217745.
(189) Yamaciyan, A.; Stolterfoht, M.; Burn, P. L.; Lin, Q.; Meredith, P.; Armin, A. Recombination Losses Above and Below the Transport Percolation Threshold in Bulk Heterojunction Organic Solar Cells. **2018**, *1703339*, 1–8. https://doi.org/10.1002/aenm.201703339.
(190) Proctor, C. M.; Kim, C.; Neher, D.; Nguyen, T. Q. Nongeminate Recombination and Charge Transport Limitations in Diketopyrrolopyrrole-Based Solution-Processed Small Molecule Solar Cells. *Adv. Funct. Mater.* **2013**, *23* (28), 3584–3594. https://doi.org/10.1002/adfm.201202643.
(191) Maurano, A.; Hamilton, R.; Shuttle, C. G.; Ballantyne, A. M.; Nelson, J.; O'Regan, B.; Zhang, W.; McCulloch, I.; Azimi, H.; Morana, M.; Brabec, C. J.; Durrant, J. R. Recombination Dynamics as a Key Determinant of Open Circuit Voltage in Organic Bulk Heterojunction Solar Cells: A Comparison of Four Different Donor Polymers. *Adv. Mater.* **2010**, *22* (44), 4987–4992. https://doi.org/10.1002/adma.201002360.
(192) Credgington, D.; Hamilton, R.; Atienzar, P.; Nelson, J.; Durrant, J. R. Non-Geminate Recombination As the Primary Determinant of Open-Circuit Voltage in Polythiophene:Fullerene Blend Solar Cells: An Analysis of the Influence of Device Processing Conditions. *Adv. Funct. Mater.* **2011**, *21* (14), 2744–2753. https://doi.org/10.1002/adfm.201100225.
(193) Göhler, C.; Wagenpfahl, A.; Deibel, C. Nongeminate Recombination in Organic Solar Cells. *Adv. Electron. Mater.* **2018**, *1700505*, 1–18. https://doi.org/10.1002/aelm.201700505.
(194) Gasparini, N.; Salvador, M.; Heumueller, T.; Richter, M.; Classen, A.; Shrestha, S.; Matt, G. J.; Holliday, S.; Strohm, S.; Egelhaaf, H. J.; Wadsworth, A.; Baran, D.; Mcculloch, I.; Brabec, C. J. Polymer: Nonfullerene Bulk Heterojunction Solar Cells with Exceptionally Low Recombination Rates. *Adv. Energy Mater.* **2017**, *1701561*, 1–8. https://doi.org/10.1002/aenm.201701561.
(195) Coropceanu, V.; Brédas, J.-L.; Mehraeen, S. Impact of Active Layer Morphology on Bimolecular Recombination Dynamics in Organic Solar Cells. *J. Phys. Chem. C* **2017**, acs.jpcc.7b07768. https://doi.org/10.1021/acs.jpcc.7b07768.

(196) Heiber, M. C.; Baumbach, C.; Dyakonov, V.; Deibel, C. Encounter-Limited Charge Carrier Recombination in Phase Separated Organic Semiconductor Blends. *Phys. Rev. Lett.* **2015**, No. 2, 3–5. https://doi.org/10.1103/PhysRevLett.114.136602.
(197) Arkhipov, V. I.; Perova, I. A. Non-Lagevin Recombination in Disordered Dielectrics. *J. Phys. D. Appl. Phys.* **1993**, *26* (8), 1301–1303. https://doi.org/10.1088/0022-3727/26/8/022.
(198) Burke, T. M.; Sweetnam, S.; Vandewal, K.; McGehee, M. D. Beyond Langevin Recombination: How Equilibrium between Free Carriers and Charge Transfer States Determines the Open-Circuit Voltage of Organic Solar Cells. *Adv. Energy Mater.* **2015**, *5* (11), 1–12. https://doi.org/10.1002/aenm.201500123.
(199) Armin, A.; Durrant, J. R.; Shoaee, S. Interplay between Triplet-, Singlet-Charge Transfer States and Free Charge Carriers Defining Bimolecular Recombination Rate Constant of Organic Solar Cells. *J. Phys. Chem. C* **2017**, *121* (25), 13969–13976. https://doi.org/10.1021/acs.jpcc.7b04825.
(200) Dimitrov, S. D.; Wheeler, S.; Niedzialek, D.; Schroeder, B. C.; Utzat, H.; Frost, J. M.; Yao, J.; Gillett, A.; Tuladhar, P. S.; McCulloch, I.; Nelson, J.; Durrant, J. R. Polaron Pair Mediated Triplet Generation in Polymer/Fullerene Blends. *Nat. Commun.* **2015**, *6*, 1–8. https://doi.org/10.1038/ncomms7501.
(201) Etzold, F.; Howard, I. A.; Forler, N.; Melnyk, A.; Andrienko, D.; Hansen, M. R.; Laquai‡, F. Sub-Ns Triplet State Formation by Non-Geminate Recombination in PSBTBT:PC_{70}BM and PCPDTBT:PC_{60}BM Organic Solar Cells. *Energy Environ. Sci.* **2015**, *8* (5), 1511–1522. https://doi.org/10.1039/C4EE03630A.
(202) Gorenflot, J.; Heiber, M. C.; Baumann, A.; Lorrmann, J.; Gunz, M.; Dyakonov, V.; Deibel, C. Nongeminate Recombination in Neat P3HT and P3HT:PCBM Blend Films. *J. Appl. Phys.* **2014**, *115* (14), 144502. https://doi.org/10.1063/1.4870805.
(203) Kurpiers, J.; Neher, D. Dispersive Non-Geminate Recombination in an Amorphous Polymer:Fullerene Blend. *Sci. Rep.* **2016**, *6* (February), 1–10. https://doi.org/10.1038/srep26832.
(204) Credgington, D.; Jamieson, F. C. .; Walker, B.; Nguyen, T.-Q.; Durrant, J. R. Quantification of Geminate and Non-Geminate Recombination Losses within a Solution Processed Small-Molecule Bulk Heterojunction Solar Cell. *Adv. Mater.* **2012**, *24* (16), 2135–2141.

Acknowledgments

First of all, I want to thank all the people in my life who made me become passionate for science. My gratitude goes to my family and my friends for their unconditional and never-ending support. Without their contribution, support, and encouragement, all this would not have been possible.

I will be forever thankful to my supervisor Prof. Dr. Safa Shoaee, who mindfully guided me through this beautiful scientific journey teaching me not only her vast scientific knowledge, but most importantly, how to be a true scientist. Her genuine passion and curiosity for the scientific research will always resonate in me.

I want to deeply thank Prof. Dr. Dieter Neher for constant support in every aspect and also for making his professional laboratories available to me.

I would also like to thank every member of the "Soft Matter Physics" and "Organic Disordered Semiconductor" groups.

I am extremely grateful to all our scientific collaborators for their valuable inputs over the years.

Last, but not least, I want to thank the Alexander von Humboldt Foundation for providing me with full economic support during the complete duration of my doctoral studies.

The author,
Seyed Mehrdad Hosseini

Eigenständigkeitserklärung

Ich erkläre hiermit, dass ich diese Arbeit selbstständig verfasst und keine anderen als die angegebenen Hilfsmittel benutzt habe. Diese Arbeit wurde an keiner anderen Hochschule eingereicht.

Potsdam, den

Seyed Mehrdad Hosseini